

**Control of Properties of  
Amorphous Carbon Thin Films  
by Internal Parameters of  
a Low-Temperature Plasma**

**SUGIURA Hirotsugu**

2019

Department of Electrical Engineering and Computer Science  
Graduate School of Engineering, Nagoya University



## Contents

Chapter 1 Introduction.....	1
1.1 Carbon materials.....	1
1.2 Amorphous carbon.....	3
1.3 Deposition methods of amorphous carbon and their mechanisms.....	5
1.3.1 Ion beam deposition.....	5
1.3.2 Sputtering deposition.....	9
1.3.3 Plasma enhanced chemical vapor deposition.....	11
1.4 Objective and composition of this thesis .....	22
Chapter 2 Methods .....	25
2.1 Deposition of a-C films by radical injection plasma enhanced chemical vapor deposition (RI-PECVD) .....	25
2.2 Plasma characterization .....	28
2.2.1 Negative self-bias voltage.....	28
2.2.2 Plasma absorption probe (Electron density).....	28
2.2.3 Optical emission spectroscopy (Electron temperature and radical species).....	30
2.2.4 Quadrupole mass spectroscopy (Radical and ion species).....	32
2.3 Film characterization.....	34
2.3.1 Line profiler (Thickness).....	34
2.3.2 Visible Raman spectroscopy (sp <sup>2</sup> -C clusters and H content).....	35
2.3.4 Spectrophotometer (Optical bandgap).....	41
2.3.5 I-V measurements (Conductivity) .....	43
2.3.7 Electron spin resonance (Dangling bonds).....	44
2.3.8 Nanoindentation (Hardness) .....	45

## Contents

Chapter 3 The effects of H atoms and H ions on the film properties of a-C films .....	46
3.1 Experimental details .....	47
3.2 Results and discussion .....	53
3.3 Discussion: Effects of H atoms and H ions .....	60
3.4 Conclusions .....	61
Chapter 4 Control of CH <sub>3</sub> radical and its effects on the sp <sup>2</sup> fraction and hardness of a-C film .....	62
4.1 Experimental details .....	64
4.2 Results and discussion .....	65
4.3 Conclusions .....	75
Chapter 5 Control of sp <sup>2</sup> -C cluster incorporation of a-C films via monitoring of C <sub>2</sub> radical density .....	76
5.1 Experimental details .....	77
5.2 Results and discussion .....	78
5.2.1 Effect of the VHF power on the deposition .....	78
5.2.2 The possibility of the sp <sup>2</sup> -C cluster formation by C <sub>2</sub> radicals .....	88
5.2.3 Structural control of a-C films via C <sub>2</sub> radical in the H <sub>2</sub> / CH <sub>4</sub> plasma .....	89
5.3 Conclusions .....	90
Chapter 6 Effects of ion bombardment energy flux on chemical compositions and structures of a-C films .....	91
6.1 Experimental details .....	92
6.2 Results and discussion .....	93
6.2.1 Plasma characteristics .....	93
6.2.2 Effects of ion bombardment energy flux on the deposition rate ....	
.....	97

## Contents

6.2.3	Effects of ion bombardment energy flux on Slope/I <sub>G</sub> and density of dangling bonds.....	98
6.2.4	Effects of ion bombardment energy flux on sp <sup>2</sup> -C clusters.....	102
6.2.5	Discussion: H desorption and carbon-carbon continuous network formation by the ion bombardment energy flux.....	108
6.2.6	Effects of ion bombardment energy flux on optical bandgap and electrical conductivity.....	109
6.3	Discussion.....	111
6.4	Conclusions.....	114
Chapter 7	Development of the remote plasma source for the <i>in-situ</i> transmission electron microscopy under plasma irradiation.....	115
7.1	Introduction of layer-by-layer thinning of graphene.....	116
7.2	Methods.....	118
7.3	Results and discussion.....	122
7.4	Conclusions.....	131
Chapter 8	Summary and Conclusions.....	132
Chapter 9	Remaining issues and Future perspective.....	137
References	.....	140
List of figures and tables	.....	157
Figures	.....	157
Tables	.....	163
List of papers and presentations related to this thesis.....		164
Original Papers.....		164
Presentations in International conferences.....		165
Acknowledgments	.....	167

## Chapter 1 Introduction

### 1.1 Carbon materials

Carbon materials show various structures with electronic properties depending on bonding states of carbon atoms. Crystalline graphite, diamond, and amorphous carbon are widely known as typical phases of carbon materials. Since the end of the twentieth century, fullerene ( $C_{60}$ ) [1] and carbon nanotubes (CNT) [2], Carbon nanowalls (CNWs) [3] were found as new families of carbon materials. The carbon materials have become more diverse and had a variety of allotrope and material groups.

Factors that represent various structures of carbon materials are attributable to their electron orbits. There are 3 different hybridizations such as  $sp$ ,  $sp^2$ , and  $sp^3$  hybridizations in Carbon materials. The carbon material consisting of  $sp$  hybridization is called carbyne which can be synthesized under the limited condition [4]. The well-known forms of carbon are diamond ( $sp^3$ ) and graphite ( $sp^2$ ). Here, the author focuses on  $sp^3$  and  $sp^2$  carbon ( $sp^3$ -C,  $sp^2$ -C) materials.

The  $sp^3$  hybrid orbit becomes the tetrahedral structure with energy equivalent bonds. Diamond is a representative  $sp^3$  hybridized carbon material. It is well known that diamond has outstanding properties such as high resistivity, high hardness, high transparency, and wide bandgap because of its  $sp^3$  hybrid orbit.

When  $sp^2$  carbons are bonded to each other,  $sp^2$  hybridized orbits are bonded to each other to form  $\sigma$  bonds, and orbits of 2  $p_z$  share electrons and bond each other. The coupling between orbits of 2  $p_z$  is called  $\pi$  bond. A double bond is formed by  $\sigma$  and  $\pi$  bonds. This  $\pi$  bond plays an important role on

electrical conduction. Graphite is a representative  $sp^2$  hybridized carbon material. Graphite has high carrier mobility because of the  $\pi$  electron cloud.

Through these hybrid orbits, carbon materials show various structures and electronic properties. One example is Amorphous carbon (a-C). Amorphous carbon is a mixture of  $sp^3$ -C and  $sp^2$ -C as shown in Fig.1.1. This is a unique character of amorphous carbon because other amorphous materials have only one hybridized bonding. Because of multi hybrid orbits in the atomic network, a-C shows wide range electronic, electrical, mechanical, and optical properties depending on a mixture ratio of  $sp^3$ -C and  $sp^2$ -C. In the current study, amorphous carbon is a research object because of these unique bonding structures.

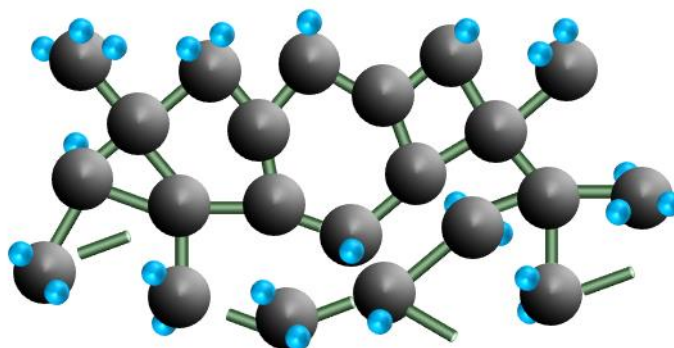


Figure 1.1 The schematic of the a-C structure. Black balls are C atoms, and blue balls are H atoms.

## 1.2 Amorphous carbon

As mentioned in Section 1.1, a-C shows a wide variety of film properties. The properties of a-C films, including high mechanical hardness, chemical inertness, a wide variety of optical bandgaps, and strong photoluminescence (PL), have attracted much attention for applications in hard coating films and electronic devices [5–12]. A large variety of optical and electronic properties of a-C films depends on the mixture ratio of  $sp^2$  to  $sp^3$  bonding states. Thus, based on comprehensive studies on bonding structures, control of these properties is achieved by precise tuning of deposition processes.

A ternary phase diagram of carbon materials was reported by Jacob and Moller as shown in Fig.1.2 [13]. The diagram consists of  $sp^2$ -C,  $sp^3$ -C and hydrogen (H). The a-C films containing a lot of  $sp^3$ -C are called tetrahedral amorphous carbon (ta-C) and shows properties close to that of diamond such as high hardness and wide band gap. On the other hand, the a-C films containing less  $sp^3$ -C, and more  $sp^2$ -C are just called a-C and shows the graphite-like properties such as narrow bandgap, high electrical conductivity. Hydrogen (H) content is also important when it is included in the a-C film, usually called hydrogenated ta-C (ta-C:H) and hydrogenated a-C (a-C:H). The incorporation of H makes the a-C films soft and low density. And, the electrical conductivity also decreases by the incorporation of H. The a-C films containing much H are called polymer like carbon (PLC). Therefore, the optical, electrical, and electronic properties of a-C films are mainly, but not completely, determined by the compositional ratios of  $sp^2$ -C,  $sp^3$ -C, and H in the films.

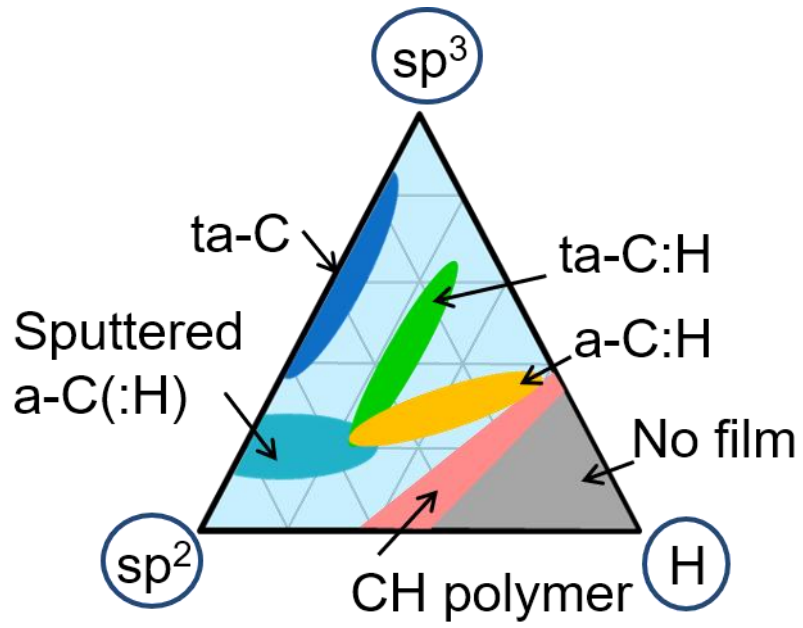


Figure 1.2 The ternary diagram of a-C films.

The focus has been placed on the structures of a-C films that were configured by chemical bonding ratio of  $sp^2$  and  $sp^3$ , such as the six-membered ring, aromatic compounds, aliphatic compounds, olefins, and diamond. The narrow optical bandgap of a-C films arises from a large number of electronic levels of  $sp^2$ -C bonds, appearing at discrete energy levels in a gap of the energy band for  $sp^3$ -C bonds [14]. This electronic structure can also induce metallic features or pronounced current leakage or act as recombination sites of photo-generation carriers [15]. Moreover, increasing the  $sp^2$ -C in a-C films causes decreases in their atomic densities and hardnesses [16]. Therefore, a method to control the bonding configurations, especially for the inclusion of the  $sp^2$ -C clusters in the a-C films, which determines the electronic structure and the mechanical hardness, is essential to realize various applications of a-C films.

### **1.3 Deposition methods of amorphous carbon and their mechanisms**

For the synthesis of a-C films, ion beam deposition, sputtering deposition, and a plasma enhanced chemical vapor deposition (PECVD) are commonly used. Here, brief characteristics of deposition methods and as-deposited a-C are explained.

#### **1.3.1 Ion beam deposition**

The ion beam deposition is an initial deposition method of a-C films operated by Aisenberg Chabot [17]. This method uses 2 separate chambers; one is a source chamber, the other is a deposition chamber. In the source chamber, the hollow discharge of Ar is used with carbon anode and cathode. The carbon electrode is sputtered by the positive Ar ion bombardment; then

the sputtered carbons are ionized in the Ar plasma. These ions are extracted from the source chamber to the deposition chamber by the magnetic field. The extracted carbon ions are accelerated by a bias voltage to the substrate. In this case, incident ions to the substrate include Ar ions. The mass-selected ion beam deposition was proposed by Lifshitz group [18]. This method can control incident ion species and give precise control of the film structure. However, the ion beam deposition method can provide only a low deposition rate because of the limited amount of sputtered carbons.

The cathodic arc deposition is a kind of ion beam deposition technique. This method uses arc discharge to generate a carbon source. The evaporated carbon atoms from the cathode are immediately ionized by a thermal electron from the cathode. This method can provide enough carbon source than ion beam deposition method, that means the deposition rate is higher than ion beam deposition. A demerit of the cathodic arc deposition is a generation of a droplet from the cathode. The droplet makes the surface of deposited a-C films rough. Filtered arc deposition using a Quarter-torus duct macroparticle filter was proposed by Aksenov et al. as shown in Fig. 1.3 [19,20]. The filter enables us to avoid depositing the droplet on the substrate. Many types of filtering methods were proposed such as filtered cathodic arc, T-shaped filtered arc [21,22].

The most benefit of ion beam deposition is the narrow energy distribution. This method only uses ions and the deposition chamber usually high vacuum around  $10^{-4}$  Pa. Therefore, the ions reach without energy loss by collision, and the ion energy is the almost same as the applied bias voltage to the substrate. The a-C deposited by this method usually contains a huge amount of  $sp^3$ -C than  $sp^2$ -C.

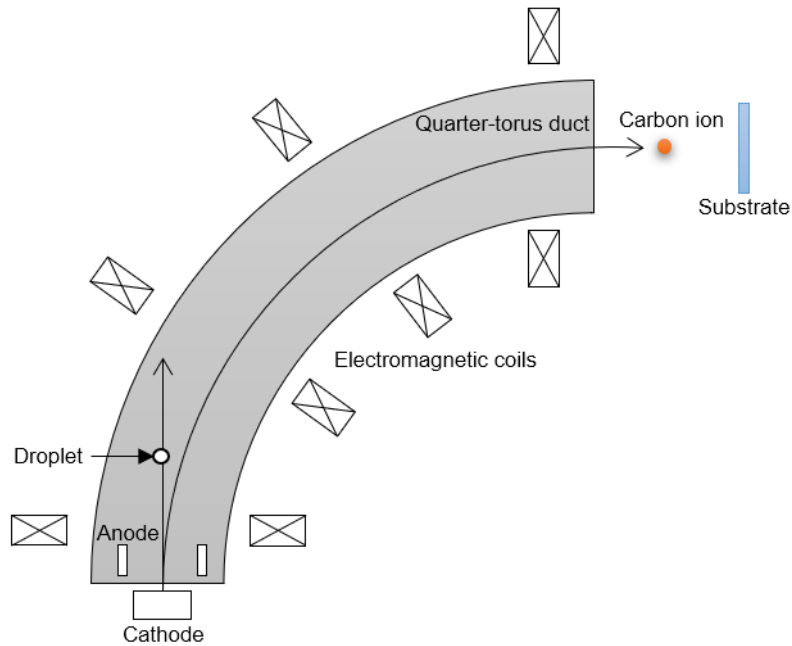


Figure 1.3 Aksenov Quarter-torus duct macroparticle filter using plasma optical principles for cathodic arc deposition.

The mechanism of ion beam deposition is well understood, as the subplantation model (Fig. 1.4).

The formation of  $sp^3$ -bonded structures in a-C films has been proposed using ion bombardment with relatively high energies. The ions which have energies more than 30 eV can penetrate the a-C film. Furthermore, the penetration of energetic carbon ion, which contains around 100 eV per atom, densifies local carbon-networks and converts the bonds from  $sp^2$  to  $sp^3$  bonding structures [23]. More than 100 eV, the relaxation process occurs, that is, the  $sp^3$ -C to  $sp^2$ -C translation because of the lower energy state of  $sp^2$ -C than the  $sp^3$ -C. Therefore, the atomic density and  $sp^3$  fraction show their maximum around the 100 eV per C atom as shown in Fig. 1.5..

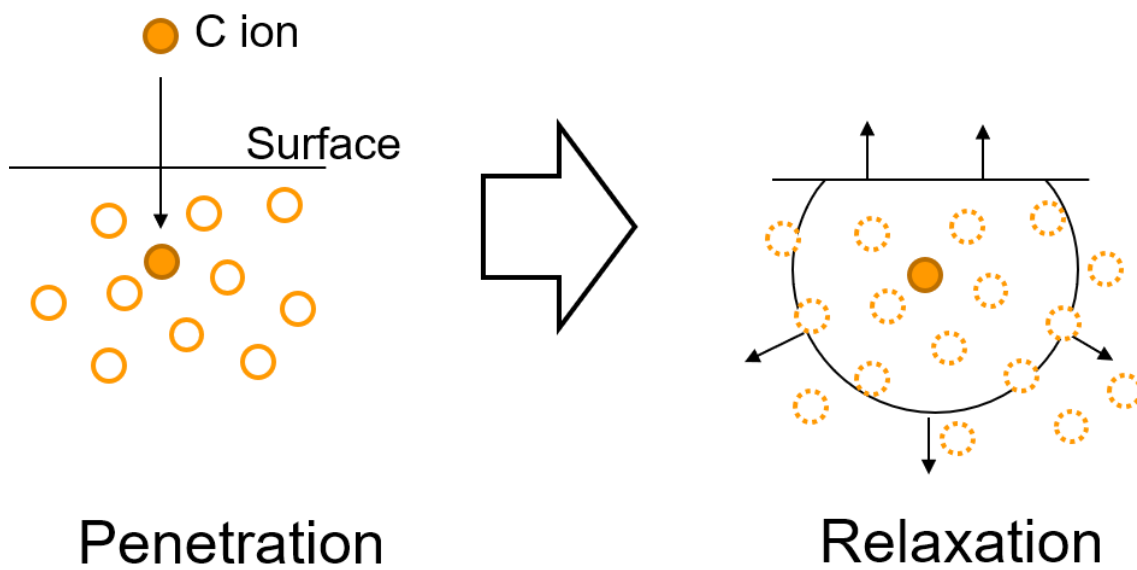


Figure 1.4 The schematic diagram of the subplantation model.

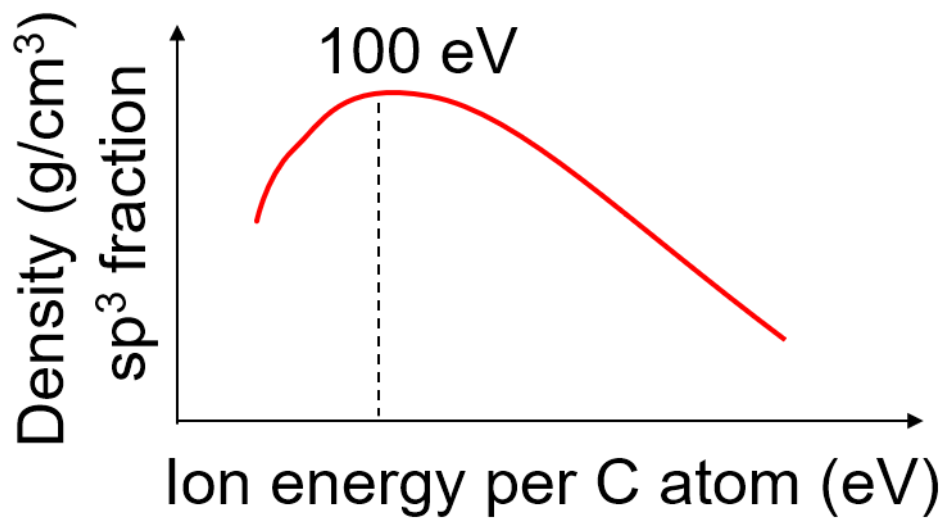


Figure 1.5 The schematic plot of the density and the  $sp^3$  fraction of a-C films as a function of ion energy per C atom.

### 1.3.2 Sputtering deposition

Figure 1.6 shows a schematic diagram of the typical sputtering deposition system. Sputtering is the most popular industrial approach for the synthesis of thin film metals, metal oxides, and a-C. Ar plasma is generated by applying a direct current (DC) or Radio frequency (RF) power to the electrode. The source materials are used in the cathode, and the substrate is put on an anode. The source materials are sputtered by the ion bombardment of Ar ions. Then sputtered materials were deposited on the opposite side substrate through the plasma region. For the a-C, the graphite target is used. The magnetron is often used in the anode to improve the sputtering yield by increasing plasma density near the target material.

The difference between ion beam deposition and sputtering deposition is whether the substrate is exposed to the plasma. The sputtering deposition can dope the various kind of atoms by addition of dopant gas to the plasma, and also putting the other material on the electrode. Therefore, the sputtering is suitable to synthesize composite materials such as SiC, BC, and CN [24–30].

The deposition mechanism of sputtering is also can be explained by a subplantation model. The a-C films deposited by sputtering have usually higher  $sp^2$  fraction than that of ion beam deposition. The ionization efficiency by the sputtering is very low, and the sputtered carbon atoms and ions reaching the substrate have less energy because there are some difficulties in applying a bias voltage to the substrate. In the sputtering deposition, the discharge gas species mainly consist of a noble gas, such as Ar. Applying the bias voltage to the substrate, high energetic Ar ions also bombard to the deposited films and induce the sputtering from the sample again. However, by applying a moderate bias voltage, increases of the film hardness and

density were reported by some researchers [31–34]. That means that ion energy can be controlled by the bias voltage. The remaining problem is a low ionization efficiency. High Power Impulse Magnetron Sputtering (HiPIMS) is a candidate for high efficient ionization to solve this problem. HiPIMS was first reported by Kouznetsov et al. [35,36] HiPIMS can ionize target without excess heating of the substrate by high power plasma because of high power pulse discharge.

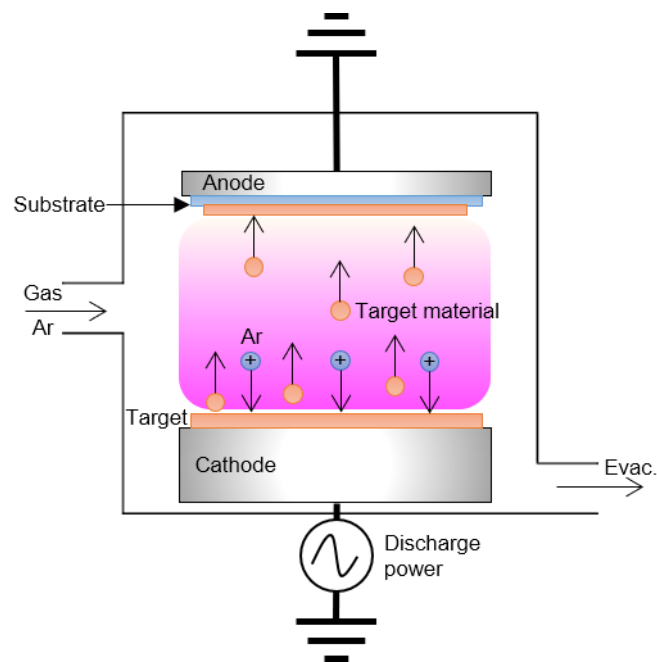


Figure 1.6 Schematic diagram of an RF sputtering system.

### 1.3.3 Plasma enhanced chemical vapor deposition

The PECVD system is the most popular synthesis method for laboratory and industry research. The advantages of the PECVD are the uniform deposition with large size wafer and the wide selectivity of source gases.

The important factors of the PECVD are ions and radicals. Figure 1.7 shows fundamental reactions in plasma processing. In the plasma, the electron is accelerated by the input power. When high energetic electrons collide with the source gas, the gas is changed its form via the excitation, dissociation, and ionization. To maintain the plasma discharge, the ionization process is very important. Ionization provides new electrons to the plasma; then the plasma is kept discharge. For the processing, dissociation and excitation are important as well. By the excitation and dissociation, excited neutrals and radicals are generated. Excited neutrals, radicals, and ions can react the material put in the plasma, and then, deposition, etching, and modification occur. For the deposition of a-C films, the deposition source of carbon is provided from the source gas, usually hydrocarbon. The source gas is dissociated and ionized by the electron collision. Then, radicals and ions flow into the substrate surface. Although radicals are neutral, they are chemically active because they have dangling bonds. When radicals reach the substrate surface, the radicals react with atoms at the surface. Ions have bombarded the surface with some energy. The conditions of electrons, ions, excited neutrals, vacuum ultraviolet (VUV), and ultraviolet (UV) photons are so-called “internal parameter” of the plasma. For precise control of the plasma process such as etching, deposition, and modification, it is undoubtedly important to control internal parameters of plasma. In the actual deposition process, the etching and modification of chemical termination also occur simultaneously. Therefore, to control the deposition process, it is necessary to

measure the internal parameters and discuss the mechanism of the film formation based on the measurement results of an internal parameter of plasma. The internal parameters can be controlled by the external parameters such as a input power, a pressure, and a gas flow rate.

The key roles of ion, radical, and light (VUV, UV) for the plasma processing are as follows.

(i) Ions

Ions show the different effects depending on the ion bombardment energy. The low energetic ions usually only react with the film surface and adsorb on the film. However, with increasing ion bombardment energy, ions can penetrate the film, knock on the surface atoms deeper into the film, and sputter the films physically or chemically. The ion bombardment sometimes makes film damaged and defective because of the energy transfer from ions to film. Control of ion bombardment energy is very important for plasma deposition.

(ii) Radicals

Radicals are usually reactive and easy to bind at the film surface. For both deposition and etching process, it is important whether the products from the film surface reaction with radicals are volatile or not at the process temperature. If the products are volatile, the films are etched off. The sticking coefficient of radicals is also important. Radicals having the high sticking coefficient can not migrate on the film surface and form the ununiform film. On the other hand, the low sticking coefficient radicals can migrate on the film surface and stick at the chemically active bond, called dangling bond at the surface. In this case, the deposited film is uniform. However, the generation of dangling bonds is mandatory.

(iii) Lights (VUV, UV photons)

Lights such as VUV and UV photons act as a bond cleavage. Zhang et al. reported that VUV photons cleave the oxygen-containing group and induce the crosslinking reaction at the surface in the case of polyethylene terephthalate (PET) [37]. VUV photons are important to consider the surface modifications and etching process.

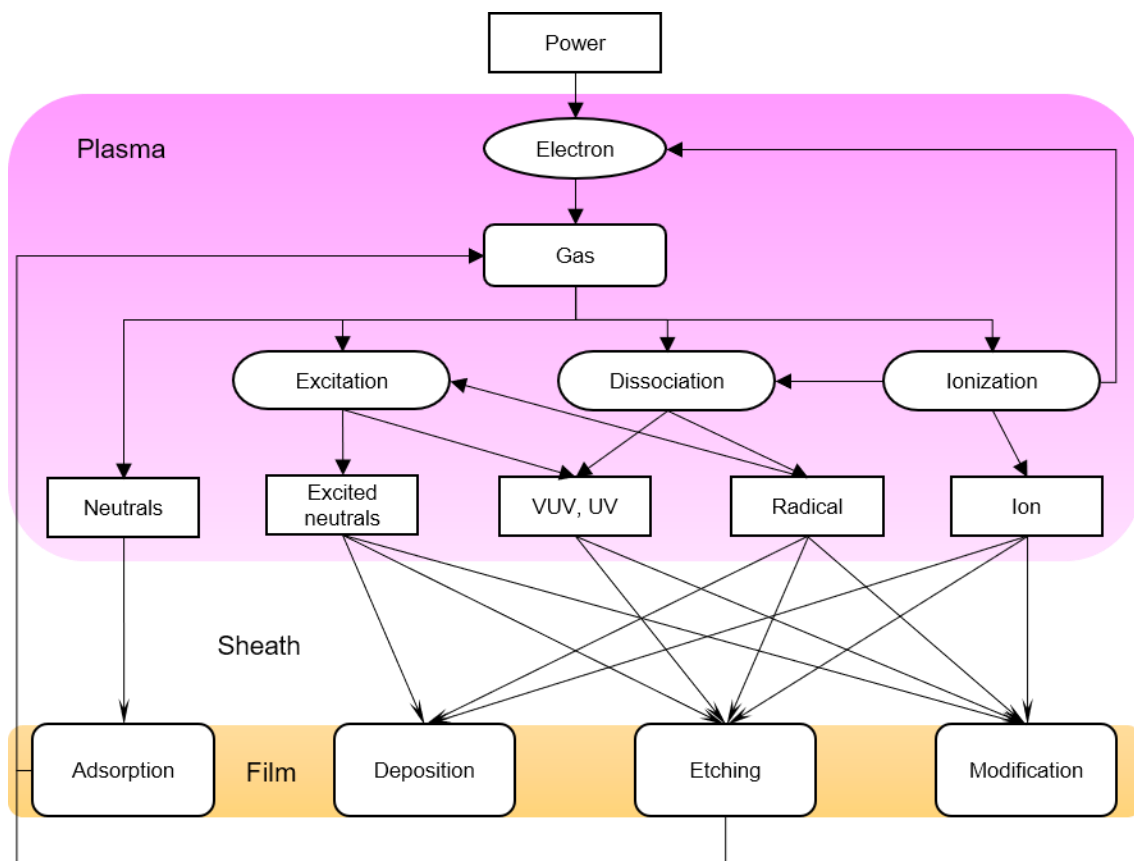


Figure 1.7 Fundamentals in a plasma processing.

Figure 1.8 shows a schematic diagram of dual-frequency capacitively coupled plasma (DF-CCP) system with a showerhead electrode and substrate bias power. The CCP is generated between two parallel electrodes. A very high frequency (VHF) power is applied to the upper showerhead electrode to generate plasma. The showerhead electrode is useful to generate plasma uniformly in between electrodes. An RF bias power is applied to the lower electrode where the substrate is mounted to control ion energy. When the RF power is applied to the electrode, both electrons and ions will move with following a change of the electric field. Electrons can follow the RF electric field; however, ions cannot follow it because the mass of electrons is much smaller than that of ions. Thus, the sheath, which is excess ions region, is generated because of the electron loss near the electrode and ground by the RF electric field acceleration. The capacitor is usually connected between the electrode and power supply to match the impedance of plasma and output of power supply. This capacitor is negatively charged up by the electron loss at the electrode. Then, the negative DC self-bias voltage ( $-V_{DC}$ ) is built up the powered electrode. When the ions flow into the sheath region, ions can move by a DC electric field at the sheath, and accelerated ions travel to the powered electrode by the  $-V_{DC}$ . The ion bombardment energy can be controlled by the  $-V_{DC}$ .

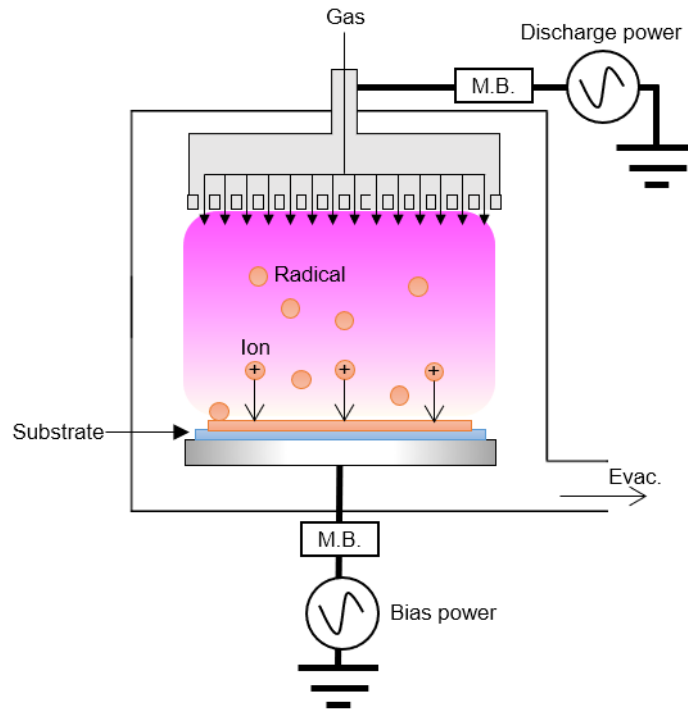


Figure 1.8 Schematic diagram of the capacitively coupled plasma with a showerhead electrode and substrate bias power.

Although the ion bombardment energy is very important, the effects of radicals cannot be negligible in the case of PECVD as mentioned before. The ion flux to the substrate surface is usually 10%. The 90% of the incident flux is the radicals'. The generation of radicals highly depends on the dissociation of the source gas. Radicals in the reactive plasma are mainly generated by the dissociation of source gas via collisions between source gas and electrons. The generation rate of radical,  $G$ , by dissociation, is described by

$$G = Kn_e n_g \quad (1-1)$$

where  $K$  is the dissociation rate constant,  $n_e$  is the electron density,  $n_g$  is the gas density. The most important parameter here is  $K$ ,

$$K = \int \sigma(E) \left( \frac{2E}{m_e} \right)^{1/2} f(E) dE = \langle \sigma v \rangle \quad (1-2)$$

where  $\sigma$  is the electron impact dissociation cross section,  $E$  is the electron energy in plasma,  $m_e$  is the mass of the electron,  $f$  is the electron energy distribution function (EEDF),  $v$  is the velocity of the electron. The author assumes that EEDF is a Maxwellian distribution as a function of electron temperature ( $T_e$ ),  $\langle\sigma v\rangle$  can be controlled by  $T_e$  as shown in Fig. 1.9.

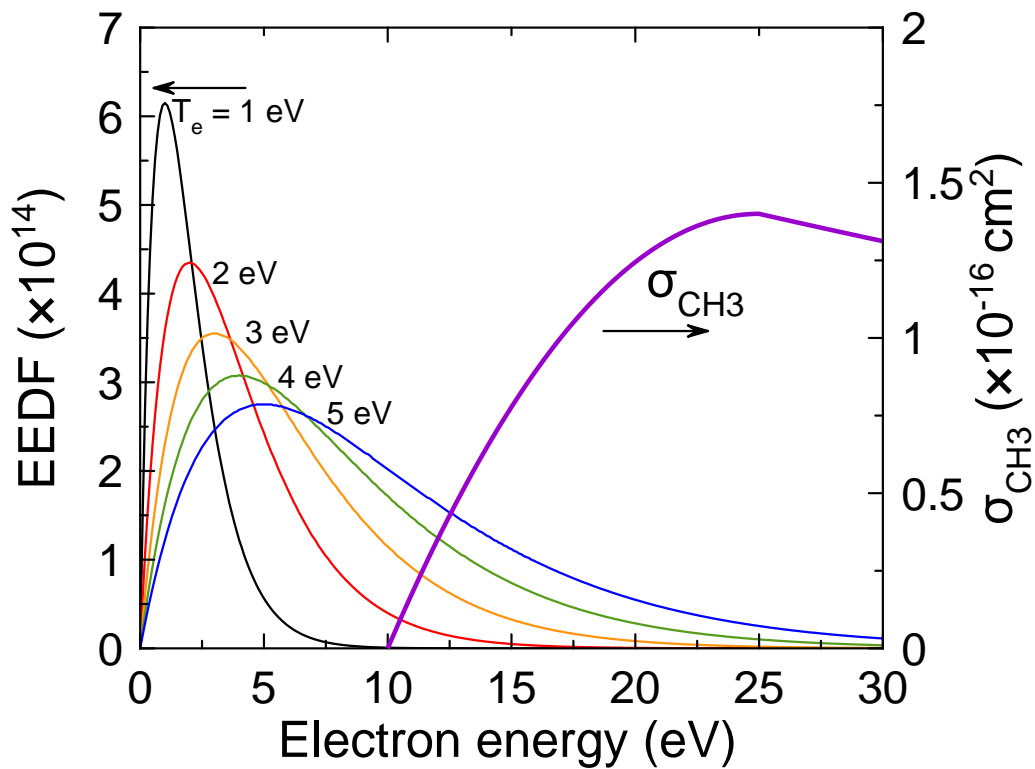


Figure 1.9 Electron energy distribution function (EEDF) and electron dissociation coefficient of  $\text{CH}_4$  to  $\text{CH}_3$  ( $\sigma_{\text{CH}_3}$ ) as functions of electron energy.

Here, the residence time ( $\tau$ ) of the source gas should be introduced. When the  $\tau$  is short, the gas dissociates only one time in the plasma, and it is soon evacuated. However, with increasing  $\tau$ , multiple collision with electron can occur, and the dissociation of source gas enhanced. This will change the radical composition in the plasma. Jia previously reported in his thesis that the dissociation of  $\text{CH}_4$  was enhanced and film properties are significantly changed with increasing the  $\tau$ .

In summary of the components of the dissociation,  $n_e$ ,  $\langle\sigma v\rangle$ , and  $\tau$ , the dissociation degree ( $D$ ) of source gas can be described as,

$$D \propto n_e \langle\sigma v\rangle \tau \quad (1-3)$$

Therefore, the control of the  $D$  based on the plasma diagnostics of  $n_e$  and  $T_e$ , and the control of the  $\tau$  is necessary to control the deposition.

The electron density can be controlled by the magnitude and frequency of the applying power. Usually, in the case of CCP, the electron density increases with increasing the discharge power and the frequency of the power. On the other hands, the electron temperature is almost not changed by the discharge power because the electron density is sensitive to the ionization rate constant  $K_{iz}$ , which is sensitively changed by the electron temperature. Therefore, a change of the electron temperature is small than that of the electron density. The residence time,  $\tau$ , is easily controlled by a flow rate of the introduced gas, the pressure, and the volume of the chamber, as the following equation (1-4),

$$\tau = \frac{V_{pl} \times P_{dep}}{P_0 \times f_{total}} \quad (1-4)$$

where  $V_{pl}$  is the volume of plasma,  $P_{dep}$  is the pressure during deposition,  $P_0$  is the standard pressure, and  $f_{total}$  is the total gas flow rate.

To control the electron density and electron temperature, the other candidate method is the use of other types of plasma source.

Figure 1.10 shows an inductively coupled plasma (ICP) source. The characteristic of the ICP is attributable to high electron density generated by the RF power. Usually, the electron density of the ICP is around  $10^{11-12} \text{ cm}^{-3}$ . This value is more than 10 times higher value than that of CCP. The floating voltage at the sheath edge is usually low; then the RF bias power is applied to the substrate to control the ion energy.

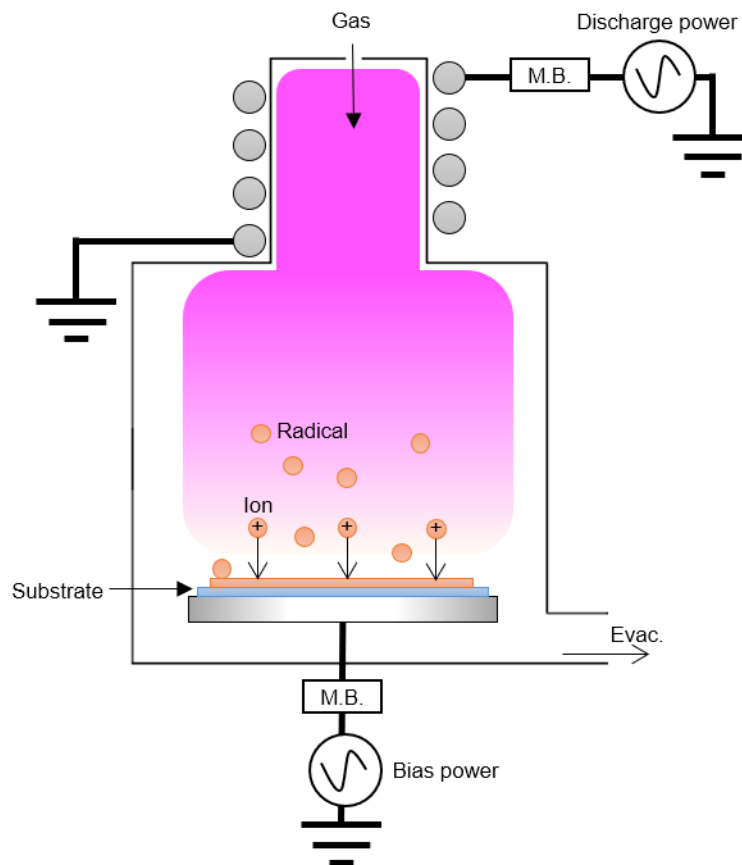


Figure 1.10 Schematic diagram of inductively coupled plasma with substrate bias power.

Figure 1.11 shows the surface wave plasma (SWP) source. The electron density of SWP is also high as well as ICP. SWP can be generated high-density plasma in relatively high pressure (2-200 Pa) compared with CCP (1-1000 Pa) and ICP (1-40 Pa). The floating voltage at the sheath edge is usually low as well as ICP; then the RF bias power is applied to the substrate to control the ion energy.

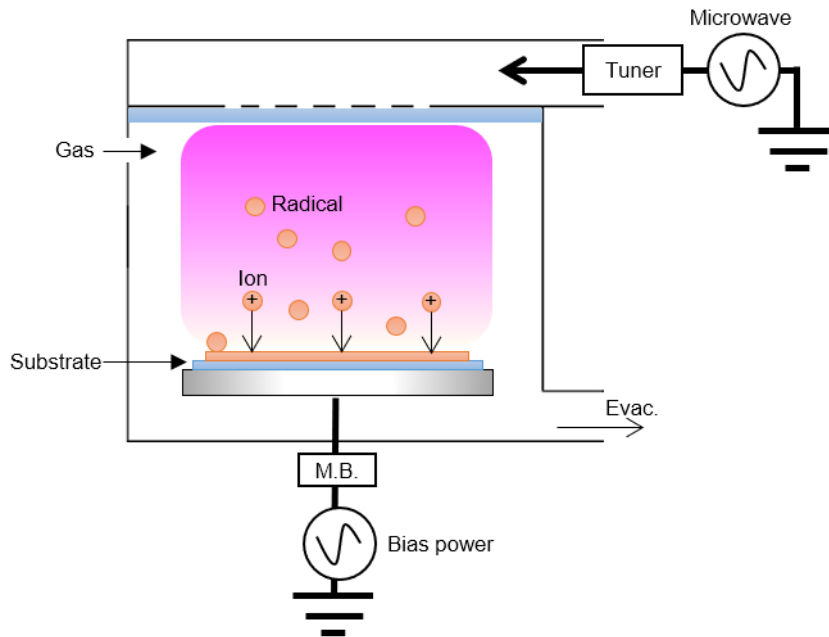


Figure 1.11 Schematic diagram of surface wave plasma with substrate bias power.

Table 1.1 Comparison of the electron density ( $n_e$ ) and the electron temperature ( $T_e$ ) among CCP, ICP, and SWP [38].

	CCP	ICP	SWP
$n_e$ (cm <sup>-3</sup> )	$\sim 10^{10}$	$\sim 10^{11-12}$	$\sim 10^{11-12}$
$T_e$ (eV)	$\sim 2$	$\sim 2-5$	$\sim 3$

Figure 1.12 shows a schematic diagram of the deposition of a-C film by PECVD [39]. In the case of PECVD, the ion subplantation occurs as well as ion beam deposition. Miyagawa et al. also reported that dynamic Monte Carlo simulation for the PECVD based on the subplantation model and it well represented experimental results [40]. When the bombardment energy of major carbon ions exceeds the penetration thresholds of the order of 30 eV, the ions can deeply penetrate the subsurface of the film [41]. Meanwhile, the penetrating ions induce the displacement of hydrogen and break the chemical bonds of carbon and hydrogen. The displacement of hydrogen occurs because the energy threshold for the displacement of hydrogen of 2.5 eV is exceeded [42]. This displacement of hydrogen leads to the formation of dangling bonds. The formation of dangling bonds at the surface is mandatory to grow the a-C films.

The  $\text{CH}_4$  plasma usually used for the deposition. In the  $\text{CH}_4$  plasma, main precursors are known as the  $\text{CH}_3$  and H. The  $\text{CH}_3$  radicals have a sticking coefficient of only  $10^{-4}$  to the surface, the film cannot grow itself [43]. The  $\text{CH}_3$  radicals seem to migrate on the deposition surface until sticking on surface dangling bonds or desorbing from the surface to the vapor. The hydrogen atoms are also known to create dangling bonds at the surface. The abstraction of hydrogen at the surface by incident hydrogen atoms creates dangling bonds. Keudell et al. reported H atoms induced  $\text{CH}_3$  chemisorption and  $\text{H}_2^+$  ions induced  $\text{CH}_3$  chemisorption [43]. They showed that the deposition rate of a-C film was enhanced when H atoms were irradiated simultaneously with  $\text{CH}_3$  radicals by the beam experiment. When the H atom flux increases, the growth rate increases because of the dangling bonds formation on the surface. The ions effects were also reported by their group. The  $\text{CH}_3$  radicals, H atoms,  $\text{H}_2^+$  ions were simultaneously irradiated to the sample and compared with the

$\text{CH}_3 + \text{H}$  atom cases. The results indicated that the  $\text{H}_2^+$  ion penetrates the subsurface (up to 8 nm depending on the ion energy) and H bonded with C was desorbed by the collision cascade. This means the H content of a-C films decreased by the  $\text{H}_2^+$  irradiation.

The study about the deposition mechanism of a-C films was conducted some researchers, however, the mechanism of film formation and its structure in the actual deposition is still unclear.

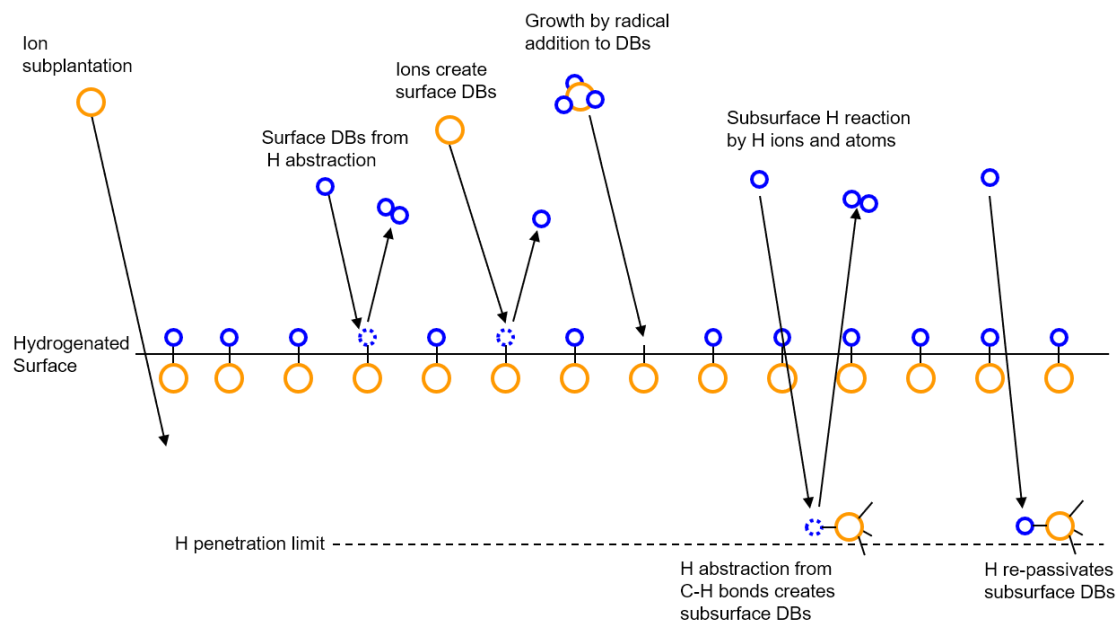


Figure 1.12 Schematic diagram of a-C deposition scheme by PECVD [39].

## 1.4 Objective and composition of this thesis

The purpose of this research is to elucidate the film formation mechanism of amorphous carbon films by a PECVD method using  $\text{CH}_4/\text{H}_2$  plasma. So far, Robertson et al. summarized the subplantation model as a mechanism to form  $\text{sp}^3$  bonds. Kuedell et al. reported the H desorption due to a collisional cascade of ions depends on the ion energy and the deposition of  $\text{CH}_3$  radicals due to the synergistic effect of H atom and  $\text{CH}_3$ . However, the growth mechanism in actual PECVD and a change in the film structure accompanying it have not been clarified. Moreover, the deposition of a-C films at the high temperature has not been reported a lot. Thus, the deposition mechanism is also still unclear for the high temperature deposition. In the current study, the objective is the clarification of the deposition mechanism of a-C films deposited by PECVD via comprehensively studies of the effects of internal parameters of plasma such as H atoms,  $\text{CH}_3$  radicals, ion bombardment of  $\text{H}_2$ ,  $\text{CH}_3$ , and  $\text{CH}_4$  ions at the deposition temperature of  $400^\circ\text{C}$  on the deposition characteristics, the films structure, and properties.

In this thesis, based on the film formation model described in Section 1.3.3, the effects of radicals and ions on a-C films will be explained in the following flow.

Chapter 2 describes the experimental methods of this research. In section 2.1, the deposition method of a-C films used in this research is described, which is called radical injection plasma-enhanced chemical vapor deposition system. Section 2.2 is about the plasma characterization, including negative self-bias voltage, electron density by plasma absorption probe (PAP), H excitation temperature instead of the electron temperature and relative radical density by optical emission spectroscopy (OES), and quantitative radical and neutral density by quadrupole mass spectroscopy (QMS). In this

section, the author introduced not only the basic measurement mechanism of these characterization approaches but also some practical details and important points during measurement in this research. Section 2.3 is about the film characterization, including the thickness measurement by stylus line profiler,  $sp^2$ -C cluster and the H content by visible Raman spectroscopy, the bonding structure by X-ray absorption spectroscopy (XAS), optical bandgap by spectrophotometer, conductivity by I-V measurements, dangling bonds density by the electron spin resonance (ESR) spectroscopy, and hardness by nanoindentation. Detailed deposition conditions are explained in the Methods section of each chapter.

In Chapter 3, the effects of H atoms and H ions on the deposition characteristics and film structure and properties are investigated. The author compared among the continuous deposition, sequential deposition with only heat treatment, H atom treatment, H plasma (H atoms + H ions) treatment. The deposited a-C films are evaluated regarding the thickness,  $sp^2$ -C clusters, PL background, density of dangling bonds, optical bandgap, conductivity. Then, the effects of H atoms and ions are discussed and summarized.

In Chapter 4, control of  $CH_3$  radical and its effects on  $sp^2$  fraction and hardness are investigated based on the residence time control. The results of plasma characterization by QMS and the  $sp^2$  fraction and the hardness of deposited a-C films are discussed. Finally, the effects of  $CH_3$  radical are summarized.

In Chapter 5, control of  $sp^2$ -C clusters in the a-C films based on the measurements of  $C_2$  radical density by actinometric OES are investigated. The plasma characterization was conducted by PAP, OES, and QMS. The visible Raman spectroscopy was carried out to measure the  $sp^2$ -C clusters in

the a-C films. Finally, the relationship between C<sub>2</sub> radical in the plasma and sp<sup>2</sup>-C clusters in the a-C films is summarized.

In Chapter 6, the ion bombardment energy flux is proposed, and its effects on the structure and electronic properties are investigated. The plasma characterization was conducted by PAP, OES, and QMS. The visible Raman spectroscopy was carried out to measure the sp<sup>2</sup>-C clusters and H content in the a-C films. The deposition rate, density of dangling bonds, optical bandgap, conductivity were measured. Finally, the deposition mechanism of a-C films based on the ion bombardment energy flux is summarized.

In Chapter 7, the author proposes new *in-situ* measurements method to observe the interaction between plasma and materials by the *in-situ* transmission electron microscope with the remote plasma source developed by the authors. Firstly, the demonstration of its effectiveness to elucidate the reaction mechanism, the etching of graphene by the O remote plasma is conducted. The TEM image, electron energy loss (EEL) spectra, and diffraction pattern are investigated. Finally, the layer-by-layer thinning of graphene is discussed.

In Chapter 8, all the results in the present study are summarized. Then, the deposition mechanism of the a-C films by PECVD is discussed based on the results in Chapter 3-6. The author proposes the deposition mechanism and the formation mechanism of the structure of a-C films.

The last part of this thesis is the remaining issues and future perspective.

## Chapter 2 Methods

### 2.1 Deposition of a-C films by radical injection plasma enhanced chemical vapor deposition (RI-PECVD)

It has been reported that a radical injection plasma-enhanced chemical vapor deposition (RI-PECVD) method can be used to control the generation of atomic H and hydrocarbon precursors independently [44–52]. Figure 2.1 shows a schematic diagram of the RI-PECVD system. This system comprises a stack of two plasma units, an SWP unit to generate H<sub>2</sub> plasma and a DF-CCP unit to generate hydrocarbon plasma. The two units are connected through multiple holes, and H generated in the SWP can be transferred to the DF-CCP unit. This system provides a wide range of control of the ratio of densities of H atoms to depositing precursors. Our group has reported the synthesis of carbon nanowalls (CNWs) with morphologies controlled by changing the ratio of H atoms in the RI-PECVD system [45,49,53–61]. In this system, ion bombardment energies on the surfaces of the films were controlled by changing the RF bias power. It has been reported that moderate ion energy is a key factor for the synthesis of a wide variety of a-C films [51,52,62].

The growth of a-C films was performed using an RI-PECVD system, in which two plasma sources were stacked and connected through a showerhead electrode [51,62]. The SWP was generated by 400 W in 2.45 GHz microwaves through a quartz window. The DF-CCP was generated by application of a 100 MHz VHF power ranging from 20 to 250 W to the showerhead for controlling the radical generation and by an application of 30-150 W, 13.56 MHz RF power to the sample stage for controlling a negative self-bias voltage ( $-V_{DC}$ ).

H<sub>2</sub> gas was introduced to the SWP region and generated the atomic H. The atomic H traveled to the lower DF-CCP region through the showerhead. A CH<sub>4</sub> gas was introduced to the DF-CCP chamber to generate hydrocarbon radicals. Flow rates of 16-500 sccm for CH<sub>4</sub> and 33-250 sccm for H<sub>2</sub> were conducted. The ratio of the flow rates, CH<sub>4</sub>/H<sub>2</sub>, was fixed to 2. This ratio significantly influenced the structure of the carbon materials [63–66]. The pressure measured at the DF-CCP region was at 1-12 Pa. The deposition time was 20 min.

Synthetic quartz square plates with 15 mm × 15 mm sizes and a thickness of 0.5 mm were used as substrates. The sample stage was heated to 550°C, which was measured by a thermocouple, and the temperature of the surface of the substrate during deposition was set around 400°C, which was measured by an infrared thermometer (KTL-PRO, LEC company Ltd). Before the deposition process, seasoning of the reaction chamber was conducted for 5 min using identical conditions to the deposition but without heating.

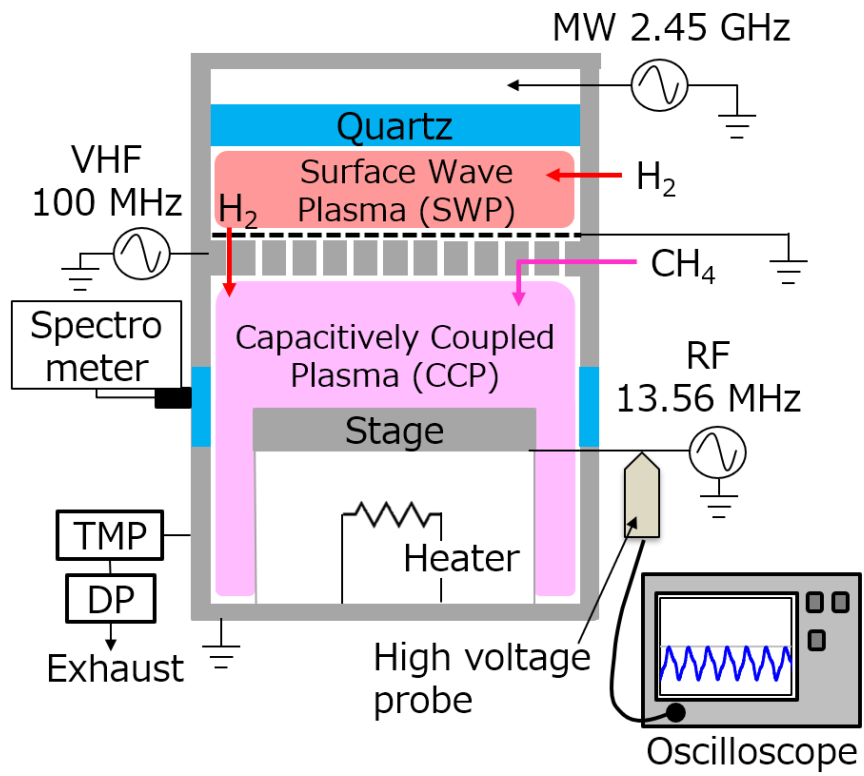


Figure 2.1 The schematic diagram of an RI-PECVD system.

## 2.2 Plasma characterization

### 2.2.1 Negative self-bias voltage

To measure  $-V_{DC}$ , an oscilloscope was connected to the lower electrode through the high voltage probe (P6015A, Tektronix) and low pass filter with a 20 MHz cut off frequency. Figure 2.2 shows a typical waveform of the RF bias voltage of RI-PECVD. The author determined the average voltage as the  $-V_{DC}$ .

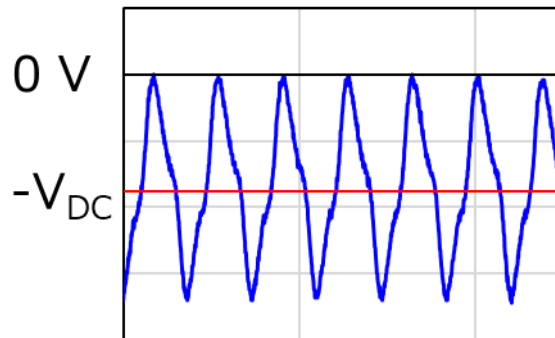


Figure 2.2 The waveform of the RF bias voltage of RI-PECVD system.

### 2.2.2 Plasma absorption probe (Electron density)

The electron density was measured by the Plasma Absorption Probe [67–71]. The antenna probe comprising a coaxial cable with a quartz tube was introduced to the DF-CCP region. The probe position was at the center of the electrode gap and near the edge of the stage in the chamber. The antenna length, which was defined as a stripping length of the coaxial cable, i.e., the unshielded region inside the quartz tube, was 6 mm. This length determined the characteristics of the fundamental absorption by the surface wave. The

absorption signals were collected by the network analyzer (E5071C, Agilent Technologies) with a power limiter (11930B, Agilent Technologies) and a high pass filter (NHP-150+, Mini-Circuits). Figure 2.3 shows the reflectance spectra of the microwave. The center frequency of the resonant peaks on the measured dispersion curves was determined by fitting Lorentzian functions to the peaks. The electron densities were calculated using the center frequencies ( $f_{SW}$ ) of the resonant peaks by the following equation [71].

$$n_e [cm^{-3}] = 1.24(1 + \varepsilon_d)f_{SW}^2 \times 10^{10} \quad (2-1)$$

where  $n_e$  is the electron density,  $\varepsilon_d$  is the dielectric constant of the probe quartz tube (relative permittivity of 3.78), and the unit of  $f_{SW}$  is GHz.

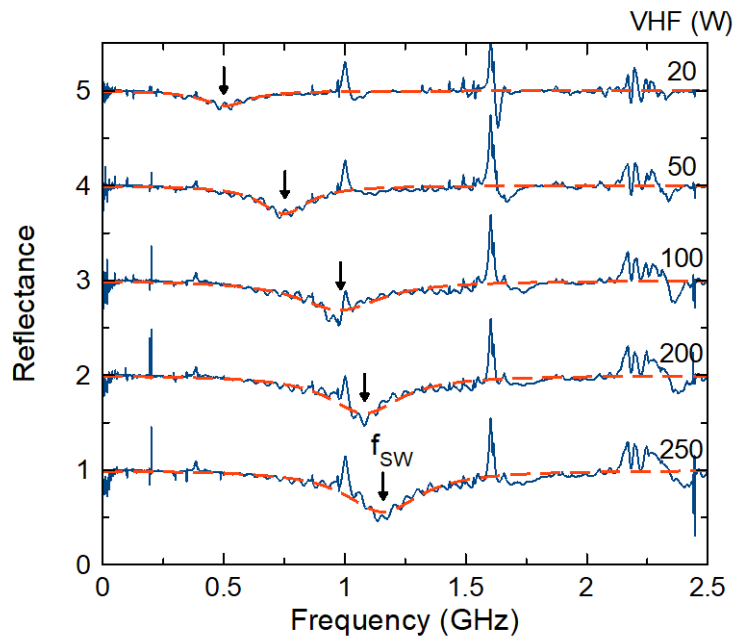


Figure 2.3 The reflectance spectra of the microwave as a function of frequency. Orange dash lines are Lorentzian fit results.

### 2.2.3 Optical emission spectroscopy (Electron temperature and radical species)

Particles in plasma are excited as well as dissociated and ionized by collisions with electrons. When excited particles return to a stable energy state, some of them emit energy as light.

Optical emission spectra were taken by a spectrometer (HR-2000 CG and USB2000+, Ocean Optics) using an optical fiber, and the light was collected through a quartz window in DF-CCP chamber.

Actinometric optical emission spectroscopy was carried out to evaluate the relative density of radicals in the plasma by adding a trace amount of Ar gas, as proposed by Coburn and Chen [72]. For the analysis of actinometry, the background for each emission peak was subtracted by the linear line before taking the ratio of each emission intensity.

The optical emission intensity of particle X,  $I_X$  can be described as

$$I_X = N_X n_e \int v \sigma(v) f(v) dv \propto k_X n_e N_X \quad (2-2)$$

where  $k_X$  is an excitation rate constant of particle X,  $n_e$  is an electron density,  $N_X$  is a density of ground state particles of X.

In the actinometry method, the density change of a particle X in the plasma is measured by the emission intensity ratio of particle X and a noble gas atom which does not contribute much to the reaction in a plasma such as Ar. From the equation (2-2), the intensity ratio can be written as follows.

$$\frac{I_X}{I_{Ar}} = \frac{k_X N_X}{k_{Ar} N_{Ar}} \quad (2-3)$$

When  $N_{Ar}$  is constant because of the constant flow rate,  $N_X$  can be obtained from the intensity ratio as,

$$N_X = \frac{k_X}{k_{Ar}} \frac{I_X}{I_{Ar}} \quad (2-4)$$

where  $k$  depends on the electron temperature ( $T_e$ ). If the  $T_e$  was constant,  $N_x$  can be directly compared by the  $I_x/I_{Ar}$ .

Comparing hydrogen Balmer line intensity of alpha and beta, the excitation temperature of H atoms was estimated on the hypothesis of Local Thermodynamic Equilibrium (LTE) by following equation [73].

$$\frac{I_{H\alpha}}{I_{H\beta}} = \frac{\lambda_{H\beta} A_{H\alpha} g_3}{\lambda_{H\alpha} A_{H\beta} g_4} \exp\left(-\frac{E_i - E_k}{k_B T}\right) \quad (2-5)$$

where  $I$  is the optical emission intensity,  $\lambda$  is the wavelength of emission line,  $A$  is the transition probability,  $g$  is the degeneracy,  $E_i$  and  $E_k$  are the energy of state  $i$  and  $k$ , respectively,  $k_B$  is the Boltzmann constant,  $T$  is the excitation temperature. The optical emission intensity was calibrated by the reference light source (SL1-CAL, Tokyo Instruments) and subtracted background by the linear baseline.

### 2.2.4 Quadrupole mass spectroscopy (Radical and ion species)

A quadrupole mass spectrometer (EQP 500, Hiden Analytical Ltd.) was equipped to the DF-CCP chamber as shown in Fig.2.4. An orifice with a 100- $\mu\text{m}$ -sized hole was used. Neutral species were measured using appearance mass spectroscopy. In this experiment, the electron energy for ionization was fixed at 13 eV for detecting neutral species based on the appearance potential of molecules. Densities of the neutral species were estimated by the following equation, as described in detail elsewhere [74]. The QMS output signal intensity of particle X ( $I_X$ ) is described by

$$I_X = \alpha\beta\sigma_X I_{beam} N_X \nu \quad (2-6)$$

where  $\alpha$  is the sensitivity of the QMS,  $\beta$  is the vacuum conductance of particle X,  $\sigma_X$  is the electron impact ionization cross-section of particle X,  $I_{beam}$  is the electron beam current for electron impact ionization,  $N_X$  is the density of particle X, and  $\nu$  is the number of collisions in the ionization part of the QMS. Assuming that (i)  $\alpha$  depends on only the QMS system and (ii)  $\beta$  and  $\nu$  do not change with each particle X, the density of particle X ( $N_X$ ) is given by

$$N_X = \frac{\sigma_{CH_4}}{\sigma_X} \frac{I_X}{I_{CH_4}} N_{CH_4} \quad (2-7)$$

where  $I_{CH_4}$  was obtained under the deposition condition when the plasma was off.  $N_{CH_4}$  was calculated from the pressure, Avogadro constant ( $N_A$ ), and gas temperature (300 K).  $I_X$  can be determined from a species with known cross-section at a measured ionization electron energy of 13 eV.

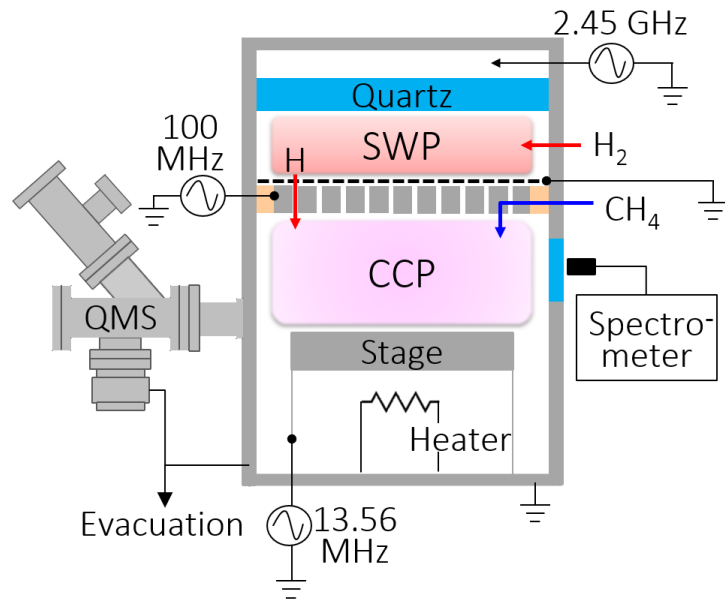


Figure 2.4 The RI-PECVD system equipped QMS.

## **2.3 Film characterization**

### **2.3.1 Line profiler (Thickness)**

The thickness of a-C films is determined by a stylus profiler (Alpha-Step IQ, KLA-Tencor). A stylus scans on the surface of solid materials, and the difference of the height between substrate and a-C film was determined as the thicknesses of a-C films.

The thickness was determined as an average of the 4 points of the steps to decrease the error from the position of a-C films.

### 2.3.2 Visible Raman spectroscopy ( $sp^2$ -C clusters and H content)

The crystallinities of the  $sp^2$ -C clusters of the deposited a-C films were analyzed by visible Raman spectroscopy (inVia Reflex Raman microscope, Renishaw) with an excitation power of 0.25 mW from a 532 nm laser. An objective lens of  $\times 50$  was used to collect Raman signals. Raman spectra were obtained by accumulating 20 spectra taken at an integration time of 1 s for a good signal to noise ratio and to avoid damage by the laser irradiation.

Figure 2.5 shows the Raman spectrum of a-C film deposited by RI-PECVD. It is well known that Raman spectra of amorphous carbon are dominated by the  $sp^2$ -C because of the much greater cross-sectional areas of the  $\pi$  states than the  $\sigma$  states [75–77]. The G band appears at around  $1580\text{ cm}^{-1}$ . The G band consists of the three types of  $sp^2$ -C clusters, such as nc-G, nR, and nC, as mentioned before [78]. In addition to the G band, the D band appears at around  $1350\text{ cm}^{-1}$ . This mode is forbidden in perfect graphite and only becomes active in the presence of disordered six-membered rings [77]. There are reports concerning the relationship between G band position and a-C film structures [79].

In Raman spectroscopic characterizations, these  $sp^2$ -hybridized bonding properties of a-C films appear in the peak positions and widths for both G and D bands [80,81]. In particular of G band, the peak positions are known to correlate with contents of nanocrystalline graphite (nc-G), fused aromatic ring (nR), and olefinic chain nanocluster (nC) [78,79]. The  $sp^2$ -C characteristics in a-C films are considered to cause decreases in their densities and hardnesses [16]. Figure 2.6 shows the relationship between the variations of G band position (G position) and the full widths at half maxima (FWHM) of the G band ( $FWHM_G$ ) as reported for various kinds of a-C films by Rose et al. and Merlen et al. [79,81]. A control method of  $sp^2$ -clusters in a-

C films has developed based on the relationship between the G position and the  $\text{FWHM}_G$ . For the visible Raman spectra, the higher shift of the G position shows the change from nR to the nc-G of  $\text{sp}^2$ -C clusters, but no relation with nC. The  $\text{FWHM}_G$  indicates the configuration of local disorder bonds, which can be related to the size of  $\text{sp}^2$ -C clusters and/or the  $\text{sp}^3$  content close to  $\text{sp}^2$ -C bonds. Therefore, the plot of G position versus the  $\text{FWHM}_G$  was proposed to estimate the a-C structure in literatures [79,81].

In general, the H containing a-C films, usually deposited by the PECVD, shows the high intensity of the background signal, because the recombination of excited electrons depends on the H content. Therefore, this PL background is often used to estimate the H content [80–84]. However, it should be noted that the dangling bonds density in the a-C film can also increase the PL background as Rose et al. reported [81]. The intensity ratio of the PL background to G-band peak ( $\text{Slope}/I_G$ ), increased with increasing post-annealing temperature, because of the passivation of the dangling bonds [81]. According to the molecular dynamic (MD) simulation, an increase of the number of C=C double bonds without changing the number of H atoms and C-H bonds suggested that the dangling bonds vanish as results of  $\text{sp}^2$  clustering and C reorganization. Conversely, this result also suggested that, if the density of dangling bonds hardly changed or decreased depending on any process conditions, an increase in the  $\text{Slope}/I_G$  indicates an increase of the H content.

Raman spectral feature was decomposed with two Gaussians for G and D bands [80,81]. The peak fitting was performed after subtraction of the background signal arisen from the photoluminescence (PL) by a linear fit with ranges of 920-970 and 1800-1950  $\text{cm}^{-1}$ . The evolution of the hydrogen content was estimated using the ratio of PL slope to G band peak (around 1580  $\text{cm}^{-1}$ )

intensity ( $I_D/I_G$ ) [81,82,85]. The peak fitting was performed by the algorithm of Levenberg-Marquardt.

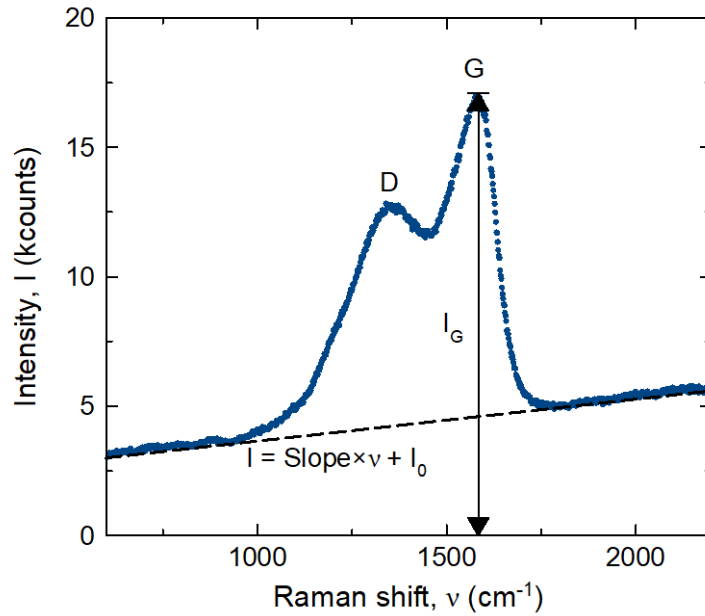


Figure 2.5 Typical Raman spectrum of a-C films deposited by RI-PECVD. The background can be described as a linear function.

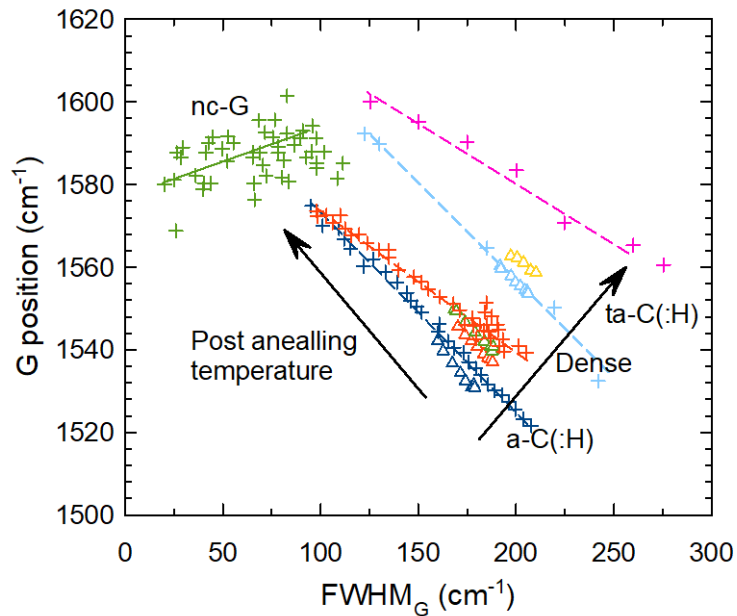


Figure 2.6 The plot of the variation of G position versus  $FWHM_G$ . ( $\Delta$  Rose et al., + Merlen et al., see details in Ref [81] and [79])

2.3.3 X-ray absorption spectroscopy and Near-edge X-ray absorption fine structure (bonding structure and  $sp^2$ -C content) To distinguish the bonding structure, near edge X-ray absorption structure (NEXAFS) spectroscopy is a highly informative experimental method [83,86–89]. Carbon K-edge NEXAFS methods have been well established for organic and polymer materials [90,91]. The NEXAFS measurement was carried out at the Aichi Synchrotron Radiation Center, Japan, on beamline 7U. The energy resolution was 0.1 eV at the carbon K edge. The NEXAFS spectra were obtained in total electron yield (TEY) mode, with an energy step of 0.1 eV for the range of 281-294 eV, 0.5 eV for the range of 294-300 eV and 1.0 eV for other energy ranges. The intensity of the incident photon beam ( $I_0$ ) was measured using a Si photodiode in the system (Fig. 2.7), and the electron current intensity from the sample ( $I_S$ ) was measured using an ammeter connected between the sample stage and ground (Fig. 2.8). The absorption signal was given by the ratio  $I_S/I_0$ . Highly oriented pyrolytic graphite (HOPG) was used as a reference sample to calculate the  $sp^2$  fractions of the a-C films. All the spectra of a-C films and HOPG were measured at an incident angle of  $54.7^\circ$  from the sample surface, which is known to be a magic angle for eliminating the orientation of bonding orbital. The X-ray incident angle from the sample surface for HOPG quite affects the quantification of  $sp^2$  fraction because of the high orientation of  $\pi^*$  orbitals. The  $\pi^*$  peak intensity is quite different with different X-ray incident angle [92]. Recently, Mangolini et al. reported that the X-ray incident angle should be  $45^\circ$  to equally contribute the  $\pi^*$  and  $\sigma^*$  transition to the NEXAFS spectra [92]. However, when the X-ray incident angle is  $54.7^\circ$ , so-called magic angle, the contribution of  $\pi^*$  and  $\sigma^*$  transition is independent on the orientation of  $\pi^*$  and  $\sigma^*$  orbitals and always constant [93]. Muramatsu and Gullikson reported that the intensity ratio of  $\pi^*$  and  $\sigma^*$  of HOPG is same as

Single-Walled Carbon Nano Tube (SWCNT), Multi-Walled Carbon Nano Tube (MWCNT) and Carbon Black (CB), which are considered as non-orientation materials, when the X-ray incident angle is magic angle [94]. Therefore, the magic angle of the X-ray incident angle was used for both a-C films and HOPG reference. The spectrum of HOPG which was used as a reference is shown in Fig. 2.9.

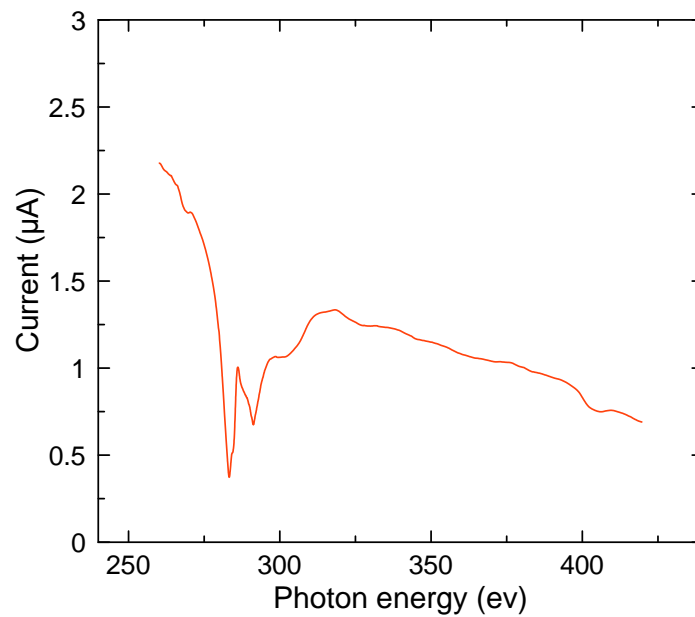


Figure 2.7 The reference synchrotron radiation intensity measured by a Si Photodiode.

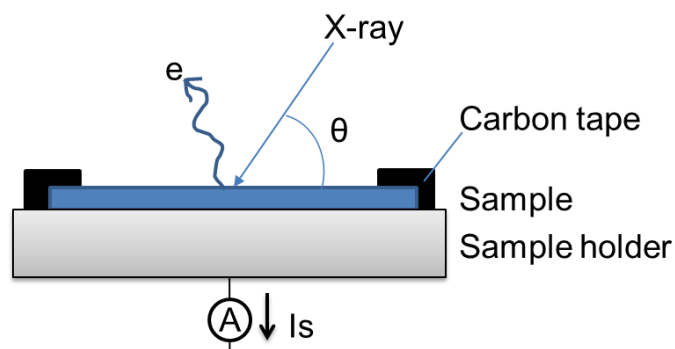


Figure 2.8 The schematic diagram of the X-ray absorption spectroscopy in a total electron yield mode.

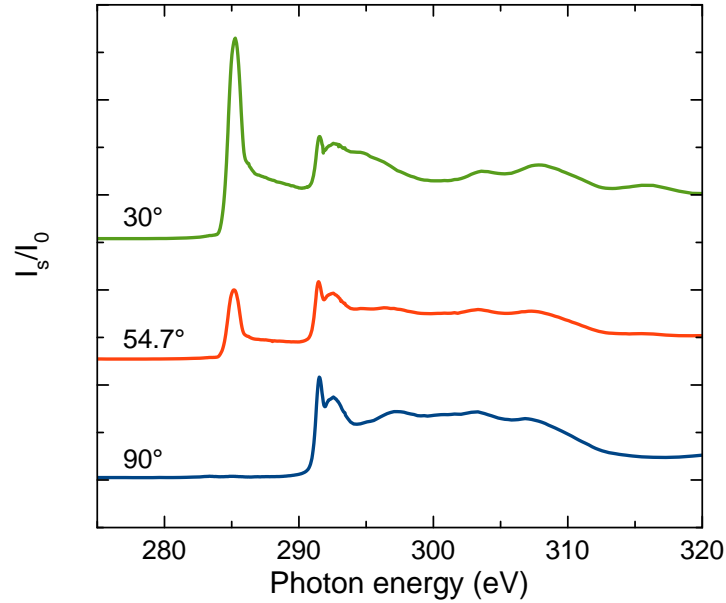


Figure 2.9 The NEXAFS spectra of HOPG with X-ray incident angles of  $30^\circ$ ,  $55^\circ$ , and  $90^\circ$ .

An  $sp^2$  fraction was calculated from NEXAFS spectra by many researchers [87,92,95–99]. The method is similar to that of an  $sp^2$  fraction in Electron Energy Loss Spectroscopy (EELS). The  $sp^2$  fraction was calculated by taking a ratio of two windows (in spectral ranges) for NEXAFS, described as

$$sp^2 \text{ fraction [\%]} = \frac{(I_{\pi^*}/I_{\sigma^*})_{a-C}}{(I_{\pi^*}/I_{\sigma^*})_{Ref}} \times 100 \quad (2-8)$$

where  $I_{\pi^*}$  is the peak area of the  $\pi^*$  C=C at 285 eV and  $I_{\sigma^*}$  is the integrated signal intensity with an energy window for a-C films and a reference material with 100 %  $sp^2$  fraction [96]. The author used the integrations energy windows of  $I_{\sigma^*}$  of 291-307 eV [52].

### 2.3.4 Spectrophotometer (Optical bandgap)

The optical properties were measured by a spectrophotometer (V-670, JASCO), in the ultraviolet-infrared spectral region (200–2500 nm). The absorbance of the a-C film deposited on the synthetic quartz substrate was measured.

From the absorbance (*Abs*) obtained by spectrophotometry, the extinction coefficient ( $\alpha$ ) was obtained from the following formula.

$$Abs = -\log_{10} \frac{I}{I_0} \approx 0.434\alpha L \quad (2-9)$$

where  $I_0$  is the transmitted light intensity of the synthetic quartz,  $I$  is the transmitted light intensity of the a-C film deposited on the synthetic quartz, and  $L$  is the optical path length, that is, the film thickness.

However, in amorphous materials, there is no long-range order, and there are many disturbances in the chemical bond structure, so there is no clear absorption edge like crystals. Also, due to a lack of structural order, three absorption regions were observed and classified by Tauc et al. [8, 9] as follows

$$\alpha < 1 \text{ cm}^{-1} \quad \alpha \sim e^{hv/E_t} \quad (2-10)$$

$$1 < \alpha < 10^4 \text{ cm}^{-1} \quad \alpha \sim e^{hv/E_1} \quad (2-11)$$

$$10^4 \text{ cm}^{-1} < \alpha \quad hv\alpha \sim C(hv - E_g)^2 \quad (2-12)$$

The optical band gap of the amorphous material is defined by  $E_g$  in Eq. (2-12) and is often used for a-Si, a-Ge. This optical band gap is called a Tauc gap. A linear region appears by plotting the ordinate with  $\sqrt{h\nu\alpha}$  and the abscissa with  $h\nu$ , and the intersection point of the approximate straight line and the abscissa is defined as the optical band gap (Fig. 2.10).

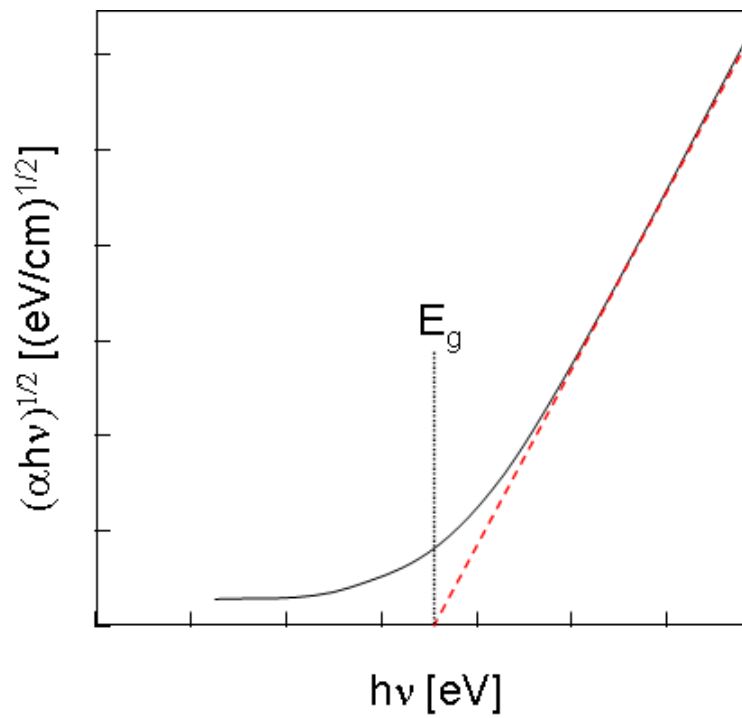


Figure 2.10 The schematic diagram of the Tauc plot.

### 2.3.5 I-V measurements (Conductivity)

The electrical conductivity of the as-deposited film was measured by I-V measurement using a source measure unit (B2901A, Agilent Technologies). The measurement was conducted by a 4 wire method. The 150 nm thickness of Au comb electrode was deposited by electron beam deposition. The structure of the comb electrode is shown in Fig 2.11.

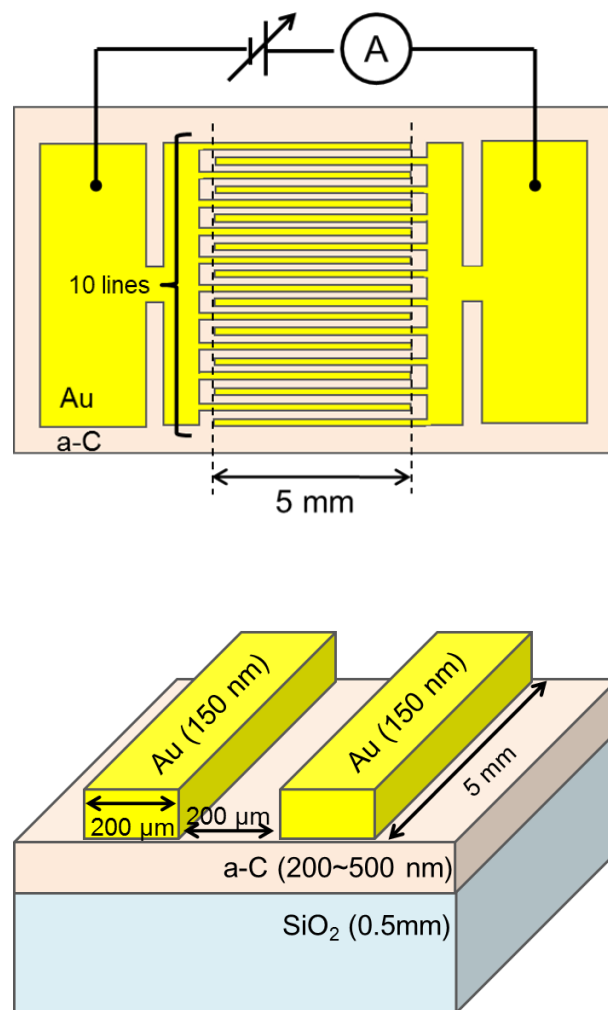


Figure 2.11 Comb electrode structure (top) and sample structure (bottom).

### 2.3.7 Electron spin resonance (Dangling bonds)

To study the density of dangling bonds, electron spin resonance (ESR) measurements were carried out at room temperature using an X-band ESR spectrometer (EMX-plus, BRUKER) with 100 kHz modulation of the magnetic field. The density of dangling bonds was estimated using a reference sample of  $\text{CuSO}_4 \cdot 5\text{H}_2\text{O}$  (number of spins;  $6.5 \times 10^{18}$ ).

Figure 2.12 shows the typical ESR spectra of a-C film. The signal intensity of ESR can be described as

$$\iint I dH = k\sqrt{P_{MW}}A_{mod}G_{rec}n_{scans}T_{conv}N_s \quad (2-13)$$

where  $I$  is the intensity of as-recorded spectra,  $H$  is the magnetic field,  $k$  is the equipment function,  $P_{MW}$  is the microwave power,  $A_{mod}$  is the modulation amplitude,  $G_{rec}$  is the receiver gain,  $n_{scans}$  is the number of scans,  $T_{conv}$  is the conversion time, and  $N_s$  is the number of spins.  $N_s$  can be calculated by taking ratio to a reference sample. The density of dangling bonds is calculated from dividing  $N_s$  by the volume of measured sample.

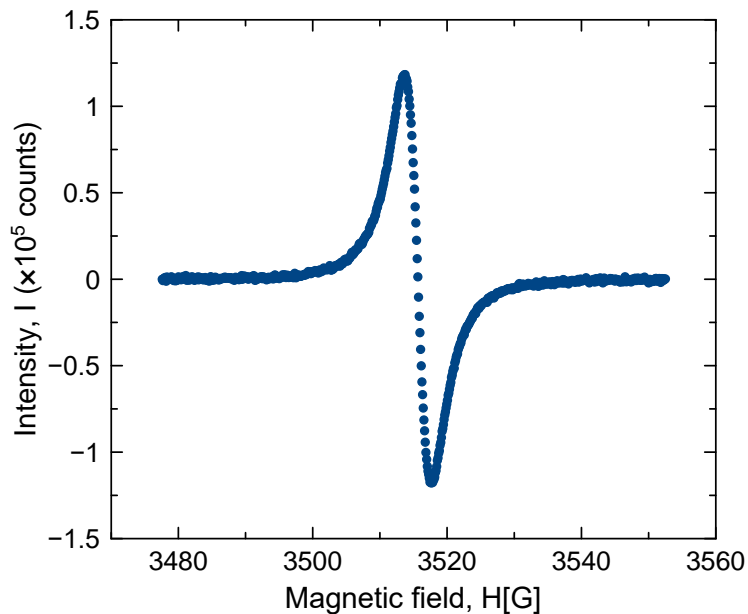


Figure 2.12 Typical ESR spectrum of a-C film.

### 2.3.8 Nanoindentation (Hardness)

The hardnesses of the a-C films were measured by Nanoindenter (ENT-1100a, Elionix) with Berkovich tip. Hardness ( $H$ ) can be calculated from the following equation,

$$H = \frac{L_{max}}{A_i} \quad (2-14)$$

where  $L_{max}$  is the maximum load, and  $A_i$  is the surface area of indentation.  $A_i$  for Berkovich tip can be described as

$$A_i = 23.96 \times (h_{max} - \varepsilon(h_{max} - h_c)) \quad (2-15)$$

where  $h_{max}$  is maximum indentation depth,  $h_c$  is the contact depth,  $\varepsilon$  was correction coefficient by ‘Tanaka method.’

Figure 2.13 shows the schematic plot of load versus indentation depth from the nanoindentation test. The hardness was calculated from this plot and determined by the average of 15 measurement points.

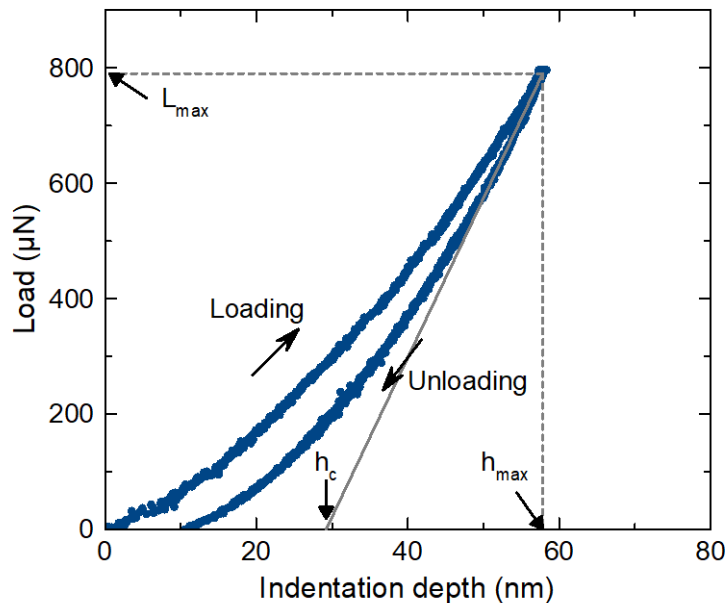


Figure 2.13 Schematic plot of load versus depth from nanoindentation test using Berkovich tip.

## **Chapter 3 The effects of H atoms and H ions on the film properties of a-C films**

In this chapter, the author discusses the effects of H atoms and H ions on the a-C structure. The effect of H atoms was reported that H abstraction from the surface C-H by Keudell et al. as mentioned before [43]. In the current research, the author compares the H atom irradiation and H plasma irradiation including H atoms and H ions by a sequential deposition method. In the sequential deposition, the deposition and H<sub>2</sub> plasma irradiation are alternatively repeated. In the current study, the author conducted the 4 process conditions; (A) continuous deposition, (B) deposition with 30 s interval, (C) deposition with H atom irradiation for 30 s, and (D) deposition with H atom and ion irradiation for 30 s. The thickness, sp<sup>2</sup>-C clusters, and PL background (Slope/I<sub>G</sub>), optical bandgap, conductivity were measured.

### 3.1 Experimental details

Figure 3.1 shows a process procedure of (A) continuous deposition, (B) deposition with 30 s interval, (C) deposition with H atom irradiation for 30 s and (D) deposition with H atom and ion irradiation for 30 s.

The heater was kept running at 550° C during the whole deposition including the interval and H plasma treatment. A total deposition time of all processes was 20 min. The detail discharge conditions are shown in Table 3.1. Each process is named as, (A) Continuous, (B) Interval, (C) H atom, and (D) H atom/ion.

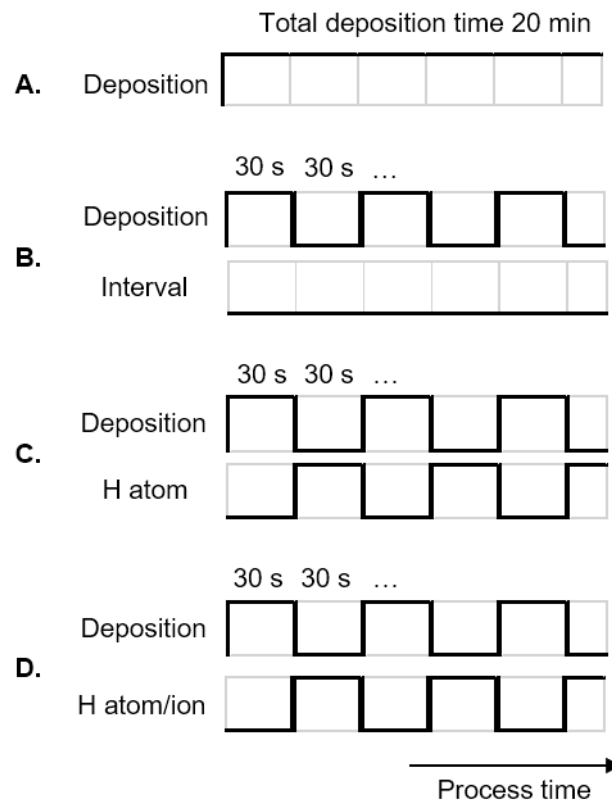


Figure 3.1 Process procedure of each condition. (A) continuous deposition, (B) deposition with 30 s interval, (C) deposition with 30 s H atom irradiation, and (D) deposition with 30 s H atom/ion irradiation.

## (A) continuous deposition (Continuous)

Figure 3.1(A) shows the process for continuous deposition. In this case, the deposition process continuously kept for 20 min. Figure 3.2 shows the schematic diagram of the continuous deposition. CH<sub>4</sub> plasma was generated by DF-CCP for the deposition. H<sub>2</sub> was not introduced chamber for deposition in the current chapter. VHF and RF bias power were applied to upper and lower electrodes, respectively. And, microwave power was not applied for the deposition.

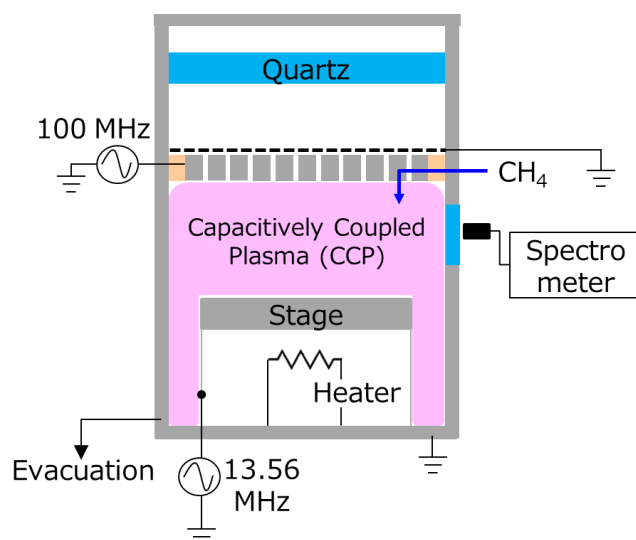


Figure 3.2 The schematic diagram of continuous deposition (A).

## (B) deposition with 30 s interval (Interval)

Figure 3.1(B) shows the process for the deposition with 30 s interval. The cycle of 30 s deposition and 30 s interval was repeated 40 times. Figure 3.3 shows the schematic diagram of deposition with 30 s interval. The deposition was conducted as the same condition as (A) continuous deposition for 30 s. In the latter half 30 s, the plasma was not generated, and no gas was flown into the chamber. The pressure during the interval process was  $10^{-4}$  Pa. So that, during the interval process, the a-C film was annealed in the vacuum.

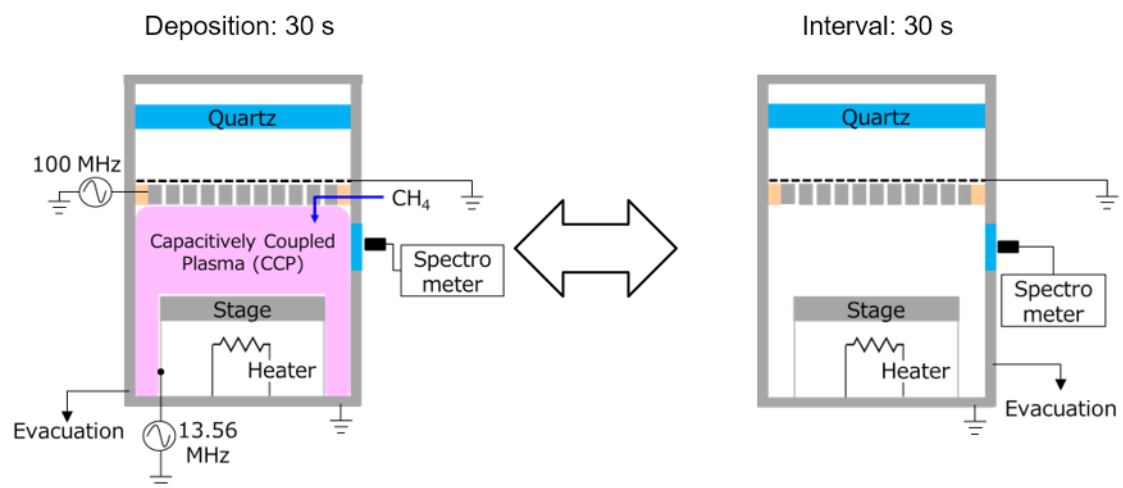


Figure 3.3 The schematic diagram of deposition with 30 s interval (B).

(C) deposition with H atom irradiation for 30 s (H atom)

Figure 3.1(C) shows the process for the deposition with 30 s H atom irradiation. The cycle of 30 s deposition and 30 s H atom irradiation was repeated 40 times. Figure 3.4 shows the schematic diagram of deposition with 30 s H atom irradiation. The deposition was conducted as the same condition as (A) continuous deposition for 30 s. In the latter half 30 s, H plasma was generated with SWP. The surface treatment was carried out using SWP, which enables to treat only with H atom because ions cannot reach the substrate because ground mesh and showerhead electrode prevent the ions. The pressure was set to 1 Pa to reduce the collisional loss of atomic H on the way from the showerhead electrode to the stage based on the mean free path of atomic H.

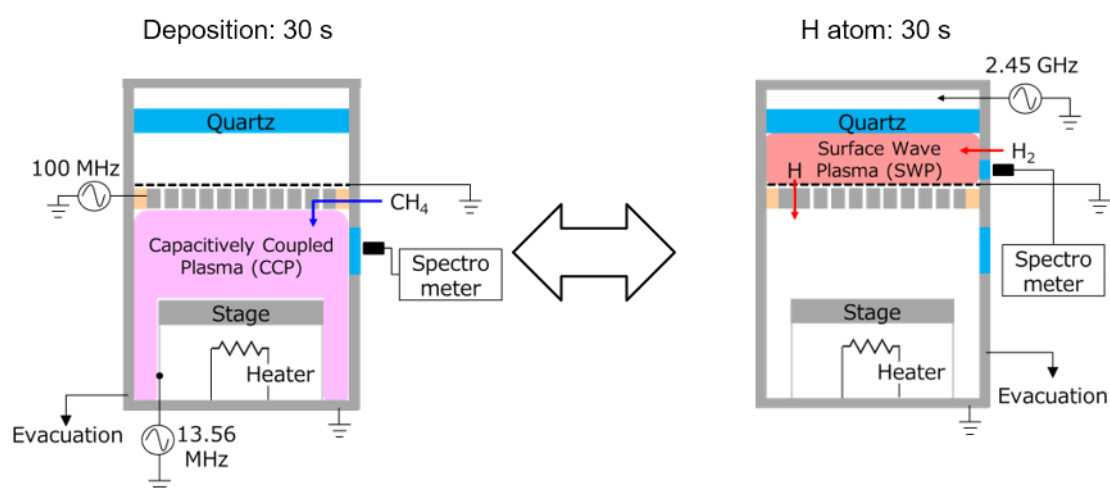


Figure 3.4 The schematic diagram of deposition with H atom irradiation for 30 s (C).

(D) deposition with H atom and ion irradiation for 30 s (H atom/ion)

Figure 3.1(D) shows the process for the deposition with 30 s H atom/ion irradiation. The cycle of 30 s deposition and 30 s H atom/ion irradiation was repeated 40 times. Figure 3.4 shows the schematic diagram of deposition with 30 s H atom/ion irradiation. The deposition was conducted as the same condition as (A) continuous deposition for 30 s. In the latter half 30 s, H plasma was generated with CCP without RF bias power. The pressure was set to 5 Pa. The stage was a floating potential which is usually a few tens Volts, and H ions have bombarded the substrate with the kinetic energy of floating potential. The surface treatment was performed with H atoms and H ions (including light).

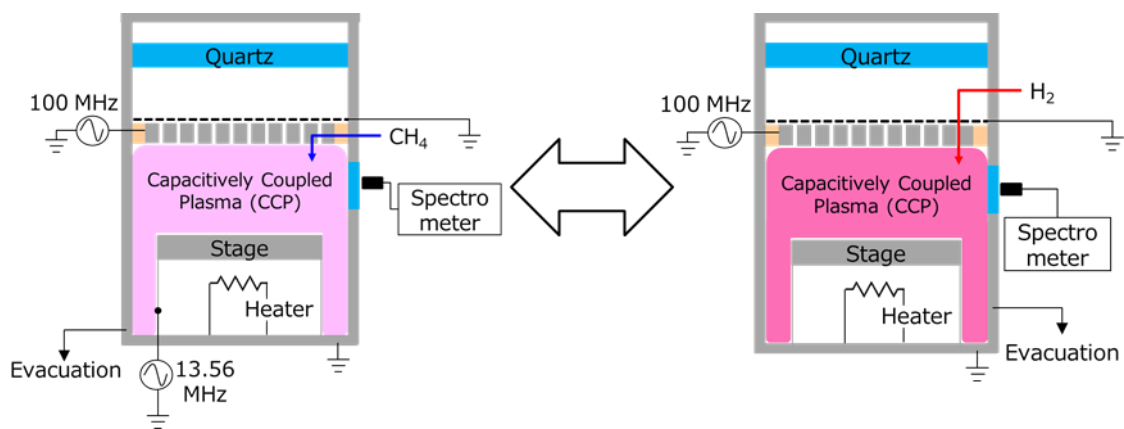


Figure 3.5 The schematic diagram of deposition with H atom/ion irradiation for 30 s (D).

Table 3.1 The process conditions of the sequential deposition.

	Deposition	Interval	H atom	H atom/ion
Microwave power (W)	0	0	800	0
VHF power (W)	100	0	0	100
RF bias power (W)	50	0	0	0
Stage temperature (°C)	550	550	550	550
Pressure (Pa)	5	10 <sup>-4</sup>	1	5
H <sub>2</sub> into SWP chamber (sccm)	0	0	30	250
H <sub>2</sub> into CCP chamber (sccm)	0	0	0	0
CH <sub>4</sub> (sccm)	500	0	0	0
Gap between electrode (mm)	30	30	30	30

## 3.2 Results and discussion

Figure 3.6 shows the film thickness of the a-C films prepared in this chapter. Continuous is treated as a reference. The film thickness increased with an interval. The film thickness also increased with H atom irradiation. On the other hand, the film thickness decreased with H atom/ion irradiation.

Increase in film thickness with an interval is thought to be due to high-density discharge when the plasma was turned on in every cycle or the H abstraction by the annealing effect in a vacuum. In the case of H atom irradiation, the thickness further increased compared with the case with an interval. H atoms react with hydrogen on the surface of the a-C film to form hydrogen molecules and surface dangling bonds. Due to the increase of the sticking probability of  $\text{CH}_3$  radicals by the generation of surface dangling bonds, the deposition rate increased. On the other hand, it is conceivable that H atoms and H ions etch the a-C film.

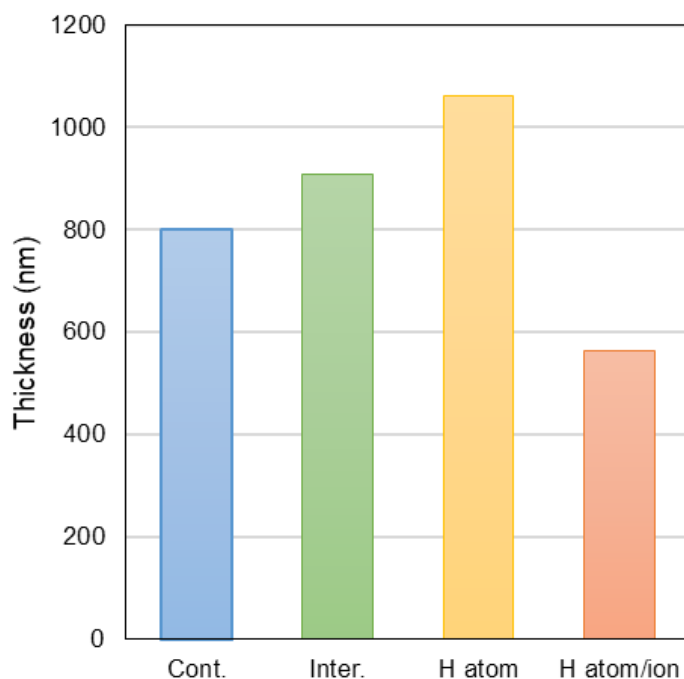


Figure 3.6 Thickness of as-deposited a-C films.

Figure 3.7 shows the Raman spectra of as-deposited a-C films. The G and D bands were observed. The background signal of PL was significantly changed only in the case of the H atom/ion irradiation. Figure 3.8 shows the normalized Raman spectra to compare the change of G and D bands. The continuous shows the highest D band intensity. However, the interval, the H atom irradiation, and the H atom/ion irradiation cases are almost same shapes of the peaks.

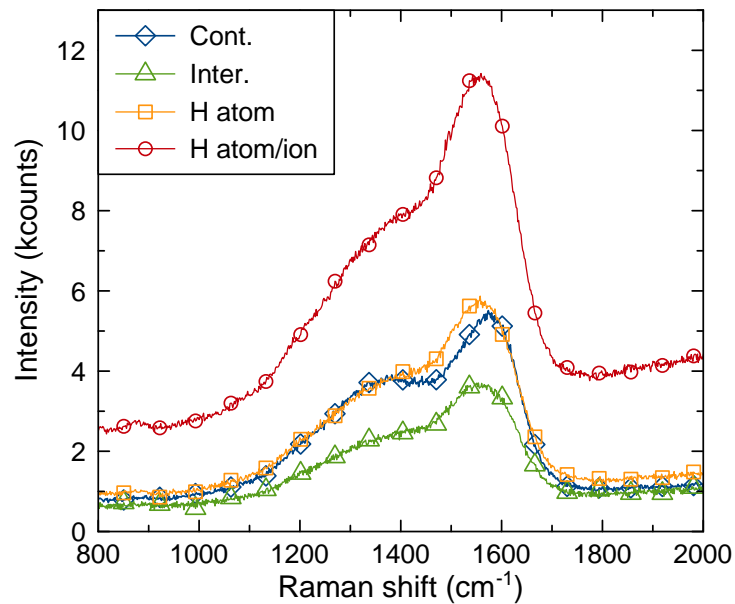


Figure 3.7 Raman spectra of as-deposited a-C films.

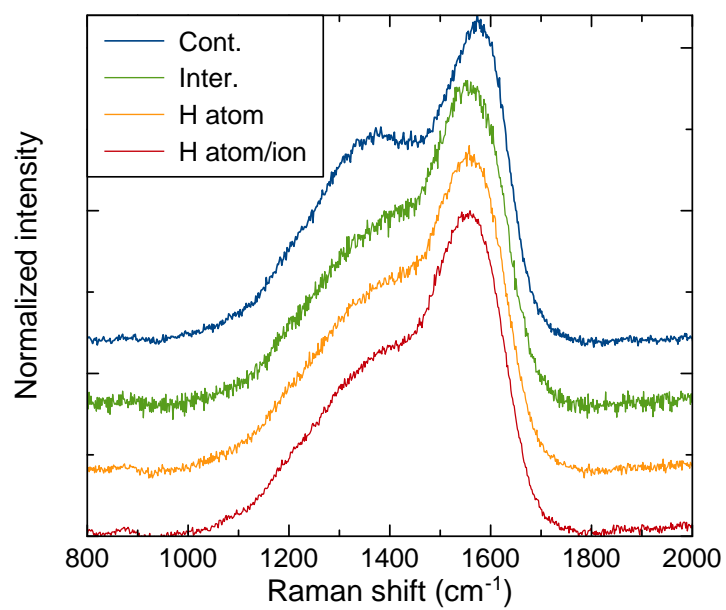


Figure 3.8 Normalized Raman spectra of as-deposited a-C films.

Figure 3.9 shows the  $I_D/I_G$  of as-deposited a-C films. Compared with the continuous case, the interval, the H atom irradiation, and the H atom/ion irradiation cases showed the lower values. The difference between the interval and H atom/ion irradiation cases is small, and the  $I_D/I_G$  of the H atom irradiation case is a little high. This indicates that the H atom enhances the  $sp^2$ -C cluster size.

Figure 3.10 shows the G position as a function of  $FWHM_G$ . The a-C films deposited with the sequential deposition mode shows the lower G position and broader  $FWHM_G$  than that of the continuous deposition. The difference among the sequential depositions with an interval, H atom irradiation, and H atom/ion irradiation cases are small.

Figure 3.11 shows the PL background and G band intensity ratio,  $Slope/I_G$ . Interval and H atom irradiation cases show almost the same  $Slope/I_G$ . The H atom/ion irradiation shows the highest value. The increase of  $Slope/I_G$  indicates that a decrease of non-radiative recombination sites, which is usually dangling bonds, or the increase of the H content in the film. To confirm this, the density of dangling bonds was measured as shown in Fig. 3.12. The densities of dangling bonds of continuous, interval and H atom irradiation cases are almost  $1 \times 10^{20} \text{ cm}^{-3}$ , on the other hand, that of H atom/ion irradiation case is  $0.4 \times 10^{20} \text{ cm}^{-3}$ . It still cannot distinguish which the decrease of dangling bonds or an increase of H content is dominant.

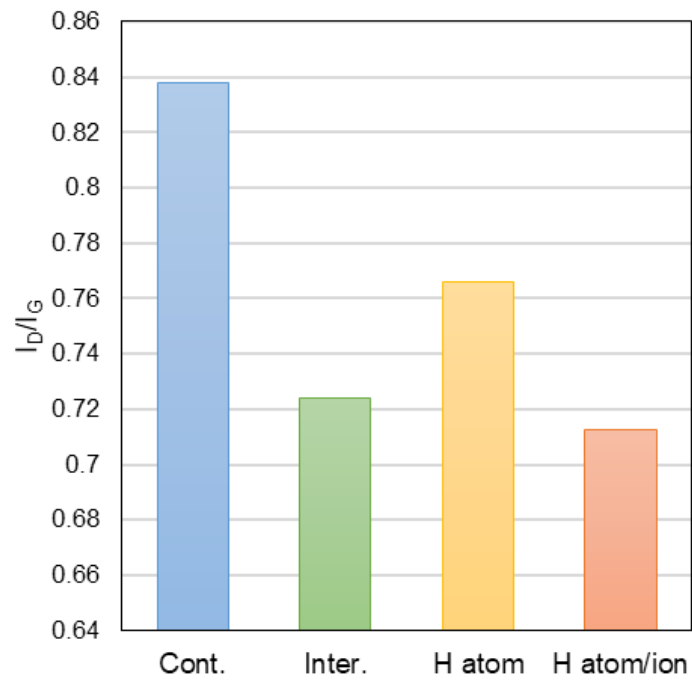


Figure 3.9  $I_D/I_G$  of as-deposited films.

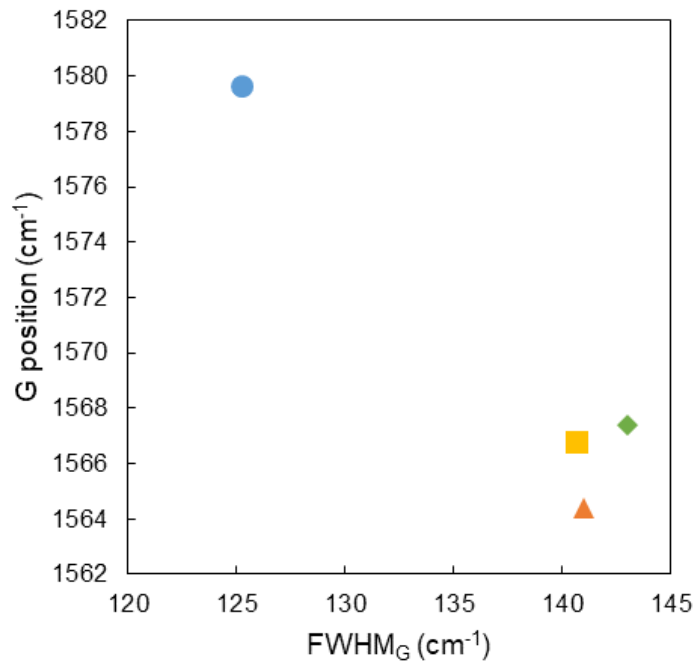


Figure 3.10 G position versus  $\text{FWHM}_G$ . (● Continuous, ◆ Interval, ■ H atom, and ▲ H atom/ion)

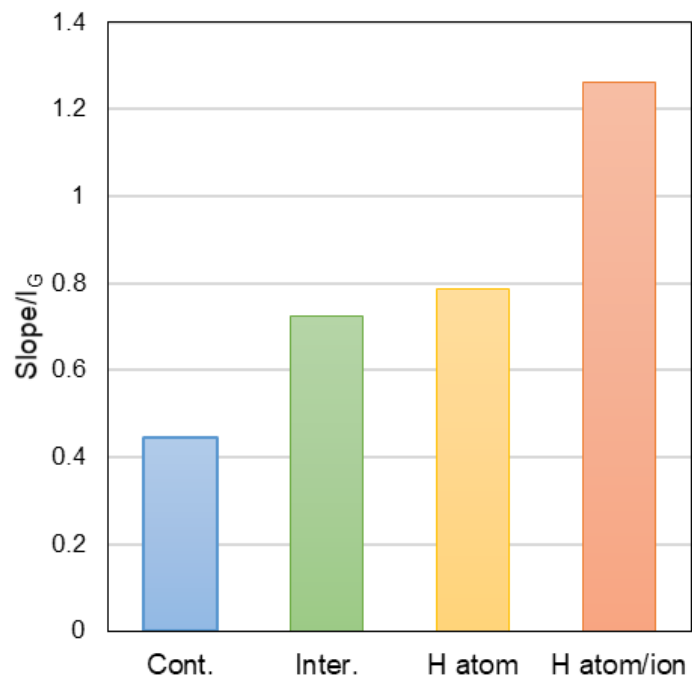


Figure 3.11 Slope/I<sub>G</sub> of as-deposited a-C films.

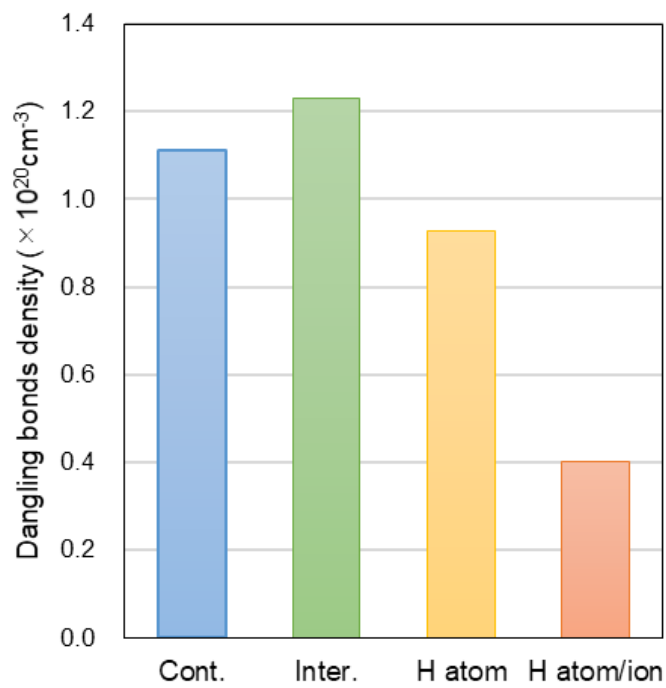


Figure 3.12 Dangling bonds density of as-deposited a-C films.

Figure 3.13 shows the optical bandgap of the as-deposited a-C films, calculated by a Tauc plot. The optical bandgap of the continuous, interval, and H atom irradiation cases are around 0.8 eV, on the other hand, that of H atom/ion irradiation case is 1.05 eV.

Judging from these results comprehensively, it is considered that dangling bonds are H-terminated by H atom/ion irradiation, and as a result, the H content is also increased. Moreover, only H atom irradiation case did not show such effect; the H ion tends to terminate the dangling bonds in the a-C film.

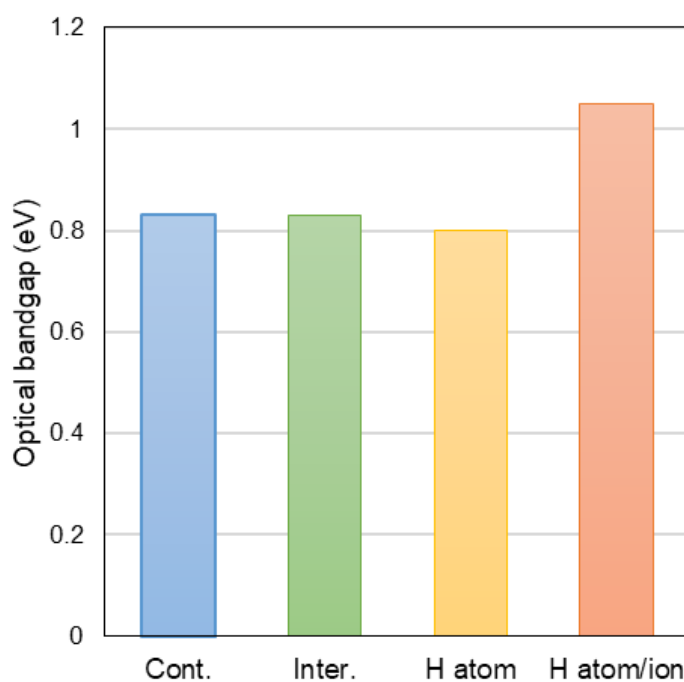


Figure 3.13 Optical bandgap (Tauc gap) of as-deposited a-C films.

### 3.3 Discussion: Effects of H atoms and H ions

From these results, the effect of hydrogen plasma on a-C films is considered as follows.

1. The hydrogen atom extracts hydrogen from the surface of the a-C film to form dangling bonds. It reacts only with the surface, and there is almost no etching effect of the a-C film. Because H abstraction always occurs at the surface, the polymer structure decreases and the carbon-carbon bond increases and the  $sp^2$ -C cluster size increases. When the effect of H atom irradiation only occurs on the film surface, it does not significantly affect the H content.

2. When H ions and light are added to H atoms, the H content of the entire film increases because the H ions reach the deep part of the film. As a result, H-terminated structure increased, and the dangling bonds decreased. These reactions are thought to be caused by relatively low energy hydrogen ions because the sample stage was not RF biased during H atom/ion irradiation. Also, the chemical sputtering by ion bombardment occurs. When the RF bias increases, the chemical etching effect might occur mainly. This result is different from the result that the Keudell et al. reported as explained in Section 1.3.3. It is no wonder that the H abstraction by collision cascade which they proposed occurs. However, our results cannot be simply explained in terms that the abstracted H recombines with H bonded with C to form  $H_2$ . The abstracted H might react with the nearby dangling bonds.

### 3.4 Conclusions

The effects of H atoms and ions on the film properties of a-C films were investigated by the sequential deposition process. The film thickness increased by the surface treatment of hydrogen atoms. In contrast, the film thickness decreased by simultaneously injecting H atoms, H ions, and light.

The influence of the sequential process on the bonding structure of the a-C film was discussed from the results of Raman spectroscopy. Surface H was eliminated by H atoms, and it promotes graphitization. The H content of the a-C film increased by adding H ions.

To support the Raman analysis, the changes of the optical bandgap, the density of dangling bonds were also investigated. Due to the influence of hydrogen atoms, both the optical band gap and the density of dangling bonds did not change. Also, when hydrogen atoms and hydrogen ions were implanted at the same time, the band gap increased, the dangling bonds density decreased. From this result, the effect of H atom and H ion irradiation were considered as, 1) H atoms abstract H only from the surface and generate the surface dangling bonds, 2) H ions etch the a-C films by the chemical sputtering, 3) H ions deeply project into the film and react with the dangling bonds, 4) H ions abstract H from the C-H by the collision cascade and the abstracted H reacts the dangling bonds again.

## Chapter 4 Control of CH<sub>3</sub> radical and its effects on the sp<sup>2</sup> fraction and hardness of a-C film

In the case of a-C growth by PECVD, it has been deduced that ion bombardments are critical to the formation of the sp<sup>3</sup>-C bonding structure, and this is called the subplantation model as mentioned in Section 1.3.1 [23]. On the other hand, since densities of radicals are generally much higher than those of ions in the PECVD system, the bonding structures should also strongly depend on the irradiation of radicals during the deposition process. The radicals are adsorbed at surface dangling bonds forming the carbon film [100]. CH<sub>3</sub> radicals are the main precursors during film deposition, in a single-frequency CCP, as reported by Mutsukura et al. [101]. The CH<sub>3</sub> radicals are long-lived species as compared with CH and CH<sub>2</sub>. The measurement of radicals in CH<sub>4</sub> plasmas was reported [102]. However, effects of radicals on the bonding structure and electronic properties have not been discussed yet.

Jia et al. have reported that the composition of radicals could be controlled by changing the residence time of source gases in the deposition chamber [62]. As the short residence time tuned the low electron-collision-induced impact frequency between gases and electrons in the plasma, the number of six-membered carbon rings decreased, the amorphization of the a-C films enhanced, and then the optical bandgap of the a-C films increased at the short residence time [62]. The optical emission spectral data of radical species such as C<sub>2</sub> and CH were also varied by decreasing the residence time [62]. From the relationship among the radical composition, deposition rate, and OES data, the radical density ratios were concluded to be main factors [62]. In the measurements of the near-edge X-ray absorption fine structure (NEXAFS),

the  $sp^2$  fraction of a-C films changed from 52% for the residence time of 18 ms to 46% for 6 ms and increased again to 70% for the shortest residence time of 2 ms [52]. A single mechanism failed to explain the experimental results on the  $sp^2$  fraction of the a-C films because the electronic structure of the a-C films could be modified by deposition conditions [52]. The structural properties were able to control by the optimization of radical species compositions and their densities [62]. However, the generations of radicals and their effects on the film properties have not been quantitatively considered yet.

The relationship between the radical density in the plasma, especially for nonradiative  $CH_3$  radicals, and the bonding structure of the a-C films was a focus of this study. To measure the radicals quantitatively, the author performed appearance mass spectrometry to analyze the neutral radical species generated in the  $CH_4/H_2$  mixture plasma. The author measured the  $CH_3$  radical density in the PECVD system by the QMS. The effects of the  $CH_3$  radicals on the  $sp^2$  fraction in the a-C films are discussed concerning the residence time of source gases and the generation of  $C_2H_4$  and  $C_2$  radicals.

## 4.1 Experimental details

In this experiment, to control the residence time, the flow rates of CH<sub>4</sub> and H<sub>2</sub> gas were varied as shown in Table 4.1. The residence time was calculated by Eq. (1-4). In this chapter, microwave power was applied for the deposition. The input powers were constant while the flow rates were varied.

Table 4.1 The deposition conditions.

	Values
Microwave power (W)	400
VHF power (W)	100
RF bias power (W)	50
Stage temperature (°C)	550
Pressure (Pa)	1
H <sub>2</sub> into SWP chamber (sccm)	13, 25, 50, 100, 133
H <sub>2</sub> into CCP chamber (sccm)	0
CH <sub>4</sub> (sccm)	26, 50, 100, 200, 266
Gap between parallel electrodes (mm)	30

## 4.2 Results and discussion

Figure 4.1(a) shows the mass spectra when the plasma was ON and OFF. The residence time was 2 ms. When the plasma was ON, obvious peaks appeared at mass numbers of 15 ( $\text{CH}_3$ ), 16 ( $\text{CH}_4$ ), 26 ( $\text{C}_2\text{H}_2$ ), 28 ( $\text{C}_2\text{H}_4$ ), 30 ( $\text{C}_2\text{H}_6$ ), 40 ( $\text{C}_3\text{H}_4$ ), 42 ( $\text{C}_3\text{H}_6$ ), 50 ( $\text{C}_4\text{H}_2$ ), 52 ( $\text{C}_4\text{H}_4$ ), 54 ( $\text{C}_4\text{H}_6$ ), and 56 ( $\text{C}_4\text{H}_8$ ), acquired with an electron energy of 15 eV for ionization. On the other hand, only a mass number of 16 ( $\text{CH}_4$ ) was detected when the plasma was OFF. Figure 4.1(b) shows the output intensity of quadrupole mass spectrometer of a mass number of 15 ( $\text{CH}_3$ ) at a residence time of 2 ms as a function of electron energy for ionization. The signals above 15 eV were attributed to the dissociation of  $\text{CH}_4$  in the QMS, but not to that of  $\text{CH}_3$  from the plasma in the process chamber. This is because  $\text{CH}_4$  dissociates into  $\text{CH}_3^+$  and H by one electron impact when the electron energy is higher than its threshold value of 14.3 eV [103]. The ionization threshold energy of  $\text{CH}_3$  is 9.8 eV. Therefore, the  $\text{CH}_3$  signals between 9.8 and 14.3 eV were attributed to the  $\text{CH}_3$  radicals effusing from the plasma. The author focused on the following two molecules:  $\text{CH}_3$ , which was the only radical detected in this experiment, and  $\text{C}_2\text{H}_4$ , which had the highest intensity in the mass spectra.

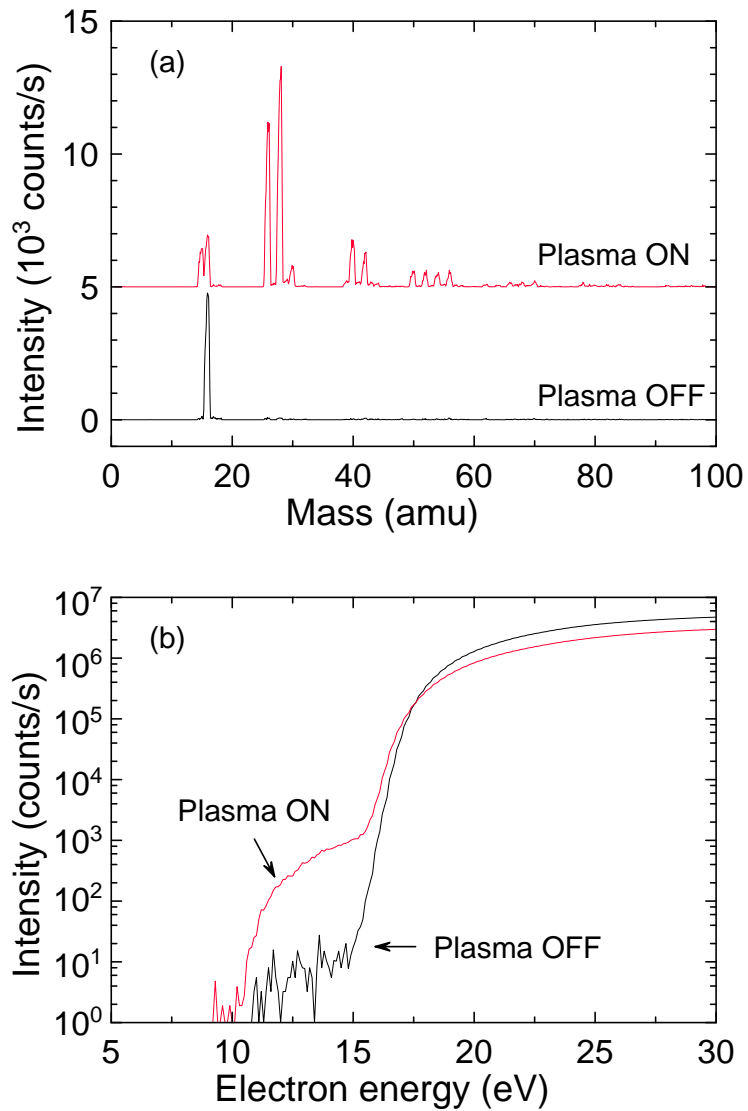
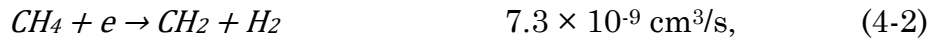


Figure 4.1 (a) Mass spectra of the plasma at a residence time of 2 ms with ionization energy of 15 eV (lower black line: plasma off, upper red line: plasma on). (b) Quadrupole mass spectrometer output of 15 amu at a residence time of 2 ms as a function of electron energy for ionization (black line: plasma off, red line: plasma on).

In Fig. 4.2, CH<sub>3</sub> radical densities are plotted on the left axis as a function of the residence time, and sp<sup>2</sup> fractions are also plotted on the right axis. With decreasing residence time from 18 to 6 ms, the CH<sub>3</sub> radical density increased from 9.6×10<sup>10</sup> to 1.6×10<sup>11</sup> cm<sup>-3</sup>. Then, it decreased as the residence time decreased to 2 ms. The CH<sub>3</sub> radical density should be determined from the results of both generation and recombination processes.

Electron impact dissociations of CH<sub>4</sub> occur via the following reactions: [101]



The highest rate constant is shown by reaction (4-1),  $CH_4 + e \rightarrow CH_3 + H$ ; such a rate constant is more than 6 times larger than those of the CH<sub>2</sub> and CH pathways. In the CH<sub>4</sub>/H<sub>2</sub> plasma, the electron impact dissociation of CH<sub>4</sub> mainly generates CH<sub>3</sub> radicals. The other reaction of CH<sub>4</sub> with H atoms is given as [101]



Because the rate constant of reaction (4-4) is smaller than those of the aforementioned electron impact dissociations, reaction (4-4) is negligible as a CH<sub>3</sub> generation pathway in this experiment. In the excitation dissociation of CH<sub>4</sub>, Harrevelt reported that the photodissociation of CH<sub>4</sub> by ultraviolet (UV) irradiation is given as [104]



where the excitation has threshold energy of approximately 5 eV (247 nm). By emissions of H atoms in the VUV region, called Lyman series, photoexcitation might occur in the CH<sub>4</sub>/H<sub>2</sub> plasma [105]. From the experimental results, a comparative number of CH<sub>2</sub> radicals was not detected

by appearance mass spectroscopy in our system. This can be interpreted as due to reaction (4-5) being negligible.

The  $sp^2$  fractions of the deposited a-C films are shown on the right axis in Fig. 4.2 as a function of residence time, as referenced in the previous study [52]. The minimum  $sp^2$  fraction appeared at 6 ms. It was found that the  $sp^2$  fraction depended on the  $CH_3$  radical density. The  $sp^2$ -C double bonds do not form directly from the  $sp^3$ -C single bonds of  $CH_3$  radicals. The chemisorption of  $CH_3$  radicals at surface dangling bonds forms a trihydride surface group in the first step [100]. The  $sp^2$ -C bonding structure was possibly formed by recombination with other molecules in the plasma, for examples,  $CH_3 + CH \rightarrow C_2H_4$ . From the results of the dependence of residence time on  $CH_3$  radical density and  $sp^2$  fraction, the formation of  $CH_3$  radicals should be considered as due to the electron impact dissociation of  $CH_4$ . As mentioned previously, the  $CH_3$  radical density should be determined from the results of both generation and recombination processes. First, the generation of  $CH_3$  radicals from the dissociation of  $CH_4$  is discussed.

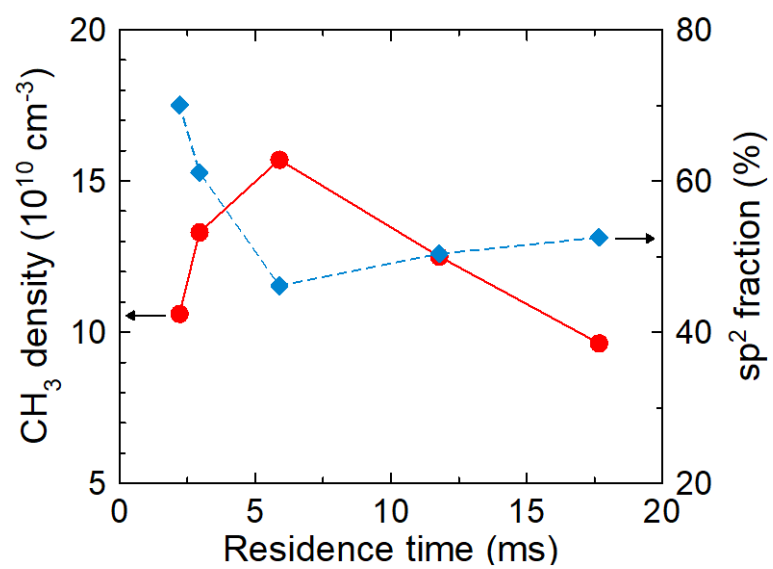


Figure 4.2 Residence time dependence of CH<sub>3</sub> density (circles). Changes in sp<sup>2</sup> fraction (diamonds) are also plotted.

Figure 4.3 shows the degree of  $\text{CH}_4$  dissociation as a function of the residence time. The degree of  $\text{CH}_4$  dissociation was estimated from the density ratio of  $\text{CH}_4$  when the plasma was ON and OFF. Such a degree increased from 0.4 to 0.7 as the residence time increased from 2 to 18 ms. The dissociation of  $\text{CH}_4$  occurred via reactions (4-1) to (4-4). With increasing the residence time, the electron impact and collision of feedstock  $\text{CH}_4$  gas with atomic H and photoexcitation increased. With the enhancement of the dissociation of feedstock  $\text{CH}_4$  gas with increasing the residence time from 2 to 6 ms, the  $\text{CH}_3$  radical density increased. However, this change contradicts the fact that the  $\text{CH}_3$  radical density decreased with increasing the residence time from 6 to 18 ms. This is possibly due to the recombination process in the plasma that resulted in the generation of molecules such as ethylene,  $\text{C}_2\text{H}_2$ , and  $\text{C}_2$  radical, and so forth.

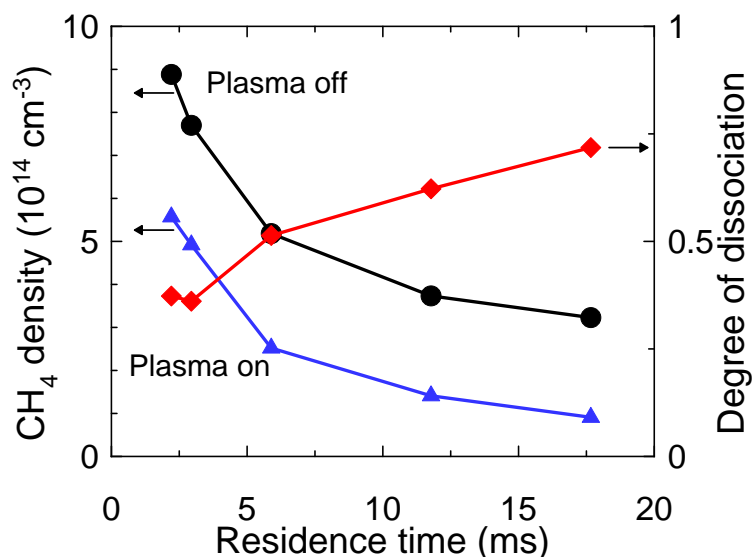


Figure 4.3  $\text{CH}_4$  density (circles and triangles) and its degree of dissociation (diamonds) as functions of residence time.

Figure 4.4 shows the  $C_2H_4$  density as a function of the residence time. The  $C_2H_4$  density increased with decreasing the residence time. As mentioned above, at a residence time less than 6 ms, the  $CH_3$  radical density decreased, while the  $C_2H_4$  density increased. This can be interpreted by the following oligomerization reactions:  $CH_3 + CH_3 \rightarrow C_2H_5 + H$ ,  $CH_3 + CH_2 \rightarrow C_2H_5$ ,  $C_2H_5 \rightarrow C_2H_4 + H$ , and  $CH_3 + CH \rightarrow C_2H_4$ . At a residence time more than 6 ms, both the  $CH_3$  and  $C_2H_4$  densities decreased with increasing residence time, while the relative  $C_2$  radical density decreased very slightly as shown on the right vertical axis in Fig. 4.4. The  $CH_4$  precursors were promoted to dissociate into fragments at a longer residence time. Then, highly dissociated precursors such as  $CH_3$ ,  $CH_2$ ,  $CH$ , and  $C$  recombined with each other, forming higher mass molecules,  $C_2H_4$ , and  $C_2$  in oligomerizations. Oligomers such as  $C_2H_4$ ,  $C_2$ , and higher mass molecules can be interpreted as the source to form  $sp^2$ -C in the a-C films. The bonding configurations such as  $sp^2$ -C and  $sp^3$ -C, in the a-C films, were formed through these generation and recombination processes in the plasma.

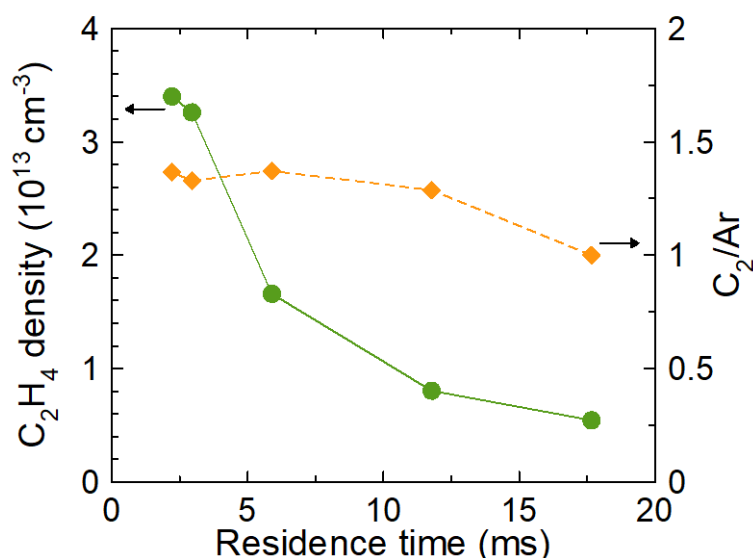


Figure 4.4 Dependence of  $C_2H_4$  density (circles) on residence time.  $C_2/Ar$  ratios (diamonds) normalized by that at a residence time of 18 ms are also plotted.

Figure 4.5 shows a reaction model in the  $\text{CH}_4/\text{H}_2$  plasma with varied residence time. As Jia et al. reported in previous paper, the deposition rate also increased with residence time and was maximum at a residence time of 6 ms [52]. However, the mechanism for the increase of the deposition rate was not clarified in previous study. It can be assumed that the deposition rate as a function of residence time was predominated by fluxes of the radical species. The measurement results in the current study revealed that the behavior of the deposition rate agreed well with the trend of the  $\text{CH}_3$  radical density for the residence time. Therefore, it can be supposed that the deposition rate depends on the termination of dangling bonds by the incident  $\text{CH}_3$  radicals. The dangling bonds at the surface were generated by ion bombardment during the deposition process, depending on the RF bias power applied to the substrate stage. In the case of PECVD, in which the densities of radicals are much higher than those of ions, the deposition rates were determined by the incident fluxes of the  $\text{CH}_3$  radicals when the incident flux of  $\text{CH}_3$  radicals is less than the number of dangling bond sites at the a-C surface. The recombination of the  $\text{CH}_3$  radicals into  $\text{C}_2\text{H}_4$ ,  $\text{C}_2$ , and higher mass molecules determined the  $\text{sp}^2\text{-C}$  formation, inducing the compositional transition at a residence time of 6 ms. Consequently, the control of the composition of radicals such as  $\text{CH}_3$ ,  $\text{C}_2\text{H}_4$ , and  $\text{C}_2$  is essential for controlling the optoelectronic properties of the a-C films prepared by PECVD.

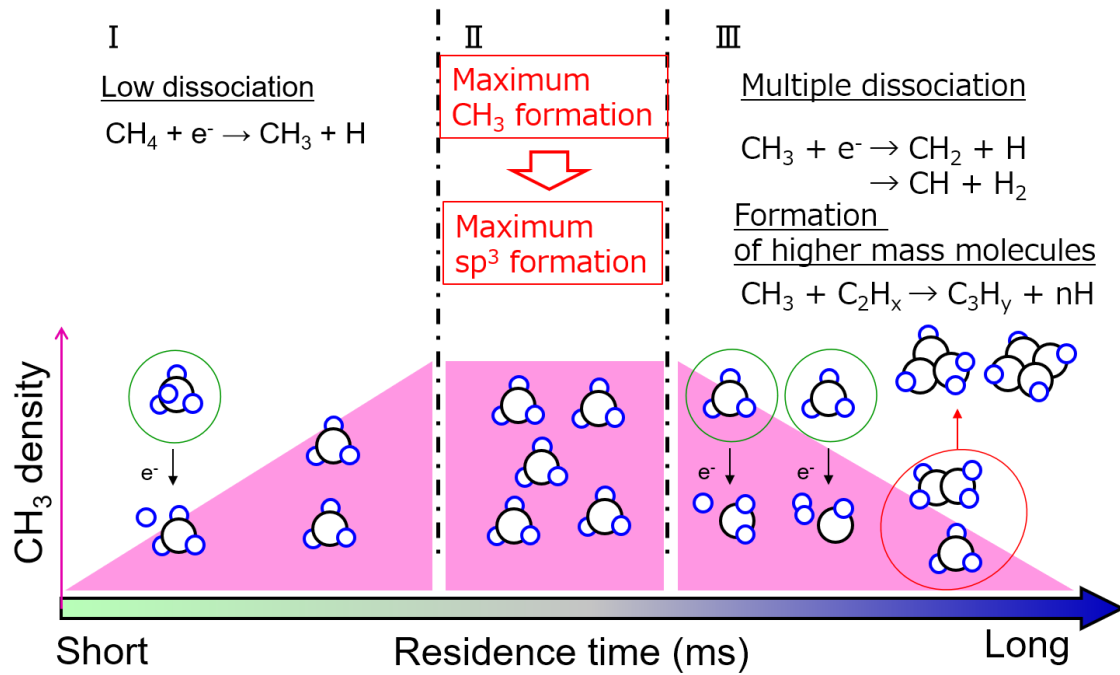


Figure 4.5 Reactions in H<sub>2</sub>/CH<sub>4</sub> plasma with various residence times.

The hardness of the a-C films is an important property of the coating applications. Figure 4.6 shows the hardness as a function of the CH<sub>3</sub> density. The hardness was measured by the nanoindenter. With increasing CH<sub>3</sub> density, the hardness of the a-C film increased. This result indicates that the hardness of a-C films depends on the density of CH<sub>3</sub> radicals because the CH<sub>3</sub> radical enhances the formation of sp<sup>3</sup>-C in the film.

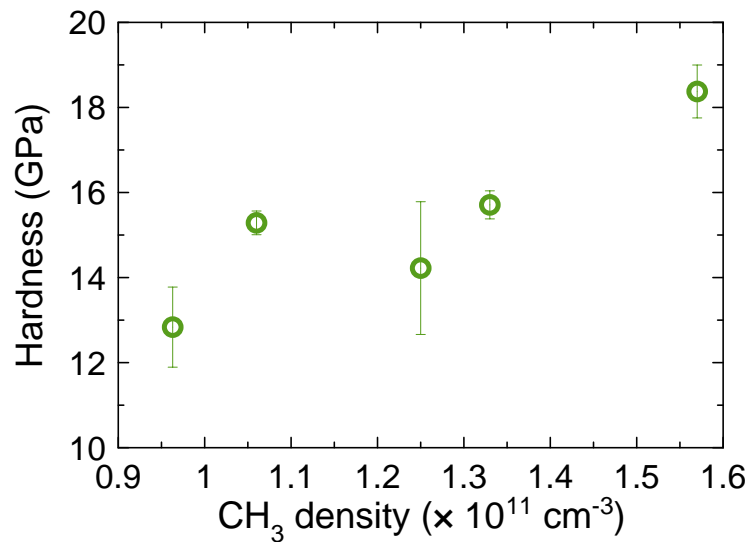


Figure 4.6 Hardness as a function of CH<sub>3</sub> density.

### 4.3 Conclusions

In the deposition of a-C films using a plasma of a mixture of CH<sub>4</sub>/H<sub>2</sub> gases in the RI-PECVD system, precursor species were studied by appearance mass spectrometry. Depending on the residence time of the gases in the reaction chamber, the sp<sup>2</sup> fraction of the a-C films reached the minimum of 46% at a residence time of 6 ms, where the CH<sub>3</sub> radical density was maximum. At a residence time above 6 ms, the degree of CH<sub>4</sub> dissociation increased and then the C<sub>2</sub>H<sub>4</sub> density decreased owing to the dissociation and recombination of the precursors, leading to the lowest sp<sup>2</sup> fraction of the a-C films. The hardness of a-C films depends on the density of CH<sub>3</sub> radicals because CH<sub>3</sub> radicals enhance the formation of sp<sup>3</sup>-C in the film. This knowledge is useful for understanding the formation mechanism and bonding structures of the a-C films.

## **Chapter 5 Control of $sp^2$ -C cluster incorporation of a-C films via monitoring of $C_2$ radical density**

In chapter 5, the author describes the  $C_2$  radical density in the plasma and the structural change of the a-C film. As mentioned in Chapter 4, moreover, the interaction of gaseous species with the deposition-surface plays a key role in controlling the bonding structure because the composition ratios of radical species are higher than those of ions in the plasma. Akasaka et al. reported that the  $sp^2$ -C cluster size in the a-C films increased with increasing electron density in the SWP of  $C_2H_2$  and Ar [106]. They found that the density of metastable Ar species increased with increasing electron density, enhancing the generation of carbon radicals via the collisions of the metastable Ar [106].

In this study, the author has extensively investigated the effects of plasma properties, especially electron, radical, and neutral species densities, on the bonding structures of a-C films. The author revealed the plasma excitation power has strong effects on six-membered ring structures in the a-C films. Based on systematic results with optical emission spectroscopy (OES) and quadrupole mass spectroscopy (QMS), the  $C_2$  radicals play important roles in the formation of six-membered ring structures. This control method is useful for the realization of various kinds of an atomic network of a-C films.

## 5.1 Experimental details

The deposition condition is shown in Table 5.1. The VHF power was varied from 20 to 250 W. The gas pressure of this experiment was 12 Pa.

Table 5.1 The deposition conditions.

	Values
Microwave power (W)	400
VHF power (W)	20, 50, 100, 200, 250
RF bias power (W)	30-150
Stage temperature (°C)	550
Pressure (Pa)	12
H <sub>2</sub> into SWP chamber (sccm)	250
H <sub>2</sub> into CCP chamber (sccm)	0
CH <sub>4</sub> (sccm)	500
Gap between electrodes (mm)	30

## 5.2 Results and discussion

### 5.2.1 Effect of the VHF power on the deposition

The effects of the VHF power on the behaviors of the deposition precursors of the a-C films were studied by controlling the electron impact dissociation of hydrocarbons under the presence of atomic H. In this section, the results of the plasma characterization and the structures of the as-deposited a-C films are discussed.

#### 5.2.1.1 Characterization of plasma

The electron density in the DF-CCP region with an injection of H atoms from SWP was measured using PAP, radical species were measured using the OES, and neutral species were measured using an appearance QMS.

Figure 5.1 shows the measured electron density as a function of the VHF power. The electron density increases almost linearly with increasing input power, which has been generally reported [107]. In the low VHF power range from 20 to 100 W, named a region (I), the electron density linearly increased from  $1.5 \times 10^{10}$  to  $5.6 \times 10^{10} \text{ cm}^{-3}$ . In the moderate VHF power range from 100 to 200 W, named a region (II), the electron density was constant at  $5.6 \times 10^{10} \text{ cm}^{-3}$ . In the high VHF power range more than 200 W, named a region (III), the plasma density increased linearly with increasing VHF powers. In the CCP operation, the electron heating is sustained by a mechanism of stochastic heating based on the motions of the sheath edge by application of the electric power to the parallel plate electrode [108]. At the low VHF power conditions, electron heating dominated the only the stochastic heating in front of the electrode used to apply the VHF power. At the high VHF power conditions, the discharge mode might be changed from a single-frequency CCP to a DF-

CCP mode, that is, the plasma was generated effectively by the stochastic heating at the sheaths facing both electrodes. The sheath motions are coupled to the powers at 100 and 13.56 MHz [108]. Further investigations are needed; however, it is possible to interpret the mode change in the discharges from the single frequency VHF power coupling to the dual frequency power coupling.

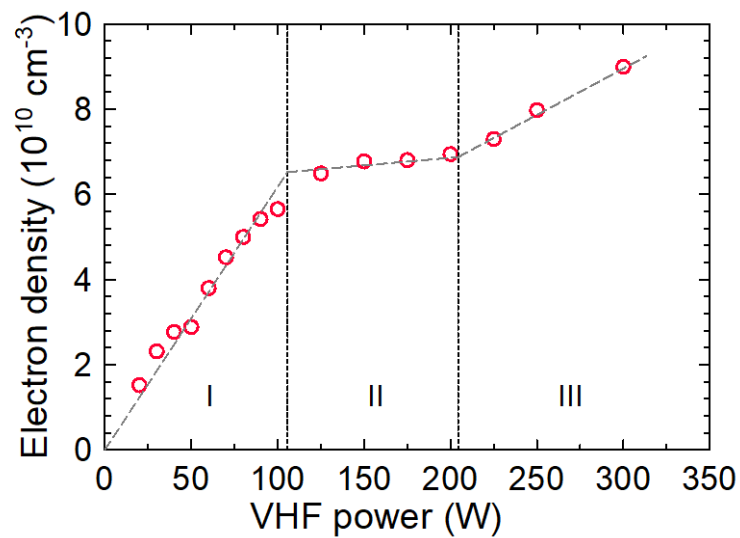


Figure 5.1 The electron density in the DF-CCP region as a function of VHF power. The dashed line is not a fit but a guide for the eye.

Optical emission spectra (OES) of the CH<sub>4</sub>/H<sub>2</sub> DF-CCP in the RI-PECVD system were measured. Figure 5.2(a) shows the OES when the VHF power was varied from 20 to 250 W. The integrated intensities of optical emissions over the whole visible range increased with increasing VHF power, which corresponds to an increase in electron density. The spectra of the plasma of CH<sub>4</sub> and H<sub>2</sub> were observed with a collection of lines. Emission lines are identified for CH at 431 nm ( $A^2\Delta; v' = 0 \rightarrow X^2\Pi; v'' = 0$ ), C<sub>2</sub> at 516 nm ( $A^3\Pi_g; v' = 0 \rightarrow X^3\Pi_u; v'' = 0$ ), H Balmer  $\alpha$  ( $H_\alpha$ ) at 656 nm, and  $H_\beta$  at 486 nm. The intensities of Ar emissions were fixed at wavelengths of 750 nm and 811 nm. For the actinometric analysis, a trace amount of Ar with a flow rate of 10 sccm was added into the CH<sub>4</sub> plasma. The change of the spectra by the Ar addition was negligibly small. By using an actinometric method, the normalization of the line intensities was performed by using the intensity of Ar peak at 811 nm after correcting the emission lines by subtracting a linear background. The intensities of the Ar line at 811 nm corresponded well with the electron density, as shown in Fig. 5.2(b). The Ar intensities should correspond to the product of the plasma density and an integrated value of multiplication of the excitation cross-section and electron temperature over the whole electron energy range. Since the Ar intensities were positively correlated with the electron density as the VHF power increased, the behavior of electrons with energies greater than 13.5 eV was unchanged in the present conditions.

Using the integrated line intensities (indicated by square blankets) for each species, the ratios of the intensities to the Ar intensity were calculated. The electron temperature was almost constant value of 2 eV (see Chapter 6) so that the intensity ratios can be directly compared. Figure 5.2(c) shows the normalized intensity ratios of [C<sub>2</sub>]/[Ar], [CH]/[Ar], and [ $H_\alpha$ ]/[Ar]. The normalization was performed at 20W in VHF power for each intensity ratios.

The normalized intensities for  $C_2$ , CH, and H changed when the electron density changed. With increasing electron density,  $[C_2]/[Ar]$  increased linearly. However,  $[CH]/[Ar]$  and  $[H_\alpha]/[Ar]$  saturated. The compositions of the radicals in the plasma changed with increasing electron density.

The OES data reflects the density of  $C_2$  in the excited state ( $A^3\Pi_g$ ). However, it can be assumed that  $C_2$  radicals in the lower excited state ( $X^3\Pi_u$ ) are also present in the plasma. John et al. measured the density of  $C_2$  in the lower excited state ( $X^3\Pi_u$ ) in an Ar/H<sub>2</sub>/CH<sub>4</sub> microwave plasma by cavity ring-down spectroscopy (CRDS) [109]. They reported that OES and CRDS data showed a linear relationship and thus the upper and lower excited states were in equilibrium. Therefore,  $[C_2]/[Ar]$  can represent the densities of  $C_2$  in the two excited states ( $A^3\Pi_g$  and  $X^3\Pi_u$ ) in the plasma.

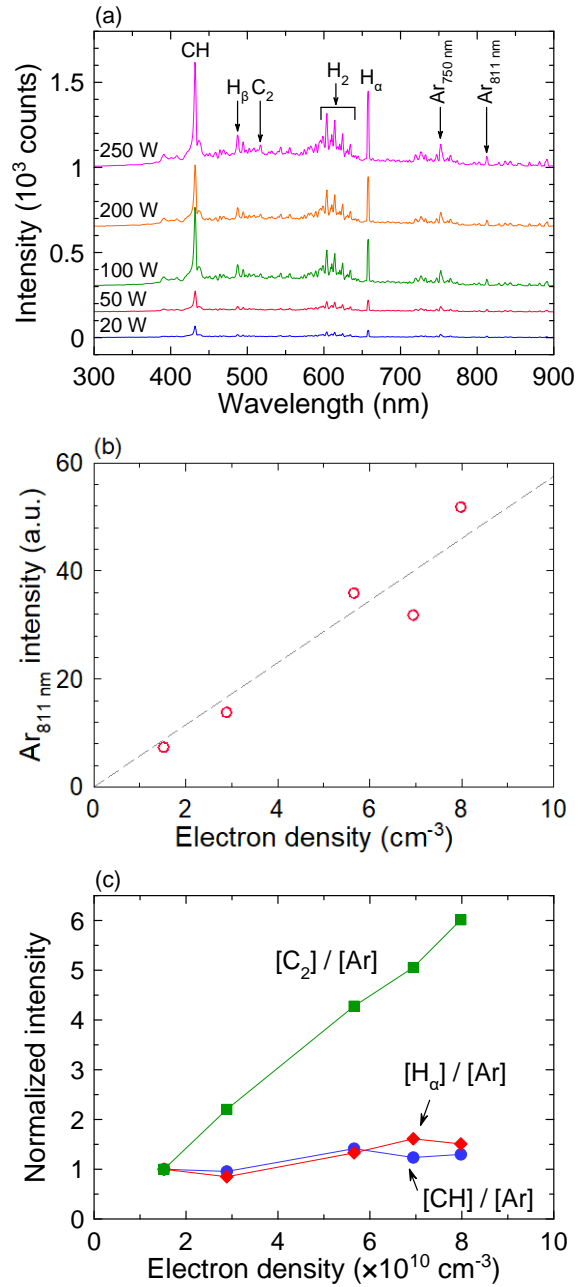


Figure 5.2 (a) Optical emission spectra of the  $\text{CH}_4/\text{H}_2$  DF-CCP for 20 to 250 W in VHF power, (b) the Ar intensity at 811 nm as a function of electron density (the dashed line is a linear fit result), (c) normalized  $[\text{C}_2]/[\text{Ar}]$  (square:  $\blacksquare$ ),  $[\text{CH}]/[\text{Ar}]$  (circle:  $\bullet$ ), and  $[\text{H}_\alpha]/[\text{Ar}]$  (diamond:  $\blacklozenge$ ) intensity ratios as functions of VHF power.

### 5.2.1.2 Behaviors of gaseous species in the plasma

Figure 5.3(a) shows a mass spectrum taken in residual gas analysis mode with an ionizing electron-energy of 13 eV. Neutral components in the CH<sub>4</sub>/H<sub>2</sub> DF-CCP with 250 W in VHF power were measured using the QMS method. For QMS measurements, Ar did not introduce the plasma to easily distinguish the hydrocarbon species. The signals at *m/z* values of 15, 16, 26, 28, 40, 42, 50, 52, and 54 and heavier masses were clearly detected when the plasma was ON. Only an *m/z* value of 16 was detected when the plasma was OFF. Thus, all signals were assigned to hydrocarbon species. Figure 5.3(b) shows the dependence of the electron density on the density of the dominant neutral species, CH<sub>3</sub>, C<sub>2</sub>H<sub>4</sub>, C<sub>3</sub>H<sub>*x*</sub> (*x*=4 and 6), and C<sub>4</sub>H<sub>*y*</sub> (*y*=2, 4, and 6). Since quantitative QMS measurements of the densities of all the neutral species were not adequately evaluated, the densities of C<sub>2</sub>H<sub>4</sub>, C<sub>3</sub>H<sub>*x*</sub>, and C<sub>4</sub>H<sub>*y*</sub> were qualitatively estimated by Eq. (2-7). The densities of C<sub>2</sub>H<sub>4</sub> linearly increased with increasing electron density. The density of the CH<sub>3</sub> radical, C<sub>3</sub>H<sub>*x*</sub> and C<sub>4</sub>H<sub>*y*</sub> saturated at an electron density of about  $3 \times 10^{10} \text{ cm}^{-3}$ .

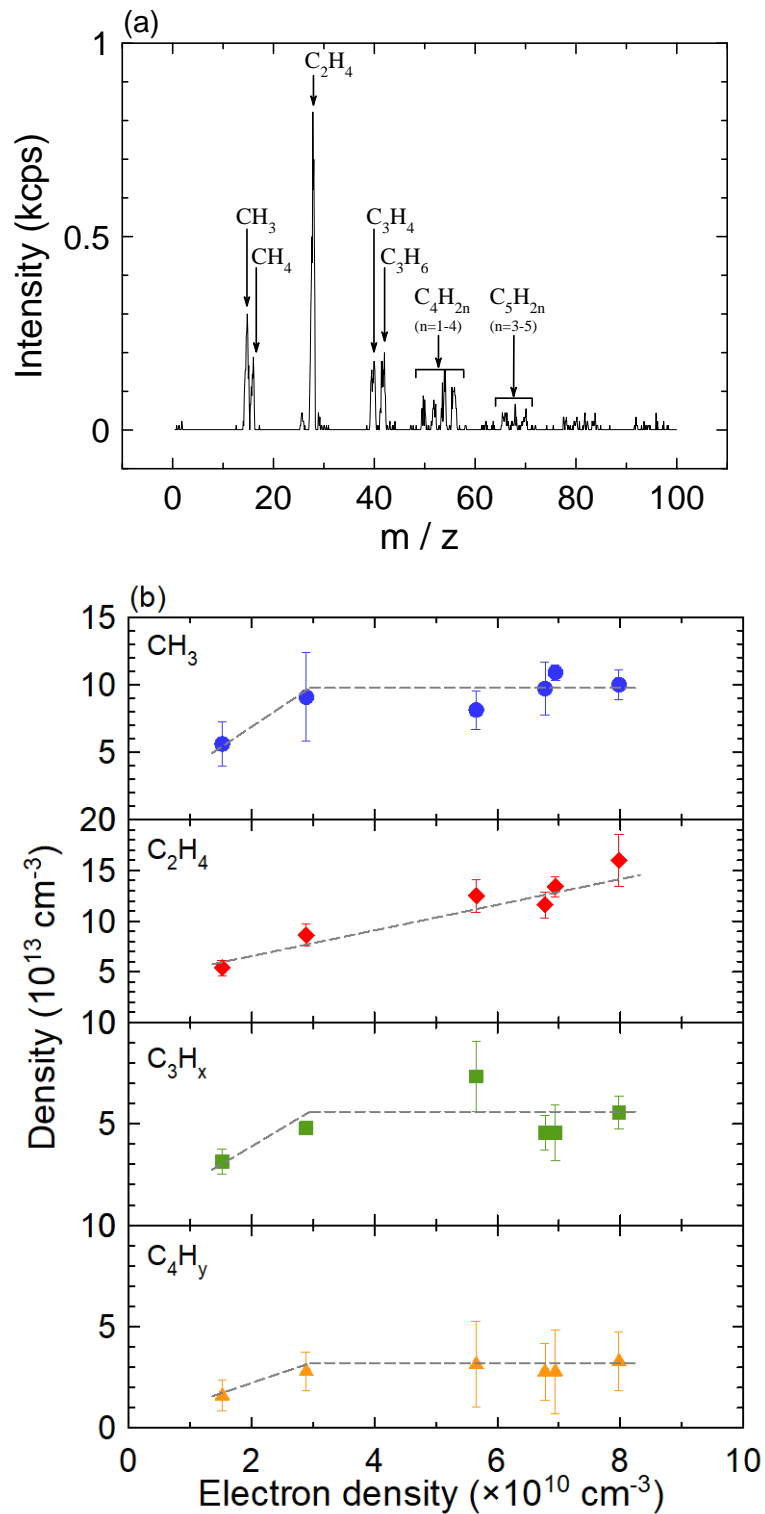


Figure 5.3 (a) Mass spectra of the DF-CCP at 250 W VHF power and (b) densities of neutral species in the DF-CCP as functions of electron densities. Dashed lines in Fig. 5(b) are simply guides for the eye.

### 5.2.1.3 Structural analysis of as-deposited a-C films

Figure 5.4 shows normalized Raman spectra of a-C films grown with the electron density ranging from  $1.5 \times 10^{10}$  to  $8.0 \times 10^{10} \text{ cm}^{-3}$ . The G band appears at around  $1580 \text{ cm}^{-1}$ . The G band consists of the three types of  $\text{sp}^2$ -C clusters, such as nc-G, nR, and nC, as mentioned before [78]. In addition to the G band, the D band appears at around  $1350 \text{ cm}^{-1}$ . This mode is forbidden in perfect graphite and only becomes active in the presence of disordered six-membered rings [77]. There are reports concerning the relationship between G position and a-C film structures [79]. For the visible Raman spectra, the higher shift of the G position shows the change from nR to the nc-G of  $\text{sp}^2$ -C clusters, but no relation with nC. The  $\text{FWHM}_G$  indicates the configuration of local disorder bonds, which can be related to the size of  $\text{sp}^2$ -C clusters and/or the  $\text{sp}^3$  content close to  $\text{sp}^2$ -C bonds. Therefore, the plot of G position versus the  $\text{FWHM}_G$  was proposed to estimate the a-C structure in literatures [79,81].

In the experimental results, the incorporation of  $\text{sp}^2$ -cluster of the deposited a-C films observed by the Raman positions and widths of the G band was controllable by monitoring of the  $\text{C}_2$  radical density.

The possibility of the a-C properties is shown in Fig. 5.5 which is a plot of G position versus the  $\text{FWHM}_G$ . The points are plotted with the literature' data for a-C films for comparison [79,81]. The author found that an increase in  $\text{C}_2$  radical density results in higher G position and narrower  $\text{FWHM}_G$ . The a-C in this region is often called as Graphite like carbon (GLC). Previously, a similar trend of the changes was reported in the case of an increase of post-annealing temperature. The relationship between  $\text{C}_2$  radical density and the  $\text{sp}^2$ -C cluster incorporation is possibly obtained the two reasons; (i) The  $\text{C}_2$  radical is generated in the plasma or from the wall of the chamber, then interacts with a-C films and enhances the nc-G structure because of the high

reactivity of  $C_2$  radical [110]. (ii) The  $C_2$  radical is sputtered from the deposited a-C film because of the high energy ion bombardment. Therefore, the  $C_2$  radical density reflects the structure of a-C film itself. Namely, the  $n_G$  of the  $sp^2$ -C cluster in the a-C films is controlled by adjusting the parameters concerning  $C_2$  radical density, enabling us to monitor *in situ* at real time during deposition.

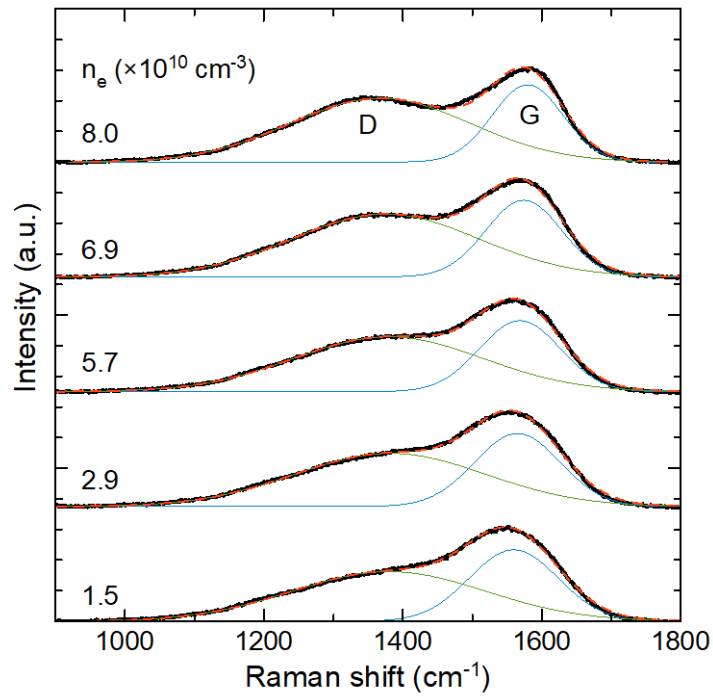


Figure 5.4 Raman spectra of a-C grown with various electron densities. The 2-peaks Gaussian fit results are also shown in each of the plots.

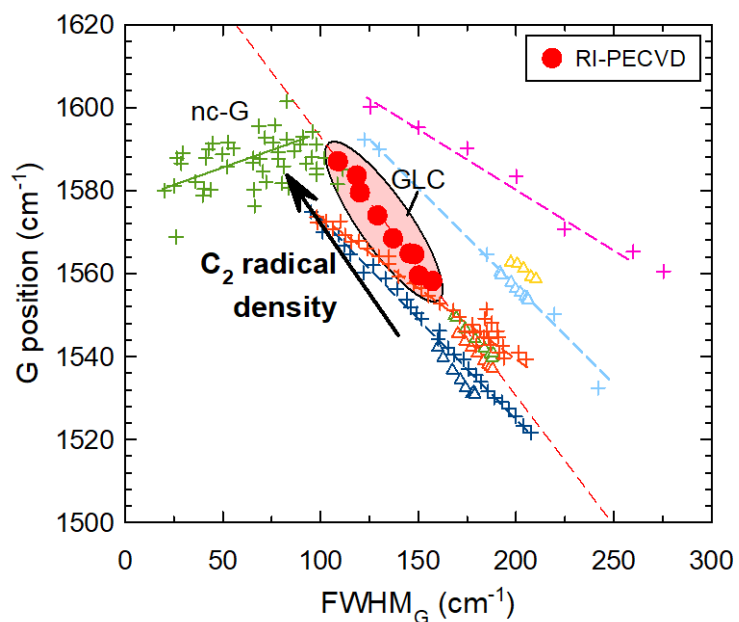


Figure 5.5 The Gaussian fit of 532nm Raman spectra of as-deposited a-C films. The plot of the variation of G position versus  $\text{FWHM}_G$  is shown with our RI-PECVD a-C films and various kinds of a-C films reported by Rose et al. and Merlen et al. for comparison [79,81]. ( $\Delta$  Rose et al., + Merlen et al., see details in Ref [81] and [79])

### 5.2.2 The possibility of the sp<sup>2</sup>-C cluster formation by C<sub>2</sub> radicals

The electronic states of C<sub>2</sub> consist of a singlet (<sup>1</sup>Σ<sub>g</sub>) and triplet (<sup>3</sup>Π<sub>u</sub>) [111]. A theoretical calculation indicates that two C atoms are bonded with a triple bond for the ground state singlet or with a double bond for the triplet [112]. The emission of C<sub>2</sub> at 519 nm originated from the triplet (<sup>3</sup>Π<sub>u</sub>) to triplet (<sup>3</sup>Π<sub>g</sub>) transitions. Skell et al. reported that the triplet C<sub>2</sub> species selectively reacted with C-H bonds as an H abstraction, and the singlet C<sub>2</sub> species produced acetylene from a singlet of vinylidene, acetone, and acetaldehyde [112]. Hence, the C<sub>2</sub> radical is highly reactive. An interpretation of our results is that a triplet C<sub>2</sub> abstracted atomic H from C-H bonds at the surface with the generation of a dangling bond, then two carbon atoms attached to the surface. Also, the singlet C<sub>2</sub> adsorbed in a nonselective manner on the surface and a C double bond group (C=C) formed on the surface. This might be the reason that the ordered six-membered ring structure was promoted with increasing numbers of C<sub>2</sub> radicals, leading to the formation of sp<sup>2</sup> double bonds at the surface.

In the case of graphene PECVD, Terasawa et al. reported that continuous growth of graphene occurred by adherence of a C<sub>2</sub> radical on the edge of graphene. However, a CH radical prevented the formation of a continuous sp<sup>2</sup> network [113]. Shiomi et al. and Hiramatsu et al. reported that the C<sub>2</sub> radical inhibited the growth of diamond with high crystallinity based on a measurement of the density of C<sub>2</sub> radicals in the plasma during diamond film formation [114,115]. Thus, the density of C<sub>2</sub> radicals effectively enhances the formation of the six-membered ring structures of a-C films.

While triplet C<sub>2</sub> radicals can be measured by OES and CRDS, singlet C<sub>2</sub> radicals cannot be measured. However, singlet C<sub>2</sub> might exist because it is in the ground state. Based on the reaction model reported by Skell et al., the

triplet  $C_2$  reacts with C-H bonds, and singlet  $C_2$  reacts at dangling bonds [112]. When triplet  $C_2$  reaches the film surface, it can form  $sp^2$ -C on the surface, regardless of the H termination of dangling bonds. Subsequently, two  $C_2$  radicals might form the six-membered ring structure at the  $sp^2$ -C edge. Therefore, a number of  $C_2$  radicals are quite important for controlling the  $sp^2$ -C clustering in the a-C films.

### 5.2.3 Structural control of a-C films via $C_2$ radical in the $H_2 / CH_4$ plasma

Under low VHF power (20-100 W) conditions, the dissociation of source gas linearly increased with increasing electron densities. Densities of all the species increased due to electron impact dissociation. Under high VHF power (100-250 W) conditions, the source gas of  $CH_4$  dissociated to form fragments, such as  $CH_3$ ,  $CH_2$ ,  $CH$ , and  $C$ . The density increase of fragments generated from the source gas resulted from the balance with the excessive dissociations, caused by multiple collisions with electrons. Only the densities of  $C_2$  and  $C_2H_4$  increased linearly with increasing electron density. These molecules were generated by multiple collisions of electrons.

Overall, our experimental results showed that the  $sp^2$ -C clusters in the as-deposited films of a-C were well-correlated with the behavior of  $C_2$ . Although the determination process of  $C_2$  density was discussed above, further investigations are required to elucidate the hypothesized mechanisms. The incorporation of  $sp^2$ -C clusters in a-C films can be controlled by changing the  $C_2$  radical density in regard with controlling of the plasma excitation powers.

### 5.3 Conclusions

Using radical-injection plasma-enhanced chemical vapor deposition,  $sp^2$  bonding structures organized in  $sp^2$ -C clusters of a-C films were controlled by changing the plasma excitation VHF power.  $sp^2$ -C clusters in a-C films were predominantly related to optical emissions of  $C_2$  radicals. The generation of  $C_2$  radicals increased with increasing electron density controlled by the input VHF power for the plasma excitation. This was determined from the densities of  $C_2$  radicals measured by OES and other species by appearance mass spectroscopy methods. The  $C_2$  radicals play important roles in enhancing the formation of  $sp^2$ -C clusters which is a portion of the  $sp^2$  fraction.

## Chapter 6 Effects of ion bombardment energy flux on chemical compositions and structures of a-C films

In the case of the PECVD, the ion bombardment energy ( $E_i$ ) can be controlled by the RF bias power, such as RF, direct current (DC), and pulsed DC applied to the sample stage. The RF bias voltage is useful for not only conductive but also insulative substrates because the negative DC self-bias voltage ( $-V_{DC}$ ) appears. The  $E_i$  is proportional to the magnitude of  $-V_{DC}$  ( $|-V_{DC}|$ ). Robertson et al. and Godet et al. reported that the H content and the optical bandgap decreased with increasing RF bias power [23,116]. However, the effect of ion flux ( $\Gamma_i$ ) has not been discussed so far. Of course, larger amounts of ions are expected to desorb more hydrogen and, develop densification and bond conversion. Oda et al. also reported the importance of the ratio between  $\Gamma_i$  and radical flux in film hardness control from the simulation results [117]. Therefore, the  $\Gamma_i$  should be considered as one of the essential factors as  $E_i$ .

In this study, the author investigated the effects of the ion bombardment energy flux ( $\Gamma_{E_i} = -V_{DC} \times \Gamma_i$ ) on the deposition rate, the incorporation of sp<sup>2</sup>-C clusters, the H content, and electronic properties of a-C films based on the plasma diagnostics results. To determine the  $\Gamma_{E_i}$ , the electron density, the H excitation temperature, and  $-V_{DC}$  were measured. The incorporation of sp<sup>2</sup>-C clusters, H contents, and electronic properties were discussed according to Raman spectra and electron spin resonance (ESR) measurements.

## 6.1 Experimental details

The ion flux ( $\Gamma_i$ ) was determined by the plasma density at the sheath edge ( $n_s$ ) and the Bohm speed ( $u_B$ ) [38].

$$\Gamma_i = n_s u_B = 0.61 N_e \left( \frac{e T_e}{M_i} \right)^{0.5}, \quad (6-1)$$

where  $e$  is the elementary charge,  $M_i$  is the mass of ion assumed 16 amu ( $\text{CH}_4$ ) in this experiment (shown in Fig. 6.1). The electron temperature ( $T_e$ ) was determined by the H excitation temperature instead of actual electron temperature because it is difficult to measure the electron temperature by a Langmuir probe method due to the deposition to the probe.

Thicknesses of a-C films were measured as a step height between the substrate and the film by a stylus line profiler. And then, the deposition rate was calculated as a value of a thickness divided by the deposition time of 20 min.

The deposition conditions are shown in Table 6.1.

Table 6.1 The deposition conditions.

	Values
Microwave power (W)	400
VHF power (W)	20-250
RF bias power (W)	30-150
Stage temperature (°C)	550
Pressure (Pa)	12
H <sub>2</sub> into SWP chamber (sccm)	250
H <sub>2</sub> into CCP chamber (sccm)	0
CH <sub>4</sub> (sccm)	500
Gap between electrodes (mm)	30

## 6.2 Results and discussion

### 6.2.1 Plasma characteristics

To determine the  $\Gamma_{E_i}$ , the ion species, the electron density and temperature, and the  $-V_{DC}$  were measured. Figure 6.1 shows the composition ratio of ion species in the H<sub>2</sub>/CH<sub>4</sub> DF-CCP measured by QMS. The CH<sub>4</sub><sup>+</sup> was 50-55% of the ions in the plasma, and CH<sub>3</sub><sup>+</sup> was 30-35%, H<sub>2</sub><sup>+</sup> was around 5%, and the rest 10% was H<sup>+</sup>, C<sub>2</sub>H<sub>2</sub><sup>+</sup>, and C<sub>2</sub>H<sub>4</sub><sup>+</sup>. Therefore,  $M_i$  is the mass of ion assumed 16 amu (CH<sub>4</sub>) in this experiment.

Figures 6.2 shows the plasma diagnostics results of H<sub>2</sub>/CH<sub>4</sub> DF-CCP. Figure 6.2(a) shows the electron densities at 20 and 250 W in VHF power, respectively, as a function of RF bias power. The electron densities hardly changed regardless of RF bias power. They were  $2.0-2.6 \times 10^{10}$  and  $8.8 \times 10^{10}$  cm<sup>-3</sup> for cm<sup>-3</sup> in the cases with 20 and 250 W in VHF power, respectively. RF bias voltage almost did not affect the electron density because the electron density increases in proportion to the square of the frequency of the discharge power [118]. The contribution of RF power to the electron density is negligibly small compared with VHF power. Figure 6.2(b) shows the H excitation temperature as a function of RF bias power, calculated by the Eq. (2-5). The H excitation temperature was almost constant to be about 2 eV regardless of both VHF and RF bias powers. The electron temperature usually depends on the process pressure because the acceleration of electrons depends on the mean free path. In the current study, the pressure was kept at 12 Pa. So that the electron temperature was almost not changed. The dissociation rate is highly sensitive to the electron temperature; then the electron density significantly increases although the change of electron temperature is within the measurement error. Figure 6.2(c) shows the dependence of the  $|-V_{DC}|$  on

the RF bias power. The  $|-V_{DC}|$  increased almost linearly with increasing the RF bias power. Figure 6.2(d) shows the  $\Gamma_i$  values calculated using Eq. (6-1) as a function of  $|-V_{DC}|$ . They hardly changed regardless of  $|-V_{DC}|$  to be  $4.0\text{-}5.4\times 10^{15}$  and  $1.8\times 10^{16}$   $\text{Vcm}^{-2}\text{s}^{-1}$  in the cases with 20 and 250 W in VHF powers, respectively. This means the  $\Gamma_i$  depends on the VHF power rather than the  $|-V_{DC}|$  because the  $\Gamma_i$  depends on the electron density via the VHF power, in contrast,  $|-V_{DC}|$  depends on the RF power. This suggested that the combination of VHF power and RF bias power can precisely control the plasma properties.

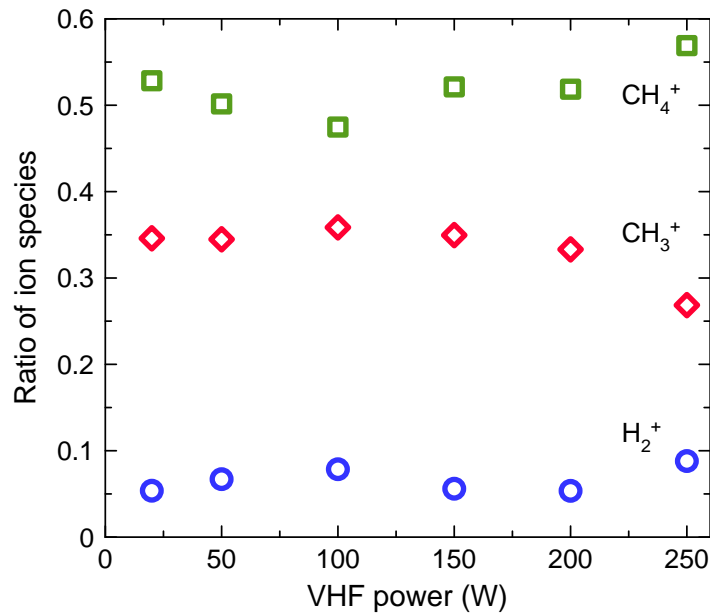


Figure 6.1 The composition ratio of ion species in  $\text{CH}_4/\text{H}_2$  DF-CCP.

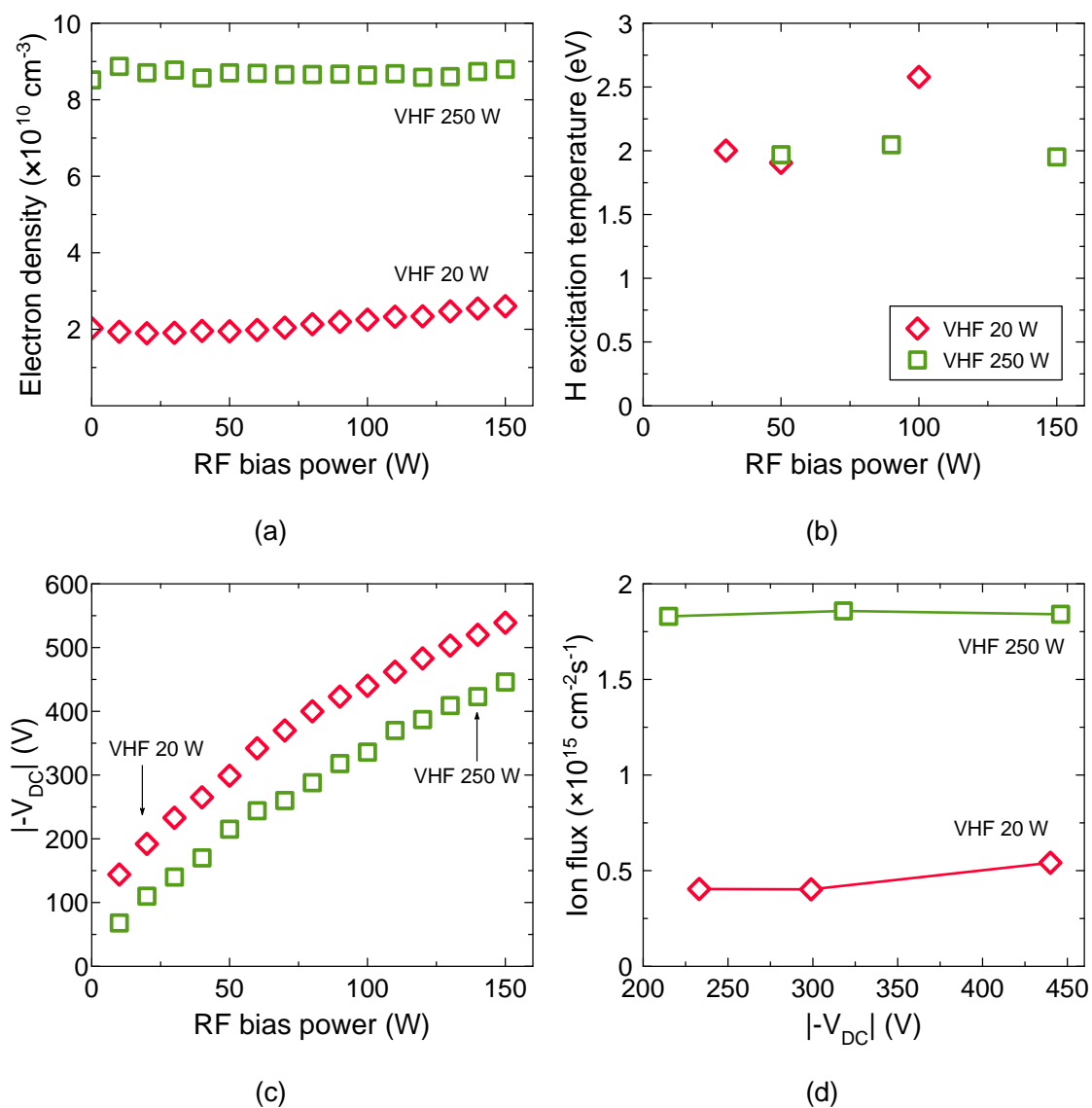


Figure 6.2 The results of plasma diagnostics. Diamonds ( $\diamond$ ) correspond to 20 W VHF power and squares ( $\square$ ) correspond to 250 W VHF power. (a) The electron density as a function of RF bias power; (b) H excitation temperature as a function of RF bias power; (c) The magnitude of negative self-bias voltage  $| -V_{DC} |$  as a function of RF bias power; (d) The ion flux as a function of the magnitude of negative self-bias voltage  $| -V_{DC} |$ .

Figure 6.3 shows the  $\Gamma_{E_i}$  values calculated from  $|-V_{DC}| \times I_i$  at 20 and 250 W in the VHF power, respectively, as a function of the RF bias power.  $\Gamma_{E_i}$  increased from  $0.9 \times 10^{18}$  to  $2.4 \times 10^{18}$   $\text{Vcm}^{-2}\text{s}^{-1}$  and from  $3.9 \times 10^{18}$  to  $8.2 \times 10^{18}$   $\text{Vcm}^{-2}\text{s}^{-1}$  for 20 and 250 W in VHF power, respectively. This suggested that the combination of VHF power and RF bias power can precisely control the plasma properties. Based on plasma characteristics, effects of  $\Gamma_{E_i}$  on the deposition rate, the incorporation of  $\text{sp}^2\text{-C}$  clusters, the H content, and the density of dangling bonds are discussed in Section 6.2.2-6.2.5.

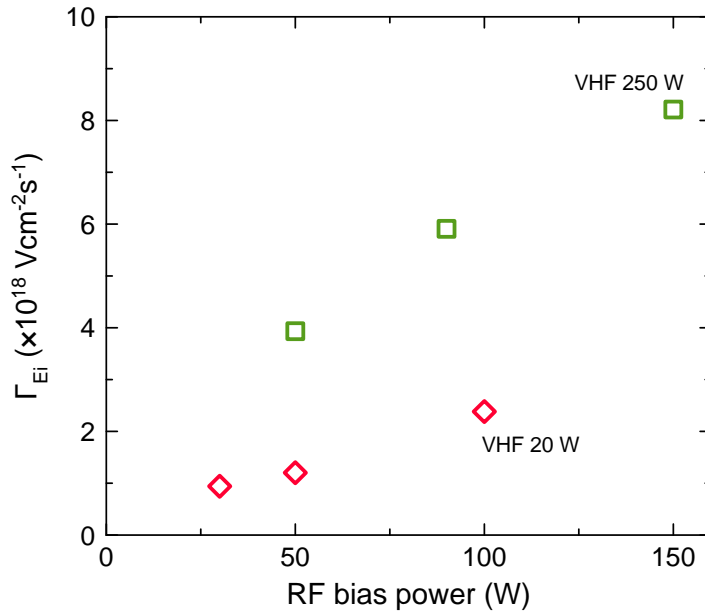


Figure 6.3 Ion bombardment energy fluxes  $\Gamma_{E_i}$  as a function of RF bias powers. Diamonds ( $\diamond$ ) and squares ( $\square$ ) correspond to 20 and 250 W in VHF power, respectively.

### 6.2.2 Effects of ion bombardment energy flux on the deposition rate

Figure 6.4(a) shows the deposition rate of a-C films as a function of  $|-V_{DC}|$ . In both cases with 20 and 250 W in VHF power, they almost proportionally decreased with increasing  $|-V_{DC}|$  in the same manner. However, values of Slope/ $I_G$  in VHF 20 W are higher than that in VHF 250 W. By plotting the deposition rate as a function of  $\Gamma_{E_i}$ , plots are almost on one line as shown in Fig. 6.4(b). It is assumed that the surface dangling bonds are generated by ion bombardment depending on not only its energy but also its flux, and then the sticking of radicals are enhanced. This result indicates that the deposition rate depends on  $\Gamma_{E_i}$  and  $\Gamma_{E_i}$  should be a candidate for the factor of the deposition mechanism of a-C in PECVD.

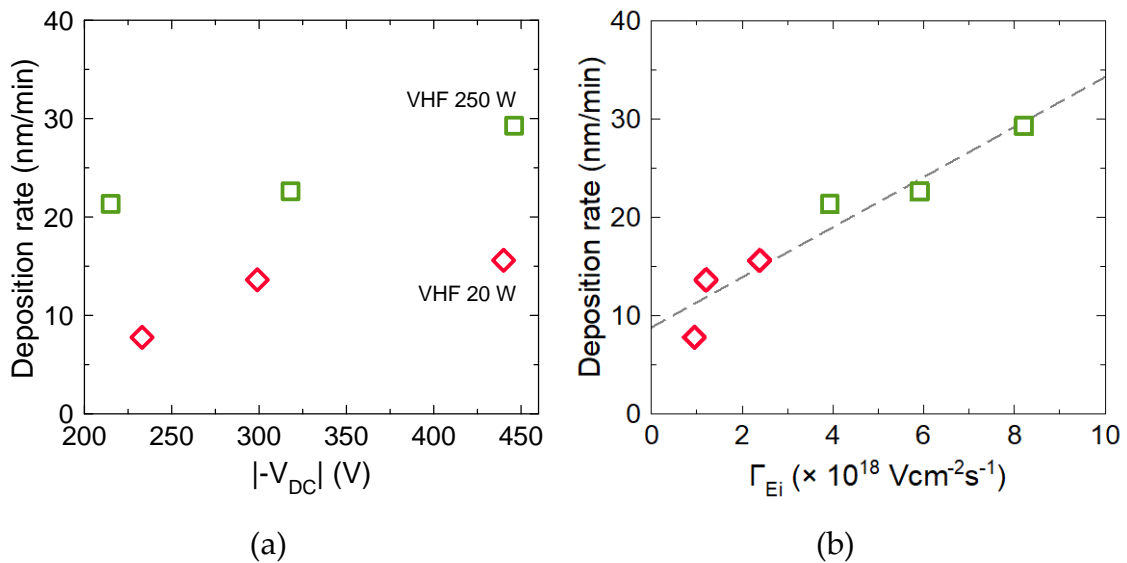


Figure 6.4 Deposition rate as a function of (a) magnitudes of negative self-bias voltages ( $|-V_{DC}|$ ) and (b) ion bombardment energy fluxes. Diamonds ( $\diamond$ ) and squares ( $\square$ ) correspond to 20 and 250 W in VHF power, respectively.

### 6.2.3 Effects of ion bombardment energy flux on Slope/ $I_G$ and density of dangling bonds

Figure 6.5 shows the Raman spectra of as-deposited a-C films deposited at different VHF and RF bias powers. G- and D- band peaks, which correspond to the  $sp^2$  bonded carbon and the edge of the six-membered ring structure respectively, became sharper as the RF bias power increased. Also, their widths at 20 W were larger than those at 250 W. This can be interpreted that thermal spike and relaxation occur with increasing VHF and RF bias powers. On the other hand, the PL background was decreased with increasing VHF and RF bias power. Also, the PL backgrounds at 20 W was larger than those at 250 W. As mentioned in Section 2.3.2, the H containing a-C films, usually deposited by the PECVD, shows the high intensity of the background signal because the recombination of excited electrons depends on the H content. Therefore, this PL background is often used to estimate the H content [80–84]. However, it should be noted that the dangling bonds density in the a-C film can also increase the PL background as Rose et al. reported [81]. The intensity ratio of the PL background to G-band peak (Slope/ $I_G$ ), increased with increasing post-annealing temperature, because of the passivation of the dangling bonds [81]. According to the molecular dynamic (MD) simulation, an increase of the number of C=C double bonds without changing the number of H atoms and C-H bonds suggested that the dangling bonds vanish as results of  $sp^2$  clustering and C reorganization. Conversely, this result also suggested that, if the density of dangling bonds hardly changed or decreased depending on any process conditions, an increase in the Slope/ $I_G$  indicates an increase of the H content. Figure 6.6(a) shows the Slope/ $I_G$  values as a function of  $|-V_{DC}|$ . As shown in the figure, in both the cases with 20 and 250 W in VHF power, they almost proportionally decreased with increasing  $|-V_{DC}|$  in the same

manner. However, values of Slope/ $I_G$  in VHF 20 W are higher than that in VHF 250 W. Figure 6.6(b) shows the Slope/ $I_G$  values as a function of  $\Gamma_{E_i}$ . They almost proportionally decreased with increasing  $\Gamma_{E_i}$  in the one line. These results suggested that the Slope/ $I_G$  values depend on not only the  $E_i$  but also the  $\Gamma_{E_i}$ .

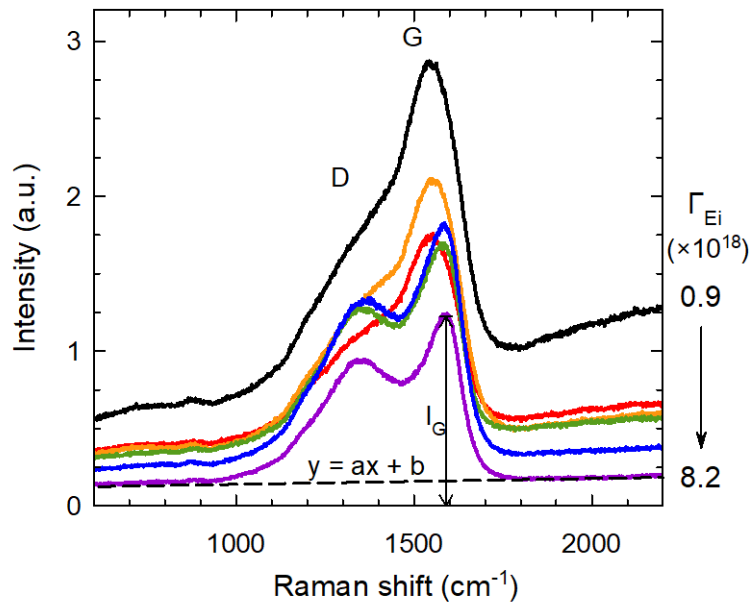


Figure 6.5 The Raman spectra of as-deposited a-C films. Top 3 spectra are a-C films deposited at 20 W in VHF power (black, orange, and red lines) and bottom 3 spectra are a-C films deposited at 250 W in VHF power (green, blue, and purple lines). The ion bombardment energy flux  $\Gamma_{E_i}$  are shown at the right and its value increase from top to bottom.

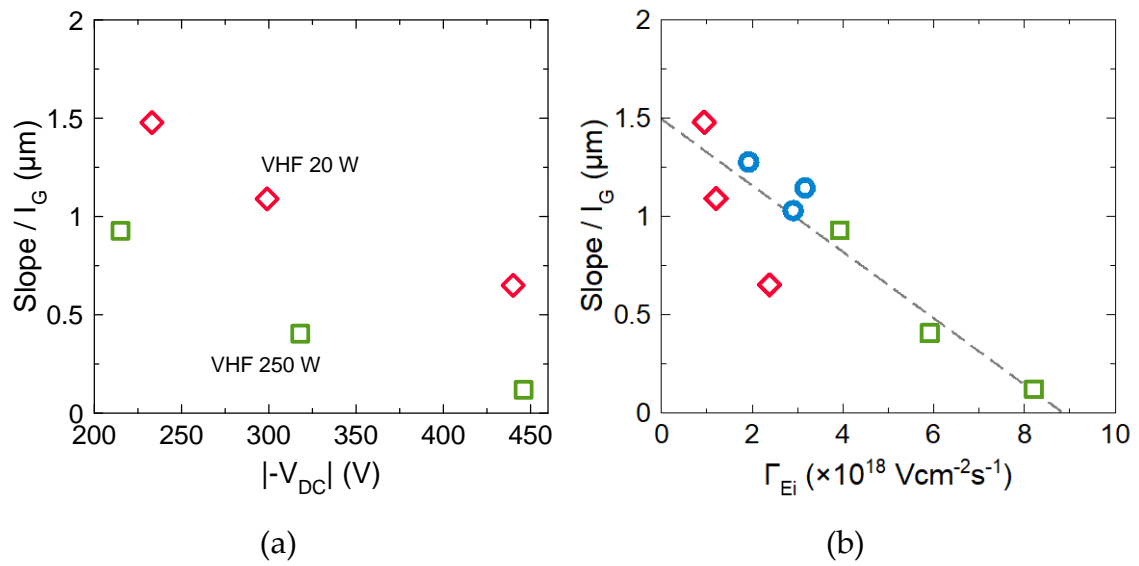


Figure 6.6 The Slope/ $I_G$  as functions of (a) the magnitude of the negative self-bias voltage  $|V_{DC}|$  and (b) the ion bombardment energy flux  $\Gamma_{Ei}$ . Diamonds ( $\diamond$ ) correspond to 20 W in VHF power, squares ( $\square$ ) correspond to 250 W in VHF power, and circles ( $\circ$ ) correspond to 50, 100, and 200 W in VHF power with 50 W in RF bias power.

Figure 6.5 shows the density of dangling bonds of the a-C films. With increasing  $\Gamma_{E_i}$ , the density of dangling bonds decreased in the same manner in both the cases with 20 and 250 W in VHF powers as well as the Slope/ $I_G$  values. This result indicated that the ion bombardment energy flux effectively reduced the dangling bonds of a-C films.

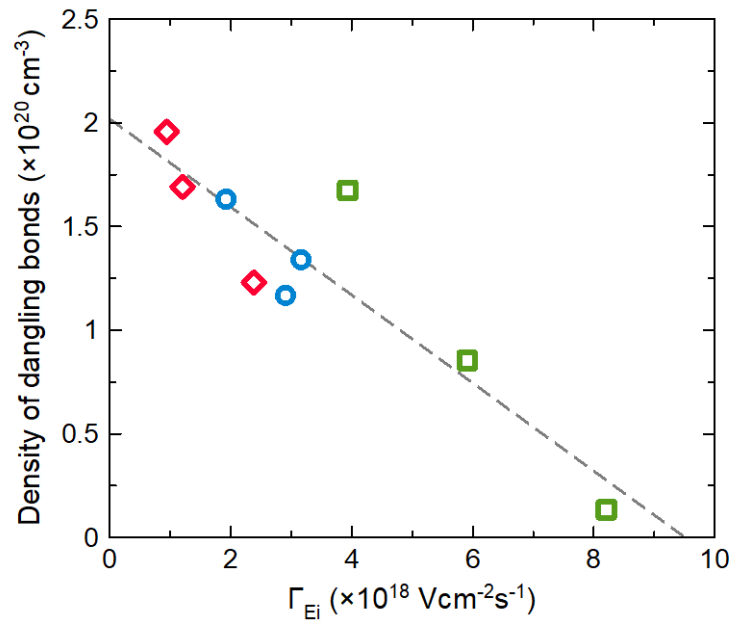


Figure 6.7 The dangling bonds density as a function of the ion bombardment flux. Diamonds ( $\diamond$ ) correspond to 20 W in VHF power, squares ( $\square$ ) correspond to 250 W in VHF power, and circles ( $\circ$ ) correspond to 50-200 W in VHF power with 50 W in RF bias power.

### 6.2.4 Effects of ion bombardment energy flux on sp<sup>2</sup>-C clusters

In chapter 6, the author reported the relationship between the optical emission of C<sub>2</sub> radical and the incorporation of sp<sup>2</sup>-C clusters. The possibility of the incorporation of sp<sup>2</sup>-C clusters by the C<sub>2</sub> radical itself, however, the more consideration was needed. In this section, the ion bombardment energy was introduced to explain the incorporation of sp<sup>2</sup>-C clusters and the change of the C<sub>2</sub> radical in the plasma.

Figure 6.8 shows the results of peak deconvolutions of Raman spectra of a-C films. Figure 6.8(a) shows the  $|-V_{DC}|$  dependence of G band position (G position), FWHM of G band (FWHM<sub>G</sub>), and the intensity ratio of D band to G band (I<sub>D</sub>/I<sub>G</sub>). With increasing  $|-V_{DC}|$ , the G position and I<sub>D</sub>/I<sub>G</sub> slightly increased, and the FWHM<sub>G</sub> slightly decreased. This trend implies that the ion bombardment enhances the incorporation of sp<sup>2</sup>-C clusters by thermal spike and relaxation process. However, the difference between 20 and 250 W in VHF power is larger than the changes of these values by  $|-V_{DC}|$ . Considering  $\Gamma_{E_i}$ , the G position, the I<sub>D</sub>/I<sub>G</sub>, and the FWHM<sub>G</sub> can be described as one trend. Figure 6.8(b) shows the G position, the I<sub>D</sub>/I<sub>G</sub>, and the FWHM<sub>G</sub> as functions of  $\Gamma_{E_i}$ . With increasing  $\Gamma_{E_i}$  from  $0.9 \times 10^{18}$  up to  $4.0 \times 10^{18}$  Vcm<sup>-2</sup>s<sup>-1</sup>, these 3 values linearly changed. Then, from  $4.0 \times 10^{18}$  Vcm<sup>-2</sup>s<sup>-1</sup>, the slope of changes decreased. Merlen et al. and Rose et al. reported that the plot of G position versus FWHM<sub>G</sub> for visible Raman spectra of a-C [79,81]. They showed that the increase in G position and decrease in FWHM<sub>G</sub> indicates the incorporation of sp<sup>2</sup>-C clusters and the change of structures to nanocrystalline graphite (nc-G). Therefore, the change of G position and FWHM<sub>G</sub> in the current study can be interpreted that the a-C films become nc-G by the ion bombardment energy flux. The increase in I<sub>D</sub>/I<sub>G</sub> indicates that the increase in

the crystallite size of  $sp^2$ -C clusters [77]. So that, the ion bombardment energy flux enhanced the incorporation of  $sp^2$ -C clusters.

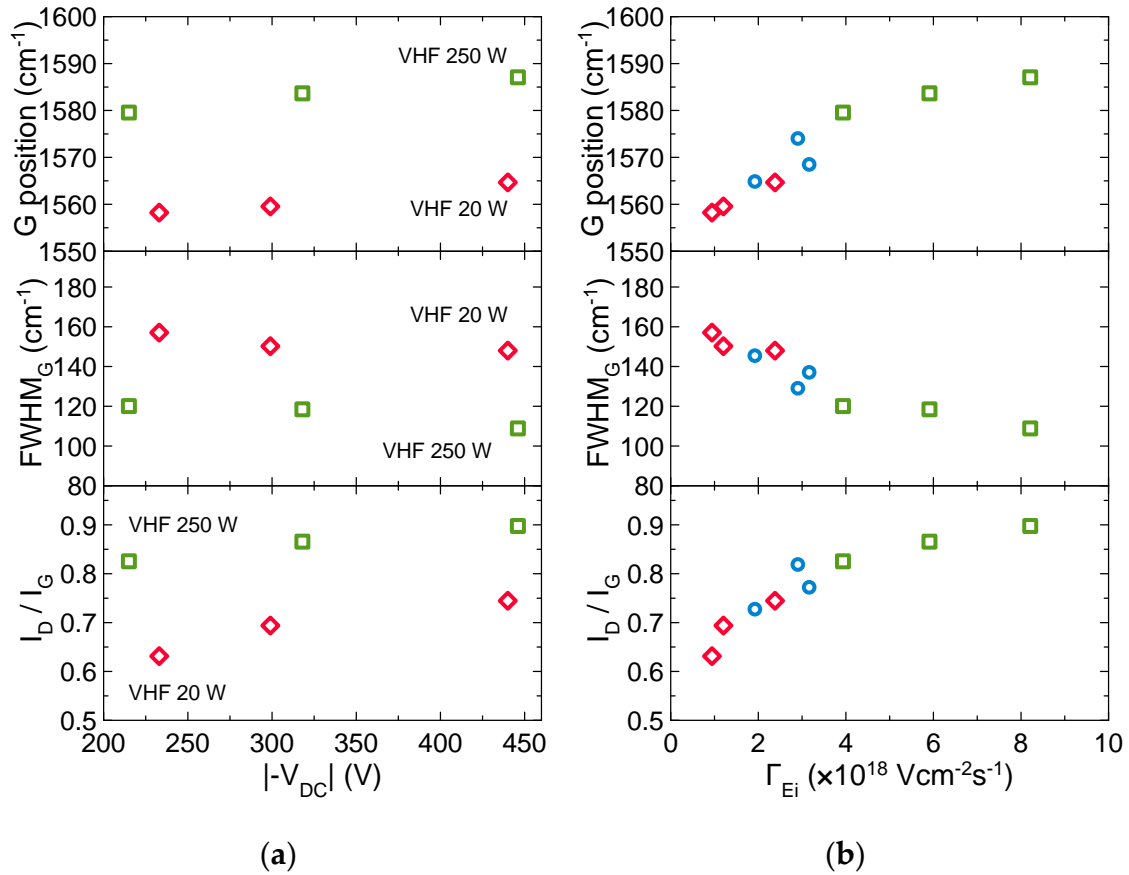


Figure 6.8 (a) The magnitude of the negative self-bias voltage  $| -V_{DC} |$  and (b) the ion bombardment energy flux  $\Gamma_{E_i}$  dependences of G band position (G position), FWHM of G band (FWHM $_G$ ), and intensity ratio of D band to G band ( $I_D/I_G$ ). Diamonds ( $\diamond$ ) correspond to 20 W in VHF power, squares ( $\square$ ) correspond to 250 W in VHF power, and circles ( $\circ$ ) correspond to 50, 100, and 200 W in VHF power with 50 W in RF bias power.

Figure 6.9 shows the dependences of  $[C_2]/[Ar]$ , G position, and  $FWHM_G$  on the  $\Gamma_{E_i}$ . Until  $4 \times 10^{18} \text{ Vcm}^{-2}\text{s}^{-1}$  of  $\Gamma_{E_i}$ ,  $[C_2]/[Ar]$ , G position increased and  $FWHM_G$  decreased linearly. Then, the slope of those turned to small and saturated. This change of G position and  $FWHM_G$  can be interpreted from Fig. 5.5. With increasing  $\Gamma_{E_i}$ , the  $sp^2$ -C clusters changed to nR or nC to nc-G. Then, at the certain  $\Gamma_{E_i}$ , the  $sp^2$ -C clusters in the a-C became almost nc-G. It is assumed that the nc-G cannot graphitize anymore by ion bombardment because the ion bombardment also destructs the crystalline structure. Therefore, the incorporation of  $sp^2$ -C clusters in the a-C films by  $\Gamma_{E_i}$  was saturated.

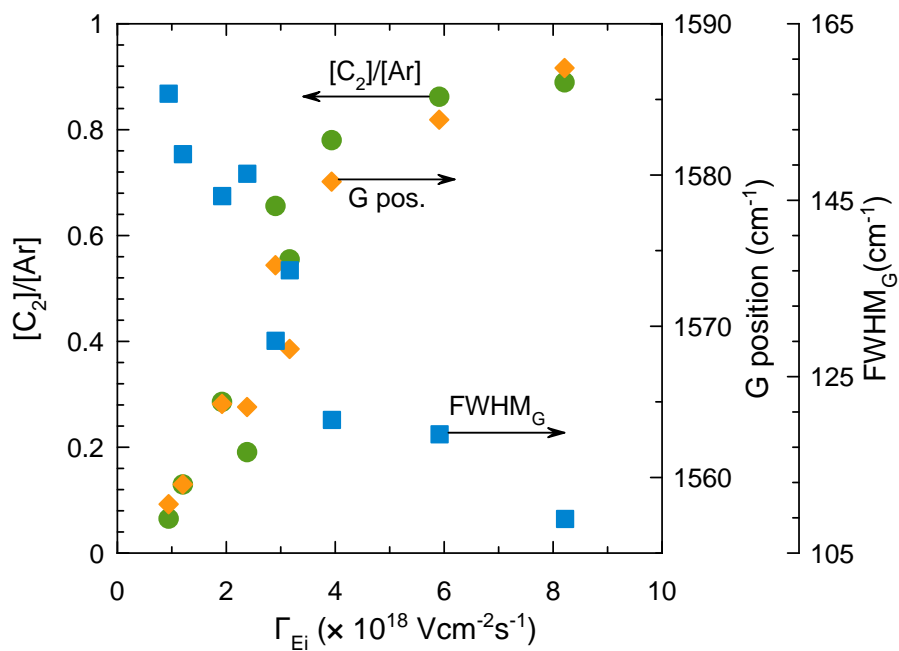


Figure 6.9 Dependence of  $[\text{C}_2]/[\text{Ar}]$ , G position, and  $\text{FWHM}_G$  on the  $\Gamma_{Ei}$ . Circles (●) corresponding to  $[\text{C}_2]/[\text{Ar}]$ , diamonds (◆) corresponding to G position, square (■) corresponding to  $\text{FWHM}_G$ .

Figure 6.10 shows Carbon K-edge NEXAFS spectra of a-C films and HOPG with an X-ray incident angle of  $54.7^\circ$ . All spectra of a-C films exhibit an absorption peak of C 1s to  $\pi^*$  transition (C=C) at  $285 \pm 0.1\text{eV}$  [93]. Since as grown a-C films contains hydrogen, a shoulder at around 287.0 eV was observed and assigned to the C 1s to  $\sigma^*$  transition of C-H [93]. The C-O  $\sigma^*$  antibonding orbital and the peaks of carbonyl groups could be observed at 288.5-289.0 eV and 286.7-288.5 eV because of contamination due to the sample exposure to air before the NEXAFS measurement [93,119]. A broad peak between 288 and 315 eV is assigned to C 1s to  $\sigma^*$  transition for disordered C-C bonds [93].

For the low magnitude of  $-V_{DC}$  samples, especially for the 20 W in VHF power, the peak between 288 and 315 eV is sharper than usual a-C films [119]. This sharp C 1s to  $\sigma^*$  transition feature can be observed in molecules and polymers [120–122]. Assumably, the a-C films grown by RI-PECVD with the low ion bombardment energy have polymeric bonding features. With increasing magnitude of  $-V_{DC}$ , the peak of C 1s to  $\sigma^*$  transition was broadened in the cases of both 20 and 250 W in VHF powers. This implies that polymeric structures might be destructed and formed continuous carbon-carbon networks as dominated by highly energetic ion bombardments.

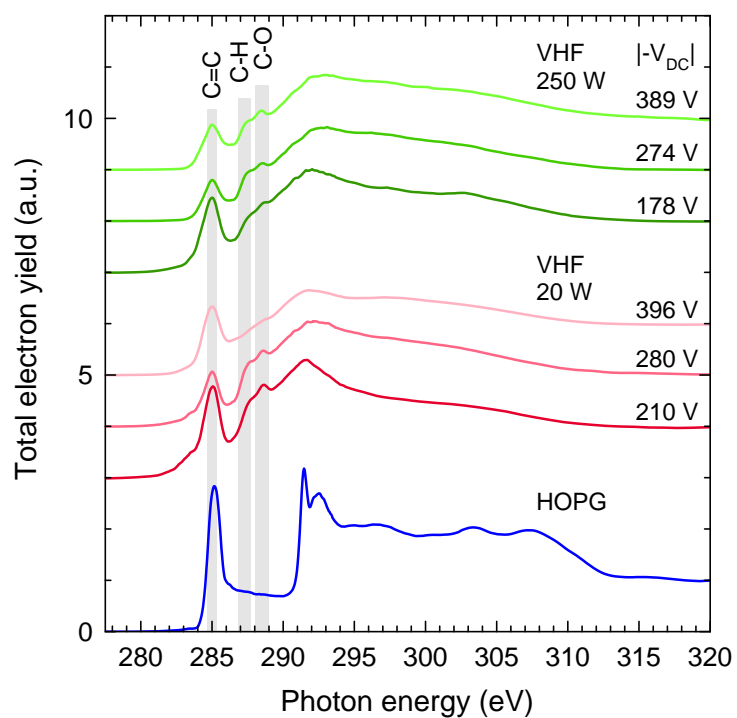


Figure 6.10 Carbon K-edge NEXAFS spectra of a-C spectra of as-grown a-C films and HOPG. Vertically dash lines are boundaries of the integration energy window. Top 3 spectra are for the samples prepared with 250 W in VHF power and middle 3 spectra are for the samples prepared with 20 W in VHF power with different  $|-V_{DC}|$ . A spectrum of HOPG is the bottom.

### 6.2.5 Discussion: H desorption and carbon-carbon continuous network formation by the ion bombardment energy flux

The decrease of both Slope/ $I_G$  and the density of dangling bonds was observed with increasing  $\Gamma_{E_i}$ . This result indicates that the decrease of H content depends on the  $\Gamma_{E_i}$  because the passivation of dangling bonds did not enhance the PL of a-C films. The passivation of dangling bonds with desorption of H by the ion bombardment can be assumed the following mechanism. It is known that the displacement of H atoms from the C-H bonding preferentially occur because of the lower displacement threshold than C [123]. This displacement depends on the ion bombardment energy. The penetration depth of ion become the deeper and the collisions in the film increase with increasing ion bombardment energy. Moreover, multiple collision in the films results in much displacement of H atom from the C-H bonding. Therefore, with increasing  $\Gamma_{E_i}$ , the flux of H subtraction from C-H bonding increases because of the energy transfer from ions to C-H bonding by an increase of collisions. The H abstraction induces to form the carbon-carbon continuous network with the close C atoms which have dangling bonds. This conversion contributes to a decrease of the density of dangling bonds with decreasing H content.

The incorporation of  $sp^2$ -C clusters, the decrease of a polymer-like feature in the NEXAFS spectra with an increase of  $\Gamma_{E_i}$  support this mechanism. Therefore, the  $\Gamma_{E_i}$  proposed in the current study is necessary to consider for controlling the H content and the carbon-carbon continuous network of the  $sp^2$ -C clusters of the a-C films deposited by PECVD.

### 6.2.6 Effects of ion bombardment energy flux on optical bandgap and electrical conductivity

Figure 6.11 shows the optical bandgap as a function of  $\Gamma_{E_i}$ . With increasing  $\Gamma_{E_i}$ , the optical bandgap decreased in the same manner in both the case with 20 and 250 W in VHF power as well as the Slope/ $I_G$  and the density of dangling bonds. This result indicated that the ion bombardment energy flux induced a decrease of H content and an increase of carbon-carbon continuous network via  $sp^2$ -C cluster incorporations of a-C films.

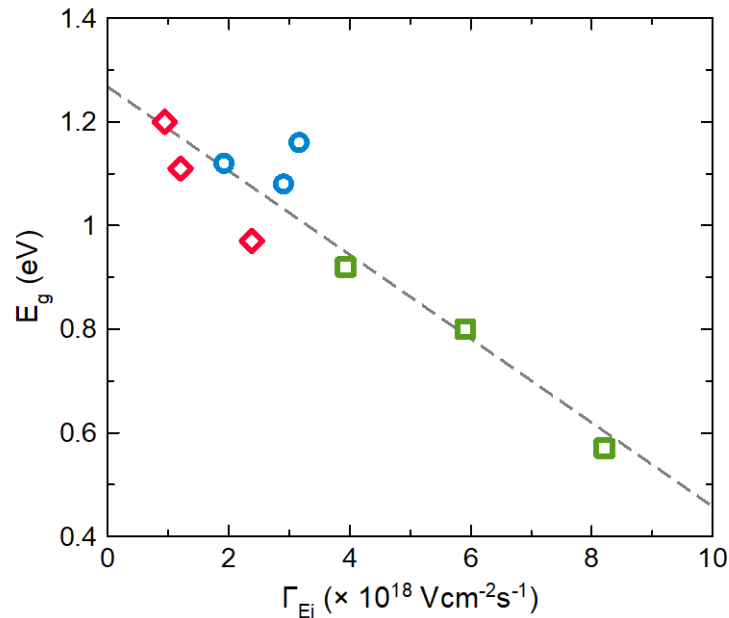


Figure 6.11 The optical bandgap as a function of  $\Gamma_{E_i}$ . Diamonds ( $\diamond$ ) correspond to 20 W in VHF power, squares ( $\square$ ) correspond to 250 W in VHF power, and circles ( $\circ$ ) correspond to 50-200 W in VHF power with 50 W in RF bias power.

Figure 6.12 shows the electrical conductivity as a function of  $\Gamma_{E_i}$ . With increasing  $\Gamma_{E_i}$ , the electrical conductivity decreased in the same manner in both the cases with 20 and 250 W in VHF powers as well as the Slope/ $I_G$  and the dangling bonds density values. The electrical conductivity increased exponentially and was very sensitive to  $\Gamma_{E_i}$ . This result indicated that the ion bombardment energy flux induced a decrease of H content and an increase of carbon-carbon continuous network via  $sp^2$ -C cluster incorporations of a-C films as well as the optical bandgap.

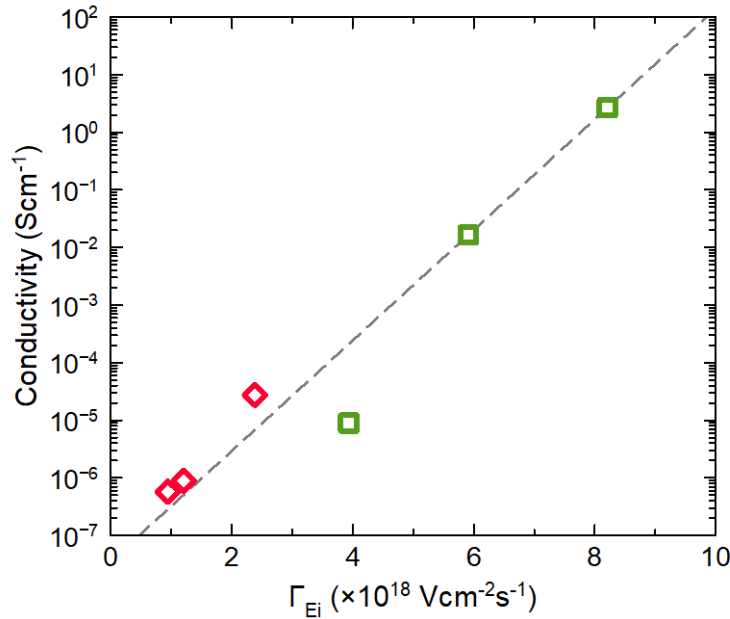


Figure 6.12 The electrical conductivity as a function of  $\Gamma_{E_i}$ . Diamonds ( $\diamond$ ) correspond to 20 W in VHF power and squares ( $\square$ ) correspond to 250 W in VHF power.

### 6.3 Discussion

The incorporation of  $sp^2$ -C clusters can be monitored by the  $[C_2]/[Ar]$  as mentioned in before. The relationship between  $C_2$  radicals and the incorporation of  $sp^2$ -C clusters can be interpreted as the following mechanism as shown in Fig 6.14. The author suggests that (i) the  $C_2$  radical in the plasma stems from the sputtered carbon from the a-C film and (ii) the amount of sputtered  $C_2$  depends on the structure of a-C film.

Usually, with increasing ion bombardment energy, the sputtering yield of carbon film increase [124]. Moreover, when the ion flux increases, the sputtered atoms increase based on the sputtering yield at the certain ion bombardment energy. The increase of  $C_2$  radical with an increase of  $\Gamma_{E_i}$  is the possible mechanism. There are some experimental observations of the production from the deposited film by ion bombardment. Oehrlein et al. reported that an increase in the emission intensity from  $C_2$  radical when a substrate covered with fluorocarbon film was RF biased [125]. Guinn et al. also reported that an optical emission spectra of  $C_2F_6$  plasma showed strong emission from  $C_2$  radical and the emission intensity of  $C_2$  radical increased by applying a bias voltage to a wafer. These results support the author's argument (i), that is, the  $C_2$  radical is the product of the sputtered a-C films by the ion bombardment.

The hypothesis (ii) can be confirmed experimentally by changing the deposition temperature. If there is the temperature dependence of the  $C_2$  radical emission intensity, the suggested mechanism will be validated. Figure 6.15 shows that the deposition temperature dependence of  $[C_2]/[Ar]$ . The discharge condition was the same as that of VHF 100 W and RF 50 W in this chapter. With increasing deposition temperature,  $[C_2]/[Ar]$  decreased. In contrast, the plot of the G position versus the  $FWHM_G$  as shown in Fig. 6.16

showed that the clear trend that an increase of deposition temperature enhanced the nc-G in the a-C films. Therefore, it is assumed that the increase of  $C_2$  radical originated from the sputtering of the a-C film depending on the  $\Gamma_{Ei}$ . However, the density of  $C_2$  radical did not represent the structure of a-C films. As a result, the incorporation of  $sp^2$ -C clusters and the  $C_2$  radical formation just showed the same trend. The monitoring of incorporation of  $sp^2$ -C clusters via the  $[C_2]/[Ar]$  can apply only in the case of changing the discharge and bias power.

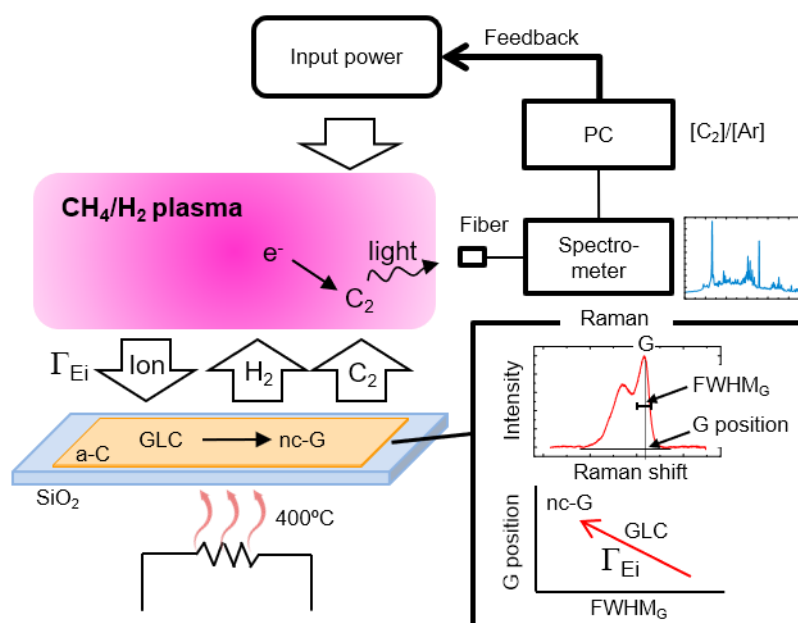


Figure 6.13 The mechanism of the  $C_2$  emission from the plasma and the control concept of  $sp^2$ -C clusters incorporation in the a-C films.

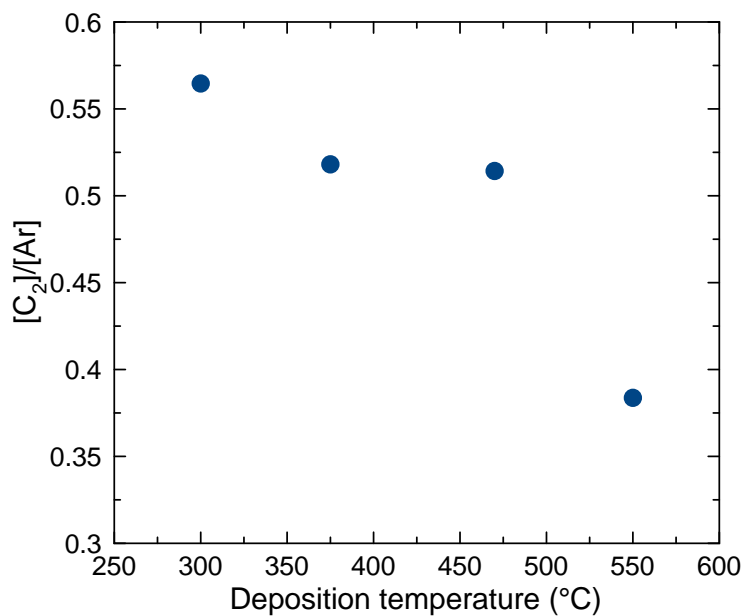


Figure 6.14 Dependence of [C<sub>2</sub>]/[Ar] on the deposition temperature.

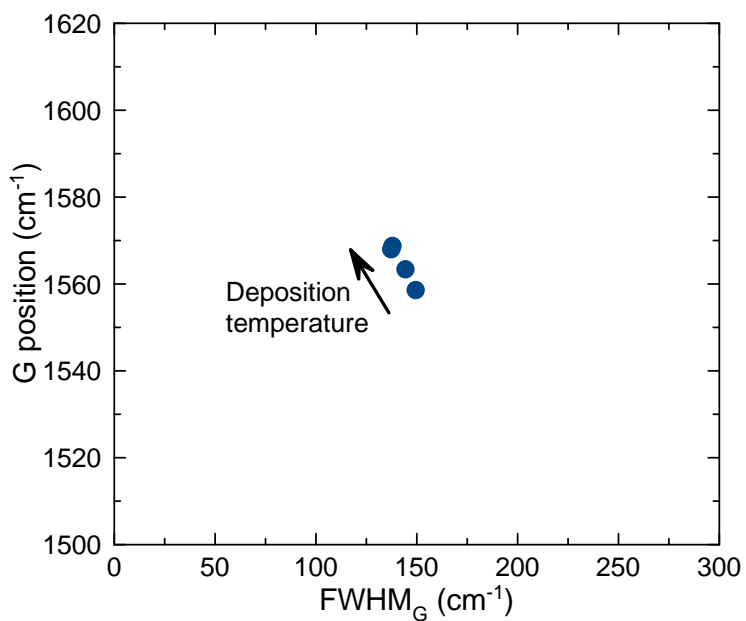


Figure 6.15 The plot of the G position versus FWHM<sub>G</sub> for the data set of deposition temperature dependence.

## 6.4 Conclusions

The author has presented the effects of ion bombardment energy flux on the PL background of Raman spectra, the dangling bond density, the incorporation of  $sp^2$ -C clusters, the bonding structure, and the optical bandgap. The ion bombardment energy flux was estimated from the plasma density at the sheath of plasma and Bohm speed based on the measurements of electron density, H excitation temperature, negative self-bias voltage, and the mass of the ions. The electron density was measured by PAP. The electron density was around  $2.0$ - $2.6 \times 10^{10} \text{ cm}^{-3}$  for the 20 W in VHF power and around  $8.8 \times 10^{10} \text{ cm}^{-3}$  for the 250 W in VHF power, and only depended on the VHF power. H excitation temperature was estimated 2 eV from the intensity ratio of  $H_\alpha$  and  $H_\beta$  of the optical emission. The ion was determined by the QMS. The  $CH_4^+$  was 50-55% of the ions in the plasma, and  $CH_3^+$  was 30-35%, and  $H_2^+$  was around 5%. The ion flux of  $4.0$ - $5.4 \times 10^{15} \text{ Vcm}^{-2}\text{s}^{-1}$  for the 20 W in VHF power and  $1.8 \times 10^{16} \text{ Vcm}^{-2}\text{s}^{-1}$  was calculated from the electron density at the sheath edge and the Bohm speed of  $CH_4$  ions. The negative self-bias voltage was controlled by the RF bias power. Thus, the ion bombardment energy flux was controlled by the VHF power and the RF bias power. The PL background of Raman spectra and the density of dangling bonds indicated that a decrease of the H content with increasing ion bombardment energy flux. The incorporation of  $sp^2$ -C clusters and a decrease of a polymer-like feature in the NEXAFS spectra with an increase of  $\Gamma_{E_i}$  support the decrease of H content by  $\Gamma_{E_i}$ . A decrease of the optical bandgap and an increase of electric conductivity are also indicated that the H desorption and the incorporation of  $sp^2$ -C clusters. Therefore, the ion bombardment energy flux was proposed as the H desorption mechanism which leads to precise control of a-C films deposited by PECVD.

## **Chapter 7 Development of the remote plasma source for the *in-situ* transmission electron microscopy under plasma irradiation**

Up to the previous chapter, the author has clarified the effect of active species in plasma on a-C film. On the other hand, it is not yet clear how the film surface and radicals undergo a reaction to form a film. In order to observe the reaction between the radical and the surface, the *in-situ* surface analysis is required. *In-situ* observation methods such as X-ray photoelectron spectroscopy (XPS), Atomic force microscopy (AFM), Ellipsometry, Fourier transform infrared spectroscopy (FTIR), and Secondary electron microscopy (SEM) have been proposed so far and have progressed to elucidate the reactions between plasma and the surface. In order to elucidate the reactions of various nanomaterials, it is necessary to perform imaging at the nanoscale and bonding structure and element analysis at the same time. Transmission electron microscope (TEM) enables us to make imaging with atomic resolution, and further, by observing electron energy loss spectroscopy, electron diffraction and EDS, element mapping and changes in the crystal structure can be observed. In this chapter, the author proposes a method for *in-situ* TEM observations while plasma irradiation is performed on material for elucidating the reactions between plasma and materials.

In the current study, graphene etching by oxygen plasma was performed as the first report of *in-situ* TEM observations with plasma irradiation.

## 7.1 Introduction of layer-by-layer thinning of graphene

The control of the layers of graphene is a key to exploiting the extraordinary properties of the materials, including its optical transmittance [126], and carrier mobility [127]. Several studies have addressed the changes in a number of layers of graphene with the application of layer-by-layer thinning in oxygen or hydrogen plasma, as reviewed by Seah and others [128]. Recently, one layer of graphene could be etched off without the effect of ions in the radio-frequency-excited oxygen plasma [129]. With lowering the ion irradiating energies, the etching of one layer of graphene could be achieved when oxygen ions and argon ions were alternately irradiated, as reported Yeom group [130–132]. Zhang and others demonstrated the thinning of graphene layers based on direct ion bombardment effect [133]. However, the details of these mechanisms whereby layers are etched have not yet been clarified. Therefore, the *in-situ* observation of graphene etching is necessary to attain a full understanding of this process.

To this end, transmission electron microscopy (TEM) methods provide a powerful means of observing atomic structures. Also, electron energy loss spectroscopy (EELS) enables us to measure the properties of not only the chemical bonding but also the layer-structure of graphene by determining the plasmon losses in the EEL spectra [134–136]. To date, *in-situ* TEM methods with environmental cells have enabled the physicochemical observations of the gas and liquid boundary reactions [137,138]. The gas-solid interactions were limited to the reporting of graphene layer sublimation by Joule heating as reported by Huang and others [139], and also gold-island formation during ion sputtering with direct-current (DC) microplasma, as reported by Tai et al. [140]. Oxygen plasma processing involves rich reactions with electrons, ions, and especially at remote for reactive neutral species such as O ( $^3P$ ,  $^1D$ ) atoms,

excited  $O_2$  ( $^1\Delta$ ) molecules. Not only the ions but also the reactive neutrals and radicals should be studied. In response to demands for a means of analyzing the reactive neutrals' and radicals' reactions, a remote-type plasma equipment was realized in the present study. That is, the author developed equipment that can be utilized with environmental cell technologies and a reaction-science high-voltage transmission electron microscope (RS-HVTEM) [141–143]. Briefly, a dedicated TEM sample holder was constructed using a system for irradiation with radicals generated by plasma.

In the present study, the author *in situ* observed the etching reactions of graphene when using a remote microwave-excited plasma source and *in-situ* RS-HVTEM. A source with a high electron density provides a high density of reactive oxygen neutrals involving O atoms to expose the graphene samples. First, etching characteristics of the graphene were analyzed from temporal changes in the TEM images. Second, the graphene layers were estimated by analyzing the plasmon loss features in the EELS spectra. Last, the crystallinity of the graphene was investigated based on the electron diffraction patterns.

## 7.2 Methods

Experimentally, a graphene sample was prepared by mechanical exfoliation from graphite (PGCX10, Panasonic). The graphene was peeled off by crushing in an agate mortar with ethanol. The crushed samples, dispersed in ethanol, were dropped onto a Cu mesh with a 167- $\mu\text{m}$  pitch and a 117- $\mu\text{m}$  hole size. Before being transferred to the vacuum chamber, the samples on the Cu mesh were dried by heating with a 100-W halogen lamp.

*In-situ* TEM observations were performed using an RS-HVTEM (JEM 1000K RS, JEOL Ltd.) operated at 1 MeV. Details of the image-recording system of the JEM 1000K RS are described elsewhere [141]. A schematic and image of the sample holder with the plasma source are shown in Fig. 7.1(a). The tip of the sample holder is inserted into the TEM environmental cell (labeled “Gas chamber”) and vacuum sealed. The plasma was generated at a discharge point 5 cm from the specimen (mounted on the sample holder) by the introduction of microwave (2.54 GHz) power, while gas was introduced from the rear of the plasma source. The specimen was not exposed to any effects of ions or light so that the electrons and ions recombined immediately at the wall surface within only a few centimeters, while a shading mechanism eliminated the emitted light. Only reactive neutral oxygen species reached the specimen surface. The gas flow rate was controlled by a mass flow controller (MFC). The O<sub>2</sub> gas was introduced with a flow rate of 1 sccm, while the pressure was around 4.6 Pa. The oxygen plasma was generated by applying 20 W in microwave power. The base pressure of the gas chamber in the RS-HVTEM was 0.19 Pa. The pressure was measured from the crystal oscillator's resonant impedance and a miniature Bayard-Alpert hot-cathode ionization gauge (crystal-ion gauge, ANELVA).

The optical emissions of the plasma were monitored during the discharge through the quartz window and introduced, via a mirror and an optical fiber, to a spectrometer (USB2000+, Ocean Optics). Figure 7.1(b) shows a typical optical emission spectrum of the oxygen plasma generated by the remote plasma source. The emission lines of the  $O_2^+$  (526, 559, 599, and 638 nm),  $O^+$  (676 nm), and O (777 and 844 nm) can be clearly observed from the center of discharge region, not the sample position. The oxygen plasma discharge was stable throughout the experiments. For a sample under this plasma condition, ions could not reach the sample, allowing the effects of reactive oxygen neutrals on graphene to be investigated.

The experimental procedure was as follows. First, initial measurements of the TEM image, diffraction, and EELS (low-loss region) were performed on the graphene before the plasma generation. Then, the plasma was generated for 1, 2, 4, 8, and 15 min. During each plasma generation, the TEM electron beam was guided away from the measurement position to prevent electron damage and subsequent damage caused by gas molecules. Measurements of the TEM images, electron diffraction, and EELS (low-loss region) were performed without any gas flow after each plasma generation. All the TEM measurements were performed at 10,000 $\times$  magnification. The author confirmed that the graphene did not change under the influence of the electron beam at this magnification. On the other hand, a greater magnitude caused damage to the graphene during the measurements. For the EELS measurements, the energy resolution (full width at half maxima, FWHM, of the zero loss peak) was 2.0 eV with an energy dispersion of 0.25 eV per channel. The EELS acquisition conditions were the same throughout the experiments, allowing the signals to be compared directly.

The TEM images and low-loss EEL spectra were analyzed using the Gatan Digital Microgram software (Gatan). To estimate the degree of etching at the graphene edges and layers, the author compared the edge length and the plasmon loss peaks for the graphene, respectively, before and after remote oxygen plasma irradiation. The elastic scattering electron peak, called the zero loss peak, was subtracted from the spectra to obtain the plasmon loss peak of the graphene by the fitted logarithm tail between 2 and 4 eV. Jovanović et al. reported that the intensity of  $\pi + \sigma$  at around 25 eV is highly dependent on the number of layers (1–15), as determined both by simulation and experiment [135]. Layers in integers were estimated by the fitting of the intensity ratio  $[\pi + \sigma]/[\pi]$  between the results of the calculations and the experiments. The obtained layers were calibrated. The areal integrated intensity for the EELS peaks was not determined. The EELS measurements were conducted by averaging over a circular area with a diameter of around 300 nm.

The thickness  $t$  of the graphene sample is proportional to the local inelastic mean free path  $\lambda$  of the electrons. Taking a ratio, the logarithmic ratio of the zero-loss electrons to the total transmitted intensity is given by

$$t/\lambda = -\ln(I_0/I_t) \quad (7-1)$$

where  $I_0$  is the area of the zero loss peak, and  $I_t$  is the total transmitted intensity [144].

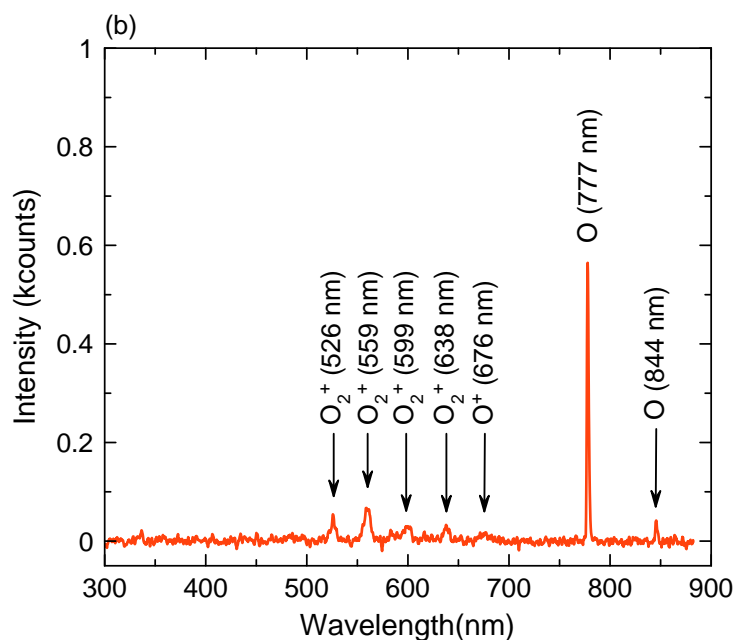
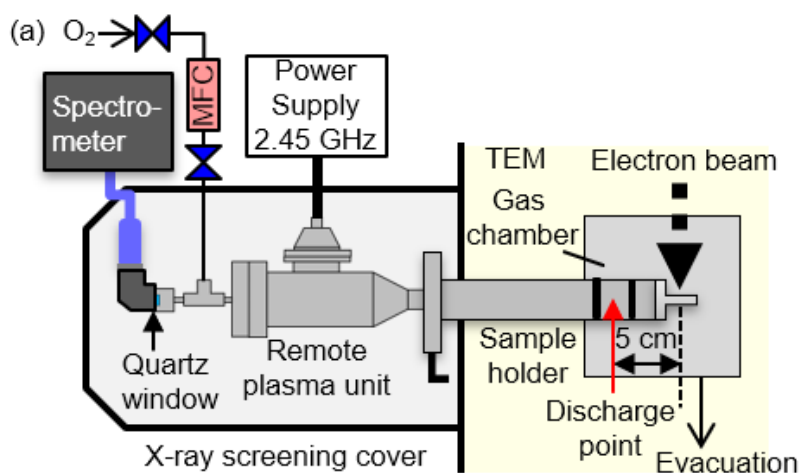


Figure 7.1 (a) Schematic of experimental setup with reaction-science TEM chamber and the environmental cell (gas chamber), equipped with the newly developed, remote-type plasma source. Plasma discharges were applied to the TEM samples, 5 cm apart. (b) The typical optical emission spectrum of remote oxygen plasma with a microwave power of 20 W, an O<sub>2</sub> flow rate of 1 sccm, and a pressure at 4.6 Pa.

### 7.3 Results and discussion

The etching of graphene by the remote oxygen plasma irradiation was observed by *in-situ* TEM. Figure 7.2 shows TEM images of the graphene edge at each reactive oxygen irradiation. The thin graphene and its edge appear at the center and right of the image. A feature of the thickly layered graphene can be seen in the top-left corner. The difference of the contrast between the basal plane of graphene and the vacuum became little when the irradiation time increased.

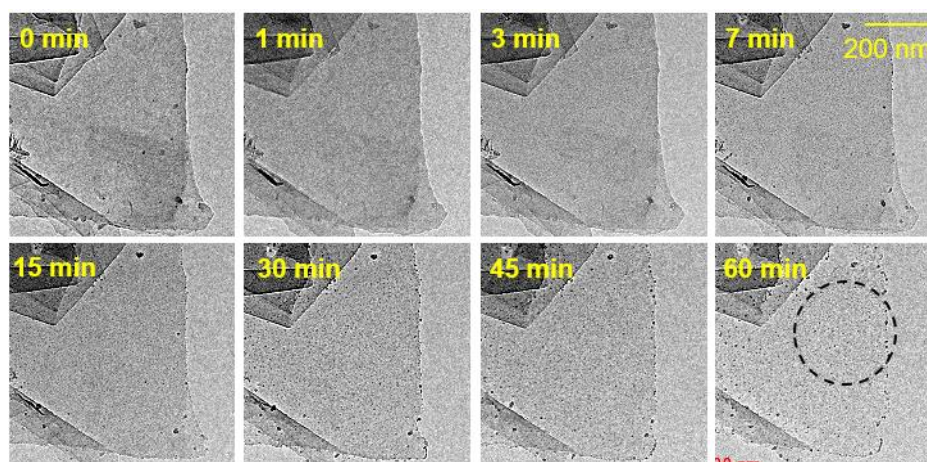


Figure 7.2 TEM images of etching from the graphene. The total remote oxygen plasma irradiation times are shown at the bottom-left corner of each figure. The dash line circle indicates the measurement area of EELS and electron diffraction.

Figure 7.3 (a) shows the plasmon region in the EEL spectra for irradiation with each remote plasma irradiation. In general, the intensities of the plasmon peaks of the EEL spectra are well correlated with the number of layers of graphene because plasmon excitations consisting of  $\pi$  and  $\sigma$  plasmons appear in the EEL spectra for graphitic materials. There are typically two plasmon modes; one is the bulk mode, while the other is the surface mode. For graphite, the two plasmon peaks are attributed to  $\pi$  at around 4.7 eV and the bulk  $\pi + \sigma$  plasmon at around 26 eV [145]. For single-layer graphene, a redshift of the  $\pi + \sigma$  feature of the graphitic materials occurs to shift the position of the  $\pi + \sigma$  plasmon peak to around 14.5 eV [146]. For multilayer graphene, the peak intensities of both the surface  $\pi + \sigma$  peak at around 15 eV and the bulk  $\pi + \sigma$  peak at around 25 eV depend on the number of layers [135,136]. From the actual spectra showing the decrease in the intensity of the  $\pi + \sigma$  feature of the bulk mode at 25 eV, the change in the layers can be estimated at each remote plasma irradiation time based on the data obtained by Jovanović and Gass [135,136]. Figure 7.3 (b) shows the relative thickness ( $t/\lambda$ ) as a function of the intensity ratio ( $[\pi + \sigma]/[\pi]$ ) of the  $\pi$  plasmon at 4.7 eV and the  $\pi + \sigma$  plasmon at 25 eV. This plot shows the linear relationship of the measured data for  $[\pi + \sigma]/[\pi]$ , and the relationship with the number of layers of graphene. This result was in good agreement with the findings of Persichetti et al. [134]. In addition, the number of layers was estimated from the relationship of  $[\pi + \sigma]/[\pi]$ , as shown in Fig. 7.3 (c). The range of  $[\pi + \sigma]/[\pi]$  for each number of layers is indicated with the thick bars on the plot. Simultaneously, the measured data are plotted on the graph.

With an increase in the remote plasma irradiation time, the number of layers of graphene decreased. The estimated number of layers constantly decreased from 8 to 4 in the estimated number of layers. Figure 7.3 (d) shows

the etching of the layers for a given remote plasma irradiation time. This behavior may give rise to the layer-by-layer thinning.

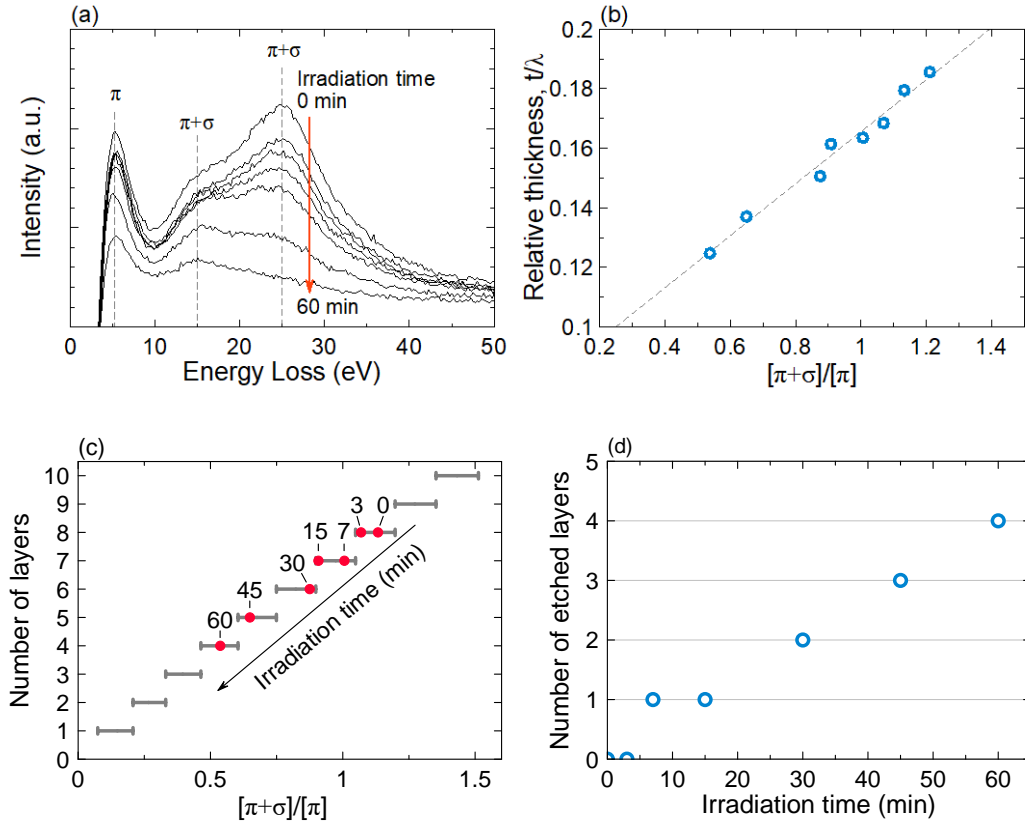


Figure 7.3 (a) Plasmon peaks of EEL spectra in the low-loss region. (b) Relative thickness ( $t/\lambda$ ) as a function of the intensity ratio of the  $\pi$  plasmon and  $\pi + \sigma$  plasmon at 25 eV ( $[\pi + \sigma]/[\pi]$ ). (c) The relationship between the number of layers and  $[\pi + \sigma]/[\pi]$  (from the data obtained by Jovanović[135]). The red dots indicate the  $[\pi + \sigma]/[\pi]$  measured in this experiment for the remote oxygen plasma irradiation. (d) A number of etched layers as a function of the irradiation time.

Next, the etching of the graphene basal plane can be seen to start from a point defect, as shown in Fig. 7.4. At 0 min, the point defect can barely be seen. At 1 min, the image contrast changes. Subsequently, as the reactive species irradiation time increased, a concentric circular shape appeared. This indicates the expansion of the defective edges on the basal plane of the graphene at the position of the point defect. On the non-defective basal plane of the graphene, no pits and no holes were observed while the reactive oxygen species were irradiated.

In addition, before the irradiation (0 min), the edges of the graphene are smooth and appear as straight lines, as shown in Fig. 7.5. As the irradiation time increases, the edge positions gradually move from the right to the left and the edge shapes become jagged. After irradiation for 60 min, the position of the graphene edge was moved by roughly 125 nm at the maximum.

From 30 min of remote oxygen plasma irradiation time, dots or particles were observed. However, these particles arose from SiO<sub>2</sub> contaminants where the quartz tube of the remote plasma source was etched off. The contaminants were evaluated by energy dispersive X-ray spectrometry (EDS).

From the TEM images, the amount of etching of the graphene from the edge, the point defect, and the tip of the edge were calculated by drawing a straight line or as the diameter of a concentric circle, and then, the length was divided by 2. Figure 7.6 shows the degree of etching of the graphene from the edge, the point defect, and the tip of an edge as functions of the remote oxygen plasma irradiation time. For the tip of edge, the images were calibrated the position, and one line was drawn. The difference in the line lengths between the initial and each irradiation time was defined as the amount of etching. The amount of etching of the edge and the point defect was almost the same. The etching rate had a linear relationship with the remote oxygen plasma

irradiation time. These etching rates were determined to be around 0.4 nm/min. The rate for the tip of the edges was determined to be around 2.1 nm/min. This indicates that graphene edge structure at the tip of the edge was zig-zag or armchair, etc.

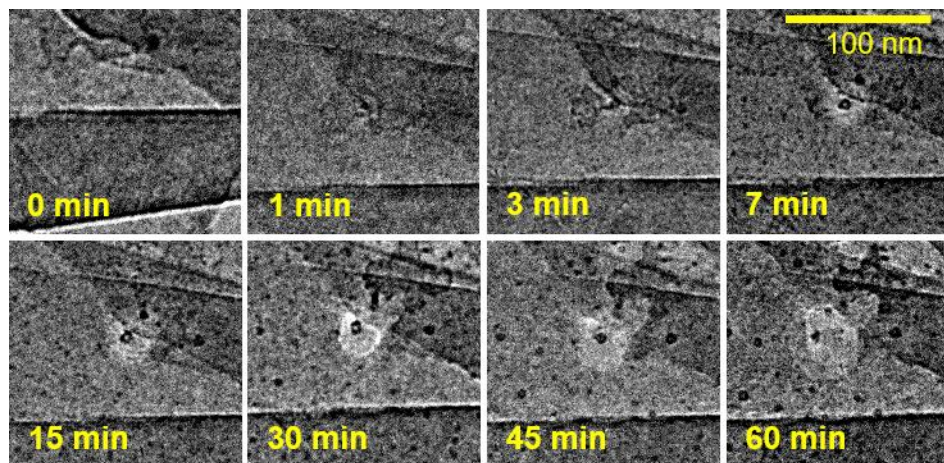


Figure 7.4 TEM images of etching from point defect at the graphene basal plane. The total remote oxygen plasma irradiation times are shown at the bottom left of each figure.

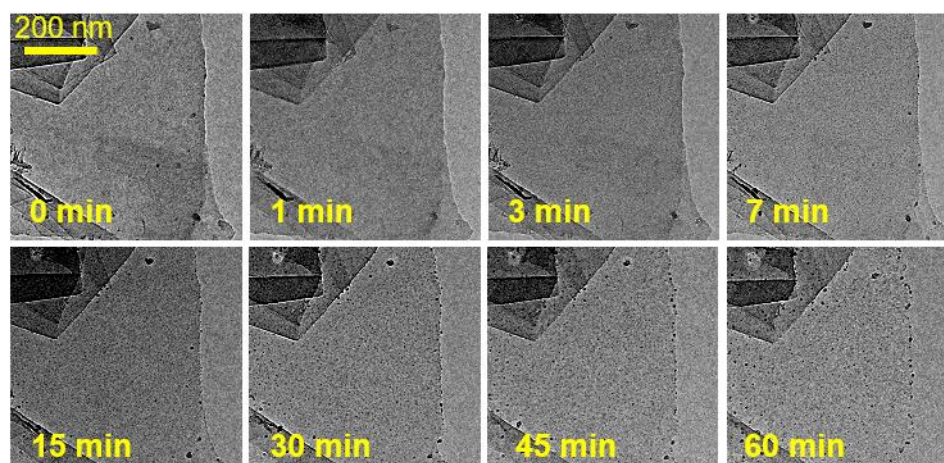


Figure 7.5 Enlarged TEM images of etching from the tip of edge.

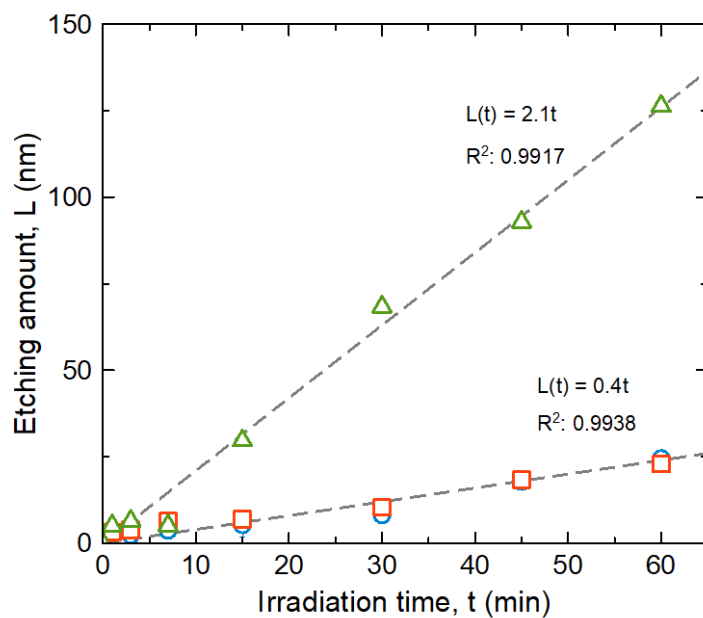


Figure 7.6 Amount of etching of graphene from edge (○), point defect (□), and the tip of edge (△). The data for the edge is the average of the three lines. The gray dashed line corresponds to the result of linear fitting with a determination coefficient ( $R^2$ ).

Figure 7.7 shows the electron diffraction pattern of the sample before and after remote plasma irradiation for 1-60 min. The electron diffraction was measured restricting the area on the smooth basal plane of the graphene. The diffraction pattern exhibits a typical six-fold symmetry which is attributed to the graphene and graphite [147,148]. With an increase in the remote plasma irradiation time, the intensity of the diffraction pattern decreased without changing the shape of the pattern. This result suggested that at least the inner bulk crystalline structure of the basal plane of the graphene did not change with the remote plasma irradiation, although the surface of the basal plane may be oxidized. The decrease in the intensity of the diffraction spots may reflect in a decrease in the number of graphene layers as a result of the remote plasma irradiation.

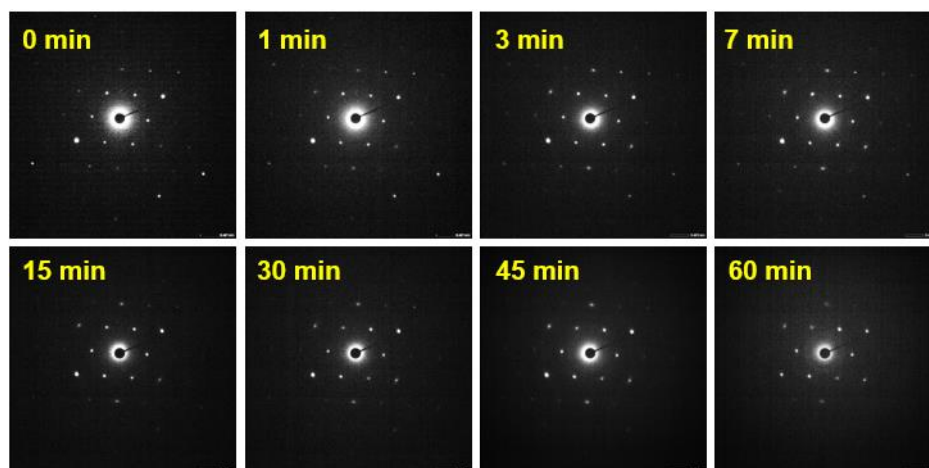


Figure 7.7 Electron diffraction pattern of graphene before and after 1-60 min remote plasma irradiation. The total remote oxygen plasma irradiation times are shown at the top left of each graph.

During the interaction between the graphene and the reactive oxygen species, etching processes take place on the graphene. These consist of three reaction schemes, as follows. (1) Adsorption of the oxygen species onto the graphene which then migrates to the planes; (2) the adsorbed oxygen adheres to the graphene edges and causes the oxidation of the carbon atoms; and (3) the oxidized carbons such as  $\text{CO}_2$  and  $\text{CO}$  are desorbed. In these etching schemes, the reaction rates for etching at the graphene edge are higher and occur preferentially with a rate-limiting step of the formation of volatile products. Thus, the etching of graphene should occur by the formation of  $\text{CO}$  and  $\text{CO}_2$  [149–152]. This scheme is interpreted as the basal plane of the graphite oxidizing to form an epoxy group bound on  $\text{C}=\text{C}$  bonds [153–158]. The epoxy is further oxidized to form a  $\text{C}-\text{C}$  bond and to dissociate into two semiquinones [159]. The semiquinones may be intermediate states for exothermic  $\text{CO}$  formation with an energy barrier higher than 2 eV, as determined from a thermodynamic estimation [154]. The experimental results supporting the etching mechanisms may differ between the edge and the basal plane. The crystalline structure of the graphene observed in the electron diffraction pattern remained unchanged from that of the bulk inner crystalline graphene, even after the removal of the surface layer by remote oxygen plasma irradiation. This behavior was in agreement with the results of TEM image observation (Fig. 7.2). No obvious defects are generated in the basal plane by the remote plasma irradiation. Although the number of layers decreased with an increase in the remote plasma irradiation, the etching rate of one layer was much faster than that of the edge when etching the  $\text{Ø}300\text{-nm}$  observation area. This implies that the surface layer was removed from not only the edge but also the basal plane.

## 7.4 Conclusions

In summary, graphene etching using microwave-excited oxygen plasma was observed *in situ* using a reaction-science high-voltage transmission electron microscope equipped with a developed remote plasma source. The etching mechanism consisting of layer-by-layer thinning of graphene, as deduced by simulation, was supported experimentally by our observations. At both the edge and on the basal plane, the etching of the graphene with the remote oxygen plasma irradiation was observed by the *in-situ* TEM method. The layers of graphene were analyzed using the peak intensity ratio of the  $\pi$  and the bulk  $\pi + \sigma$  plasmon features of the EELS spectra. Etching rates for the defective edges and tip edges were estimated to 0.4 nm/min and 2.1 nm/min, respectively. The layer-by-layer thinning rate by irradiation was such that one layer was removed every 15 min until the second layer was reached. In addition, the electron diffraction pattern of the graphene structure remained unchanged during the etching.

The author established the *in-situ* TEM observation under the remote plasma irradiation method. This method will be helpful to elucidate the reaction mechanism in the plasma and materials interface.

## Chapter 8 Summary and Conclusions

In this thesis, based on the film formation model described in Section 1.3.3, the effects of radicals and ions on a-C film were investigated to elucidate the formation mechanism of the a-C film by PECVD.

In Chapter 3, the effects of H atom and H ions on the deposition characteristics and film structure and properties were investigated. The author compared among the continuous deposition, sequential deposition with an interval, H atom, and H atom/ion. The deposited a-C films were evaluated regarding the thickness,  $sp^2$ -C clusters, PL background, density of dangling bonds, optical bandgap, conductivity. As a result, the effects of H atom were the surface dangling bonds creation by the H abstraction and enhancement of the formation of  $sp^2$ -C clusters. The effects of H ion were the dangling bonds termination by the C-H formation within the projection range and the chemical sputtering of a-C film. Both effects were confirmed at the 400°C of the surface temperature.

In Chapter 4, control of  $CH_3$  radical and its effects on  $sp^2$  fraction and hardness are investigated based on the residence time control. The results of plasma characterization by QMS showed that there is an optimum residence time to generate the  $CH_3$  in the plasma, and it related to the formation of an  $sp^3$ -C atom in the a-C film. The hardness of deposited a-C films increased with the  $CH_3$  increased. This results also implied that the  $CH_3$  radical tends to form the  $sp^3$ -C.

In Chapter 5, control of  $sp^2$ -C clusters in the a-C films based on the measurements of  $C_2$  radical density by actinometric OES was investigated. The plasma characterization was conducted by PAP, OES, and QMS. The electron density increased with an increase of the input VHF power. The  $C_2$

radical and  $C_2H_4$  increased with an increase of the electron density. The visible Raman spectroscopy was carried out to measure the  $sp^2$ -C clusters in the a-C films. The plot of G position versus  $FWHM_G$  showed that the enhancement of graphitization of a-C film could be monitored by the  $C_2$  radical density using actinometric OES.

In Chapter 6, the author has presented the effects of ion bombardment energy flux,  $\Gamma_{E_i}$ , on the PL background of Raman spectra, the dangling bond density, the incorporation of  $sp^2$ -C clusters, the bonding structure, and the optical bandgap. The  $\Gamma_{E_i}$  was estimated from the plasma density at the sheath of plasma and Bohm speed based on the measurements of electron density, H excitation temperature, negative self-bias voltage, and the mass of the ion. The electron density was measured by the PAP. The electron density was around  $2.0$ - $2.6 \times 10^{10} \text{ cm}^{-3}$  for the 20 W in VHF power, and around  $8.8 \times 10^{10} \text{ cm}^{-3}$  for the 250 W in VHF power, and only depended on the VHF power. H excitation temperature was estimated 2 eV from the intensity ratio of  $H_\alpha$  and  $H_\beta$  of the optical emission. The ion species was determined by the QMS. The  $CH_4^+$  was 50-55% of the ions in the plasma, and  $CH_3^+$  was 30-35%, and  $H_2^+$  was around 5%. The ion flux of  $4.0$ - $5.4 \times 10^{15} \text{ Vcm}^{-2}\text{s}^{-1}$  for the 20 W in VHF power, and  $1.8 \times 10^{16} \text{ Vcm}^{-2}\text{s}^{-1}$  was calculated from the electron density at the sheath edge and the Bohm speed of  $CH_4$  ion. The negative self-bias voltage was controlled by the RF bias power. Thus, the  $\Gamma_{E_i}$  was controlled by the VHF power and the RF bias power. The PL background of Raman spectra and the dangling bonds density indicated that the decrease of H content with increasing the  $\Gamma_{E_i}$ . The incorporation of  $sp^2$ -C clusters, the decrease of a polymer-like feature in the NEXAFS spectra, and the decrease of optical bandgap with an increase of  $\Gamma_{E_i}$  suggested the nc-G formation as the incorporation of  $sp^2$ -C clusters as well. A decrease of the optical bandgap and

an increase of electric conductivity were also indicated that the H desorption and the incorporation of  $sp^2$ -C clusters. Moreover, the author has also proposed that the  $C_2$  production by the  $\Gamma_{E_i}$ . Therefore, the  $\Gamma_{E_i}$  was proposed as the partial film formation mechanism which leads the precise control of a-C films deposited by PECVD.

In Chapter 7, the author proposes the new *in-situ* measurements method to observe the interaction between plasma and material by the *in-situ* transmission electron microscope with the remote plasma source developed by the authors. Firstly, the demonstration of its effectiveness to elucidate the reaction mechanism, the etching of graphene by the O remote plasma is conducted. The graphene etching using microwave-excited oxygen plasma was observed *in situ* using a reaction-science high-voltage transmission electron microscope equipped with the developed remote plasma source. The etching mechanism consisting of layer-by-layer thinning of graphene, as deduced by simulation, was supported experimentally by our observations. At both the edge and on the basal plane, the etching of the graphene with the remote oxygen plasma irradiation was observed by the *in-situ* TEM method. The layers of graphene were analyzed using the peak intensity ratio of the  $\pi$  and the bulk  $\pi + \sigma$  plasmon features of the EELS spectra. Etching rates for the defective edges of 0.4 nm/min and tip edges of 2.1 nm/min were estimated. The layer-by-layer thinning rate by irradiation was such that one layer was removed every 15 min until the second layer was reached. Also, the electron diffraction pattern of the graphene structure remained unchanged during the etching. Finally, the author established the *in-situ* TEM observation under the remote plasma irradiation method. This method will be helpful to elucidate the reaction mechanism in the plasma and materials interface.

The film formation mechanism of a-C films by a low-temperature CH<sub>4</sub>/H<sub>2</sub> plasma is summarized in Fig. 8.1. In this model, the ion subplantation induces the H abstraction by collision cascade with C-H. Through the H abstraction in the a-C film, the incorporation of sp<sup>2</sup>-C clusters is occurred. C<sub>2</sub> molecules are sputtered from the deposition surface by the ion bombardment. These reactions depend on the ion bombardment energy flux. H atoms react with the surface H bonded with C and create surface dangling bonds by H abstraction and formation of H<sub>2</sub> gas. CH<sub>3</sub> radicals stick to surface dangling bonds generated by ion bombardment and H atom. H<sub>2</sub><sup>+</sup> ions etch off the a-C films from the surface and make H rich layer in the subsurface. These phenomena occur simultaneously during the deposition. The author notes that this formation model is for the deposition temperature of 400°C at the surface. The author advocates that the control of the CH<sub>3</sub> density and the ion bombardment energy flux should be controlled based on the measurements of the electron density, the electron temperature, and reactive species including radicals and ions.

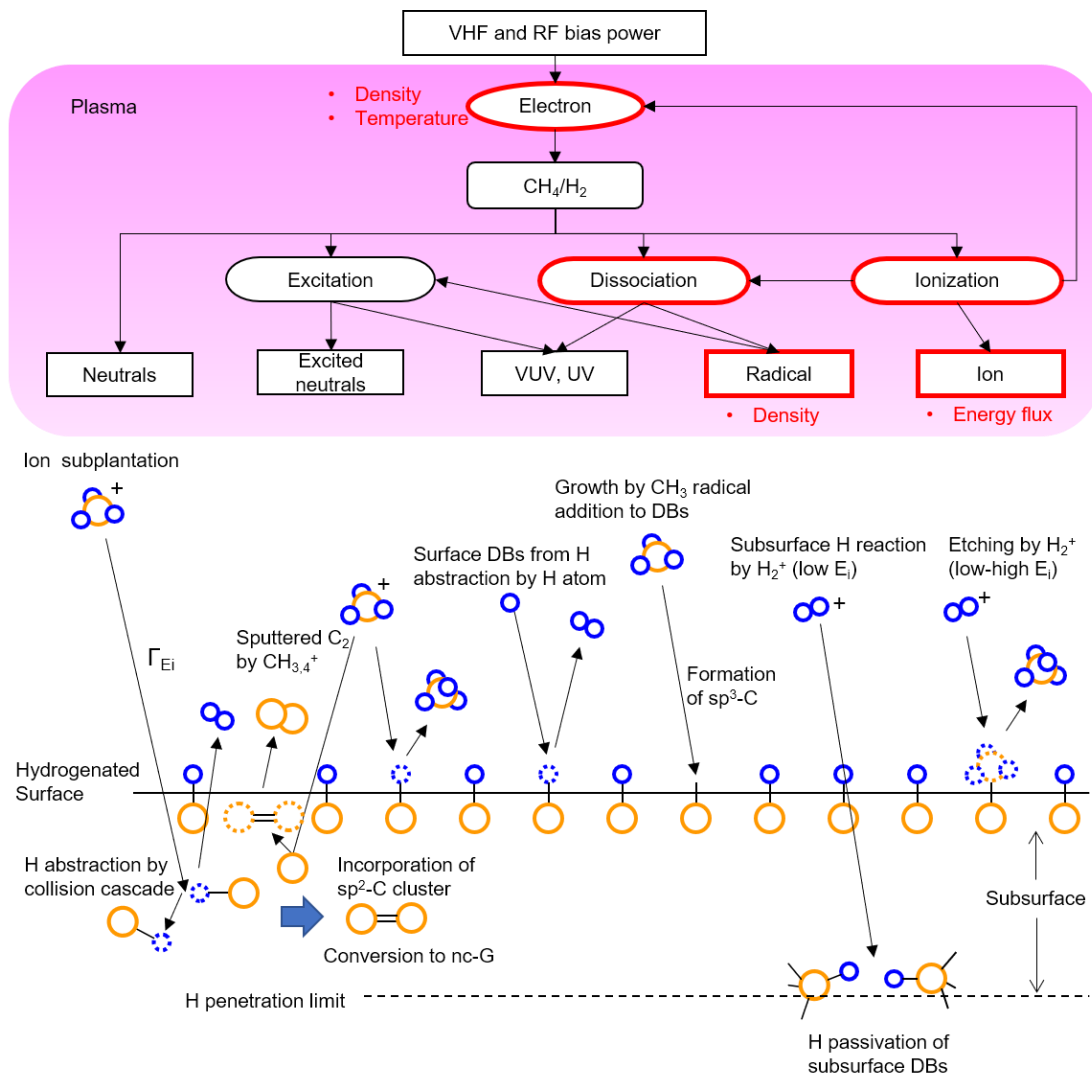


Figure 8.1 The proposed film formation mechanism by PECVD.

## Chapter 9 Remaining issues and Future perspective

In the previous chapters, the effect of H atom, H ion, CH<sub>3</sub> radical irradiation and ion bombardment energy flux by CH<sub>3,4</sub> ion in the film formation of a-C by PECVD was clarified. In this chapter, The author will describe remaining issues and the future perspective for the parts that could not be clarified in this paper.

### 1. The dependence of deposition temperature on the effects of H atom, H ion, CH<sub>3</sub> radical irradiation and ion bombardment energy flux by CH<sub>3,4</sub> ions on the film formation of a-C by PECVD

Firstly, it is considered that the temperature during film formation contributes greatly to the etching effect of hydrogen ions, the sticking probability of CH<sub>3</sub> radicals, the hydrogen desorption due to CH<sub>3,4</sub> ion impact, and the formation of the carbon-carbon continuous network. Therefore, the deposition temperature should be investigated in detail. Because the transformation from sp<sup>3</sup>-C to sp<sup>2</sup>-C due to post-annealing occurs from 400°C, the temperature used for this film formation, 400°C is a condition that is likely to form sp<sup>2</sup>-C clusters. Changes in film properties depending on the deposition temperature have been reported by many researchers, and it is known that as the deposition temperature increases, the film thickness decreases and it becomes graphite-like carbon (GLC). Usually, the elevation of deposition temperature is needed to grow the crystalline structure such as graphite and diamond. However, it has not yet been clarified whether it is an effect of temperature only or temperature enhanced interaction between the film surface and plasma irradiation. Through comprehensive studies, elucidation of the further mechanism is expected.

## **2. The mechanism of doping and conduction path of electrons, and the application of solar cell devices**

To be honest, the purpose of this a-C project was to realize a solar cell device by a-C films due to its tunable bandgap at the first time. The a-C films prepared in this work shows very small photo-induced current because they have a high density of dangling bonds. It has been reported that the Si and a-C junction shows the photovoltaic effect, but not a-C and a-C junction whether doping or not. It can be considered as the photoexcited carrier can only move within the very small range of depletion layer near the interface of the junction. The increase of carrier mobility and carrier separation of photoexcited electrons. It is considered that the carrier control is necessary based on the film formation mechanism clarified in this research.

## **3. The application of etching hard mask**

Etching is now an indispensable technology for people's lives because a semiconductor mounted on information communication terminals such as a personal computer and a smartphone cannot be produced without etching technology. In this semiconductor etching, not only the process technology but also the mask material is very important. In order to process to an arbitrary shape, it is necessary to realize the process that the semiconductor material can be etched, but the mask material cannot be etched off. An amorphous carbon film having higher etching tolerance is expected as a next-generation etching hard mask material instead of the spin coating film (organic film) which has been conventionally used. However, it is still not clear what kind of film structure is optimal. Further, the etching pattern has been miniaturized year by year, and the pattern deforms in a mask film having

high residual stress. Based on the film formation mechanism clarified in this research, it is desirable to clarify the mechanism of etching resistance and residual stress.

#### **4. *In-situ* TEM method under a plasma irradiation**

Plasma has been studied for a very long time since Langmuir named the discharge phenomenon as a “plasma.” The material process using plasma has developed greatly and is a technology indispensable to people's living as mentioned above. In the 20<sup>th</sup> century, researches on plasma irradiation on living bodies and plants were also actively undertaken. However, what is happening at the reaction interface between plasma and materials, living organisms and plants is still mysterious, and it is desirable to clarify the reaction toward various applications. The *in-situ* TEM observations under plasma irradiation developed by the authors is a very effective means to elucidate this reaction interface. Various types of *in-situ* TEM have already been developed, and some can observe *in situ* with atomic resolution. In order to elucidate the reactions between a plasma and a surface of solid materials, it is desirable to carry out observation experiments under plasma irradiation under high-resolution TEM. Also, the reactive science high voltage electron microscope (RS-HVTEM) in Nagoya University used in this study shows a very significant feature that it can observe biomaterials and very thick materials without thinning. The author believes that it is possible to observe the changes due to plasma irradiation while observing changes in cell morphology at the nanoscale. Through these experiments, the author believes that building reaction science between the plasma and the surface greatly contributes to the sustainable development of human society in the future.

## References

- [1] H.W. Kroto, J.R. Heath, S.C. O'Brien, R.F. Curl, R.E. Smalley, C60: Buckminsterfullerene, *Nature*. 318 (1985) 162. doi:10.1038/318162a0.
- [2] S. Iijima, Helical microtubules of graphitic carbon, *Nature*. 354 (1991) 56. doi:10.1038/354056a0.
- [3] Y. Wu, P. Qiao, T. Chong, Z. Shen, Carbon Nanowalls Grown by Microwave Plasma Enhanced Chemical Vapor Deposition, *Adv. Mater.* 14 (2002) 64. doi:10.1002/1521-4095(20020104)14:1<64::AID-ADMA64>3.0.CO;2-G.
- [4] B. Pan, J. Xiao, J. Li, P. Liu, C. Wang, G. Yang, Carbyne with finite length: The one-dimensional sp carbon, *Sci. Adv.* 1 (2015) e1500857. doi:10.1126/sciadv.1500857.
- [5] S.C. Ray, D. Mukherjee, S. Sarma, G. Bhattacharya, A. Mathur, S.S. Roy, J.A. McLaughlin, Functional diamond like carbon (DLC) coatings on polymer for improved gas barrier performance, *Diam. Relat. Mater.* 80 (2017) 59. doi:10.1016/j.diamond.2017.09.001.
- [6] M. Koós, M. Füle, M. Veres, S. Tóth, I. Pócsik, Multi-band structure of amorphous carbon luminescence, *Diam. Relat. Mater.* 11 (2002) 1115. doi:10.1016/S0925-9635(01)00713-0.
- [7] E.G. Gerstner, D.R. McKenzie, Fabrication and characterization of novel electronic devices using tetrahedral amorphous carbon, *Diam. Relat. Mater.* 7 (2006) 1172. doi:10.1016/S0925-9635(98)00176-9.
- [8] S. Adhikari, S. Adhikary, A.M.M. Omer, M. Rusop, H. Uchida, T. Soga, M. Umeno, Optical and structural properties of amorphous carbon thin films deposited by microwave surface-wave plasma CVD, *Diam. Relat. Mater.* 15 (2006) 188. doi:10.1016/j.diamond.2005.08.069.
- [9] J.L. Andujar, M.C. Polo, J. Esteve, J. Robertson, W.I. Milne, E. Martínez, Study of the mechanical properties of tetrahedral amorphous carbon films by nanoindentation and nanowear measurements, *Diam. Relat. Mater.* 10 (2001) 145. doi:10.1016/S0925-9635(00)00461-1.

## References

- [10] V. Tiainen, Amorphous carbon as a bio-mechanical coating — mechanical properties and biological applications, *Diam. Relat. Mater.* 10 (2001) 153. doi:10.1016/S0925-9635(00)00462-3.
- [11] K. Kanda, K. Fukuda, K. Kidena, R. Imai, M. Niibe, S. Fujimoto, K. Yokota, M. Tagawa, Hyperthermal atomic oxygen beam irradiation effect on the Ti-containing DLC film, *Diam. Relat. Mater.* 41 (2014) 49. doi:10.1016/j.diamond.2013.10.006.
- [12] K. Wazumi, Y. Koga, A. Tanaka, Tribological properties of a-C:H films on Si substrate prepared by plasma CVD in pulse-biased process, *Diam. Relat. Mater.* 12 (2003) 1018. doi:10.1016/S0925-9635(02)00391-6.
- [13] W. Jacob, W. Möller, On the structure of thin hydrocarbon films, *Appl. Phys. Lett.* 63 (1993) 1771. doi:10.1063/1.110683.
- [14] J. Robertson, Structural models of a-C and a-C:H, *Diam. Relat. Mater.* 4 (1995) 297. doi:10.1016/0925-9635(94)05264-6.
- [15] C. Chen, J. Robertson, Nature of disorder and localization in amorphous carbon, *J. Non. Cryst. Solids.* 227–230 (1998) 602. doi:10.1016/S0022-3093(98)00338-X.
- [16] S. Sattel, J. Robertson, H. Ehrhardt, Effects of deposition temperature on the properties of hydrogenated tetrahedral amorphous carbon, *J. Appl. Phys.* 82 (1997) 4566. doi:10.1063/1.366193.
- [17] S. Aisenberg, R. Chabot, Ion - Beam Deposition of Thin Films of Diamondlike Carbon, *J. Appl. Phys.* 42 (1971) 2953. doi:10.1063/1.1660654.
- [18] Y. Lifshitz, S.R. Kasi, J.W. Rabalais, Mass Selected Ion Beam Deposition: A Tool For Parametric Growth Studies, Process Development And Fabrication Of Diamondlike Films, *Adv. Mater. Manuf. Process.* 3 (1988) 157. doi:10.1080/10426918808953202.
- [19] I.I. Aksenov, V.A. Belous, V.G. Padalka, V.M. Khoroshikh, Transport of plasma streams in a curvilinear plasma-optics system, *Sov. J. Plasma Phys.* 4 (1978) 425.
- [20] M. Keidar, I.I. Beilis, R. Aharonov, D. Arbilly, R.L. Boxman, S. Goldsmith, Macroparticle distribution in a quarter-torus plasma duct of a filtered vacuum arc deposition system, *J. Phys. D. Appl. Phys.* 30 (1997) 2972. doi:10.1088/0022-3727/30/21/011.

## References

- [21] H. Inaba, K. Furusawa, S. Sasaki, Filtered Cathodic Vacuum Arc Process Conditions and Properties of Thin Tetrahedral Amorphous Carbon Films, *Jpn. J. Appl. Phys.* 43 (2004) 2681. doi:10.1143/JJAP.43.2681.
- [22] H. Takikawa, H. Tanoue, Review of Cathodic Arc Deposition for Preparing Droplet-Free Thin Films, *IEEE Trans. Plasma Sci.* 35 (2007) 992. doi:10.1109/TPS.2007.897907.
- [23] J. Robertson, Plasma Deposition of Diamond-Like Carbon, *Jpn. J. Appl. Phys.* 50 (2011) 01AF01. doi:10.1143/JJAP.50.01AF01.
- [24] Z. Zhou, I. Bello, M. Lei, K.Y. Li, C.S. Lee, S.T. Lee, Synthesis and characterization of boron carbon nitride films by radio frequency magnetron sputtering, *Surf. Coatings Technol.* 128–129 (2000) 334. doi:10.1016/S0257-8972(00)00600-9.
- [25] H.S. Jung, H.H. Park, S.B. Jung, H. Koo Baik, Bonding characteristics of Si and Ge incorporated amorphous carbon (a-C) films grown by magnetron sputtering, *Thin Solid Films.* 506–507 (2006) 77. doi:10.1016/j.tsf.2005.08.092.
- [26] J. Schwan, S. Ulrich, H. Roth, H. Ehrhardt, S. Silva, J. Robertson, R. Samlenski, R. Brenn, Tetrahedral amorphous carbon films prepared by magnetron sputtering and dc ion plating, *J. Appl. Phys.* 1416 (1996) 1. doi:10.1063/1.360979.
- [27] N. Saito, Influence of rf power on the properties of hydrogenated amorphous silicon carbon alloy films prepared by magnetron sputtering of silicon in methane-argon gas mixtures, *J. Appl. Phys.* 58 (1985) 3504. doi:10.1063/1.335775.
- [28] L. Ma, Z.W. Liu, C. De Zeng, H.Y. Yu, X.P. Zhong, X.Z. Zhang, Structure and magneto-electrical properties of Fe-C films prepared by magnetron sputtering, *Sci. China Physics, Mech. Astron.* 55 (2012) 1594. doi:10.1007/s11433-012-4763-0.
- [29] M. Aono, H. Akiyoshi, S. Kikuchi, N. Kitazawa, Y. Watanabe, Effect of substrate temperatures on amorphous carbon nitride films prepared by reactive sputtering, *J. Vac. Sci. Technol. A Vacuum, Surfaces, Film.* 26 (2008) 966. doi:10.1116/1.2919140.
- [30] N. Saito, Highly photoconductive and photosensitive hydrogenated amorphous silicon carbon alloy films prepared by magnetron sputtering, *Appl. Phys. Lett.* 46 (1985) 61. doi:10.1063/1.95853.

## References

- [31] V. Kulikovskiy, P. Bohac, F. Franc, A. Deineka, V. Vorlicek, L. Jastrabik, Hardness, intrinsic stress, and structure of the a-C and a-C:H films prepared by magnetron sputtering, *Diam. Relat. Mater.* 10 (2001) 1076. doi:10.1016/S0925-9635(00)00525-2.
- [32] S.C. Seo, D.C. Ingram, H.H. Richardson, Effect of substrate bias on the properties of diamondlike carbon films deposited using unbalanced magnetron sputtering, *J. Vac. Sci. Technol. A Vacuum, Surfaces, Film.* 13 (1995) 2856. doi:10.1116/1.579604.
- [33] W. Dai, H. Zheng, G. Wu, A. Wang, Effect of bias voltage on growth property of Cr-DLC film prepared by linear ion beam deposition technique, *Vacuum.* 85 (2010) 231. doi:10.1016/j.vacuum.2010.06.001.
- [34] S. Zhang, X. Lam Bui, Y. Fu, Magnetron sputtered hard a-C coatings of very high toughness, *Surf. Coatings Technol.* 167 (2003) 137. doi:10.1016/S0257-8972(02)00900-3.
- [35] V. Kouznetsov, K. Macák, J.M. Schneider, U. Helmersson, I. Petrov, A novel pulsed magnetron sputter technique utilizing very high target power densities, *Surf. Coatings Technol.* 122 (1999) 290. doi:10.1016/S0257-8972(99)00292-3.
- [36] A.P. Ehiasarian, W.D. Münz, L.G. Hultman, U. Helmersson, I. Petrov, High power pulsed magnetron sputtered CrN<sub>x</sub> films, *Surf. Coatings Technol.* 163–164 (2003) 267. doi:10.1016/S0257-8972(02)00479-6.
- [37] Y. Zhang, K. Ishikawa, M. Mozetič, T. Tsutsumi, H. Kondo, M. Sekine, M. Hori, Polyethylene terephthalate (PET) surface modification by VUV and neutral active species in remote oxygen or hydrogen plasmas, *Plasma Process. Polym.* (2019) 1800175. doi:10.1002/ppap.201800175.
- [38] M.A. Lieberman, A.J. Lichtenberg, *Principles of plasma discharges and materials processing*, Wiley-Interscience, 2005.
- [39] J. Robertson, Diamond-like amorphous carbon, *Mater. Sci. Eng. R Reports.* 37 (2002) 129. doi:10.1016/S0927-796X(02)00005-0.
- [40] Y. Miyagawa, H. Nakadate, M. Ikeyama, S. Nakao, S. Miyagawa, Dynamic MC simulation for a-C:H deposition in methane plasma based on subplantation model, *Diam. Relat. Mater.* 12 (2003) 927. doi:10.1016/S0925-9635(02)00223-6.

## References

- [41] J. Robertson, Deposition mechanisms for promoting  $sp^3$  bonding in diamond-like carbon, *Diam. Relat. Mater.* 2 (1993) 984. doi:10.1016/0925-9635(93)90262-Z.
- [42] W. Möller, Modelling and computer simulation of ion-beam- and plasma-assisted film growth, *Thin Solid Films.* 228 (1993) 319. doi:10.1016/0040-6090(93)90625-Y.
- [43] A. von Keudell, W. Jacob, Elementary processes in plasma–surface interaction: H-atom and ion-induced chemisorption of methyl on hydrocarbon film surfaces, *Prog. Surf. Sci.* 76 (2004) 21. doi:10.1016/j.progsurf.2004.05.001.
- [44] Y. Abe, S. Kawashima, A. Fukushima, Y. Lu, K. Takeda, H. Kondo, K. Ishikawa, M. Sekine, M. Hori, Impact of hydrogen radical-injection plasma on fabrication of microcrystalline silicon thin film for solar cells, *J. Appl. Phys.* 113 (2013) 033304. doi:10.1063/1.4778608.
- [45] S. Imai, H. Kondo, H. Cho, H. Kano, K. Ishikawa, M. Sekine, M. Hiramatsu, M. Ito, M. Hori, High-durability catalytic electrode composed of Pt nanoparticle-supported carbon nanowalls synthesized by radical-injection plasma-enhanced chemical vapor deposition, *J. Phys. D. Appl. Phys.* 50 (2017) 40LT01. doi:10.1088/1361-6463/aa8131.
- [46] M. Hiramatsu, M. Hori, Fabrication of Carbon Nanowalls Using Novel Plasma Processing, *Jpn. J. Appl. Phys.* 45 (2006) 5522. doi:10.1143/JJAP.45.5522.
- [47] M. Hiramatsu, K. Shiji, H. Amano, M. Hori, Fabrication of vertically aligned carbon nanowalls using capacitively coupled plasma-enhanced chemical vapor deposition assisted by hydrogen radical injection, *Appl. Phys. Lett.* 84 (2004) 4708. doi:10.1063/1.1762702.
- [48] S. Kondo, S. Kawai, W. Takeuchi, K. Yamakawa, S. Den, H. Kano, M. Hiramatsu, M. Hori, Initial growth process of carbon nanowalls synthesized by radical injection plasma-enhanced chemical vapor deposition, *J. Appl. Phys.* 106 (2009) 094302. doi:10.1063/1.3253734.
- [49] H.J. Cho, H. Kondo, K. Ishikawa, M. Sekine, M. Hiramatsu, M. Hori, Density control of carbon nanowalls grown by  $CH_4/H_2$  plasma and their electrical properties, *Carbon.* 68 (2014) 380. doi:10.1016/j.carbon.2013.11.014.

## References

- [50] W. Takeuchi, M. Ura, M. Hiramatsu, Y. Tokuda, H. Kano, M. Hori, Electrical conduction control of carbon nanowalls, *Appl. Phys. Lett.* 92 (2008) 213103. doi:10.1063/1.2936850.
- [51] H. Sugiura, L. Jia, H. Kondo, K. Ishikawa, T. Tsutsumi, T. Hayashi, K. Takeda, M. Sekine, M. Hori, Effects of gas residence time of CH<sub>4</sub>/H<sub>2</sub> on sp<sup>2</sup> fraction of amorphous carbon films and dissociated methyl density during radical-injection plasma-enhanced chemical vapor deposition, *Jpn. J. Appl. Phys.* 57 (2018) 06JE03. doi:10.7567/JJAP.57.06JE03.
- [52] L. Jia, H. Sugiura, H. Kondo, K. Takeda, K. Ishikawa, O. Oda, M. Sekine, M. Hiramatsu, M. Hori, Effect of gas residence time on near-edge X-ray absorption fine structures of hydrogenated amorphous carbon films grown by plasma-enhanced chemical vapor deposition, *Jpn. J. Appl. Phys.* 55 (2016) 040305. doi:10.7567/JJAP.55.040305.
- [53] M. Tomatsu, M. Hiramatsu, J.S. Foord, H. Kondo, K. Ishikawa, M. Sekine, K. Takeda, M. Hori, Hydrogen peroxide sensor based on carbon nanowalls grown by plasma-enhanced chemical vapor deposition, *Jpn. J. Appl. Phys.* 56 (2017) 06HF03. doi:10.7567/JJAP.56.06HF03.
- [54] M. Hiramatsu, M. Hori, *Carbon nanowalls : synthesis and emerging applications*, Springer, 2010.
- [55] M. Hiramatsu, S. Mitsuguchi, T. Horibe, H. Kondo, M. Hori, H. Kano, Fabrication of Carbon Nanowalls on Carbon Fiber Paper for Fuel Cell Application, *Jpn. J. Appl. Phys.* 52 (2013) 01AK03. doi:10.7567/JJAP.52.01AK03.
- [56] H. Watanabe, H. Kondo, M. Sekine, M. Hiramatsu, M. Hori, Control of Super Hydrophobic and Super Hydrophilic Surfaces of Carbon Nanowalls Using Atmospheric Pressure Plasma Treatments, *Jpn. J. Appl. Phys.* 51 (2012) 01AJ07. doi:10.1143/JJAP.51.01AJ07.
- [57] H. Watanabe, H. Kondo, M. Hiramatsu, M. Sekine, S. Kumar, K. Ostrikov, M. Hori, Surface Chemical Modification of Carbon Nanowalls for Wide-Range Control of Surface Wettability, *Plasma Process. Polym.* 10 (2013) 582. doi:10.1002/ppap.201200141.

## References

- [58] T. Horibe, H. Kondo, K. Ishikawa, H. Kano, M. Sekine, M. Hiramatsu, M. Hori, Supercritical Fluid Deposition of High-Density Nanoparticles of Photocatalytic TiO<sub>2</sub> on Carbon Nanowalls, *Appl. Phys. Express.* 6 (2013) 045103. doi:10.7567/APEX.6.045103.
- [59] H. Shimoeda, H. Kondo, K. Ishikawa, M. Hiramatsu, M. Sekine, M. Hori, Hierarchical regrowth of flowerlike nanographene sheets on oxygen-plasma-treated carbon nanowalls, *Appl. Phys. Express.* 7 (2014) 046201. doi:10.7567/APEX.7.046201.
- [60] H. Shimoeda, H. Kondo, K. Ishikawa, M. Hiramatsu, M. Sekine, M. Hori, Nanostructure modification to carbon nanowall surface employing hydrogen peroxide solution, *Jpn. J. Appl. Phys.* 53 (2014) 040305. doi:10.7567/JJAP.53.040305.
- [61] H.J. Cho, H. Kondo, K. Ishikawa, M. Sekine, M. Hiramatsu, M. Hori, Effects of nitrogen plasma post-treatment on electrical conduction of carbon nanowalls, *Jpn. J. Appl. Phys.* 53 (2014) 040307. doi:10.7567/JJAP.53.040307.
- [62] L. Jia, H. Sugiura, H. Kondo, K. Takeda, K. Ishikawa, O. Oda, M. Sekine, M. Hiramatsu, M. Hori, Effects of Radical Species on Structural and Electronic Properties of Amorphous Carbon Films Deposited by Radical-Injection Plasma-Enhanced Chemical Vapor Deposition, *Plasma Process. Polym.* 13 (2016) 730. doi:10.1002/ppap.201500229.
- [63] S. Kondo, M. Hori, K. Yamakawa, S. Den, H. Kano, M. Hiramatsu, Highly reliable growth process of carbon nanowalls using radical injection plasma-enhanced chemical vapor deposition, *J. Vac. Sci. Technol. B Microelectron. Nanom. Struct.* 26 (2008) 1294. doi:10.1116/1.2938397.
- [64] M. Hiramatsu, H. Kondo, M. Hori, Graphene Nanowalls, in: *New Prog. Graphene Res.*, InTech, 2013. doi:10.5772/51528.
- [65] Y.A. Mankelevich, P.W. May, New insights into the mechanism of CVD diamond growth: Single crystal diamond in MW PECVD reactors, *Diam. Relat. Mater.* 17 (2008) 1021. doi:10.1016/j.diamond.2008.03.022.
- [66] H. Toyota, S. Nomura, S. Mukasa, H. Yamashita, T. Shimo, S. Okuda, A consideration of ternary C–H–O diagram for diamond deposition using microwave

## References

- in-liquid and gas phase plasma, *Diam. Relat. Mater.* 20 (2011) 1255.  
doi:10.1016/J.DIAMOND.2011.07.010.
- [67] T. Ueyama, Y. Fukunaga, T. Tsutsumi, K. Takeda, H. Kondo, K. Ishikawa, M. Sekine, M. Iwata, Y. Ohya, H. Sugai, M. Hori, Electron behaviors in afterglow of synchronized dc-imposed pulsed fluorocarbon-based plasmas, *Jpn. J. Appl. Phys.* 56 (2017) 06HC03. doi:10.7567/JJAP.56.06HC03.
- [68] Y. Ohya, K. Ishikawa, T. Komuro, T. Yamaguchi, K. Takeda, H. Kondo, M. Sekine, M. Hori, Spatial profiles of interelectrode electron density in direct current superposed dual-frequency capacitively coupled plasmas, *J. Phys. D: Appl. Phys.* 50 (2017) 155201. doi:10.1088/1361-6463/aa60f7.
- [69] Y. Ohya, M. Iwata, K. Ishikawa, M. Sekine, M. Hori, H. Sugai, Rapid electron density decay observed by surface-wave probe in afterglow of pulsed fluorocarbon-based plasma, *Jpn. J. Appl. Phys.* 55 (2016) 080309. doi:10.7567/JJAP.55.080309.
- [70] T. Yamaguchi, T. Komuro, C. Koshimizu, S. Takashima, K. Takeda, H. Kondo, K. Ishikawa, M. Sekine, M. Hori, Direct current superposed dual-frequency capacitively coupled plasmas in selective etching of SiOCH over SiC, *J. Phys. D: Appl. Phys.* 45 (2012) 025203. doi:10.1088/0022-3727/45/2/025203.
- [71] H. Kokura, K. Nakamura, I.P. Ghanashev, H. Sugai, Plasma Absorption Probe for Measuring Electron Density in an Environment Soiled with Processing Plasmas, *Jpn. J. Appl. Phys.* 38 (1999) 5262. doi:10.1143/JJAP.38.5262.
- [72] J.W. Coburn, M. Chen, Optical emission spectroscopy of reactive plasmas: A method for correlating emission intensities to reactive particle density, *J. Appl. Phys.* 51 (1980) 3134. doi:10.1063/1.328060.
- [73] C. Park, Hydrogen line ratios as electron temperature indicators in nonequilibrium plasmas, *J. Quant. Spectrosc. Radiat. Transf.* 12 (1972) 323. doi:10.1016/0022-4073(72)90050-7.
- [74] H. Toyoda, H. Kojima, H. Sugai, Mass spectroscopic investigation of the CH<sub>3</sub> radicals in a methane rf discharge, *Appl. Phys. Lett.* 54 (1989) 1507. doi:10.1063/1.101336.
- [75] N. Wada, P.J. Gaczi, S.A. Solin, "Diamond-like" 3-fold coordinated amorphous carbon, *J. Non. Cryst. Solids.* 35–36 (1980) 543. doi:10.1016/0022-3093(80)90651-1.

## References

- [76] S.R. Sails, D.J. Gardiner, M. Bowden, J. Savage, D. Rodway, Monitoring the quality of diamond films using Raman spectra excited at 514.5 nm and 633 nm, *Diam. Relat. Mater.* 5 (1996) 589. doi:10.1016/0925-9635(96)90031-X.
- [77] A. Ferrari, J. Robertson, Interpretation of Raman spectra of disordered and amorphous carbon, *Phys. Rev. B.* 61 (2000) 14095. doi:10.1103/PhysRevB.61.14095.
- [78] L. Zhang, X. Wei, Y. Lin, F. Wang, A ternary phase diagram for amorphous carbon, *Carbon.* 94 (2015) 202. doi:10.1016/j.carbon.2015.06.055.
- [79] A. Merlen, J. Buijnsters, C. Pardanaud, A Guide to and Review of the Use of Multiwavelength Raman Spectroscopy for Characterizing Defective Aromatic Carbon Solids: from Graphene to Amorphous Carbons, *Coatings.* 7 (2017) 153. doi:10.3390/coatings7100153.
- [80] C. Casiraghi, A.C. Ferrari, J. Robertson, Raman spectroscopy of hydrogenated amorphous carbons, *Phys. Rev. B.* 72 (2005) 085401. doi:10.1103/PhysRevB.72.085401.
- [81] F. Rose, N. Wang, R. Smith, Q.-F. Xiao, H. Inaba, T. Matsumura, Y. Saito, H. Matsumoto, Q. Dai, B. Marchon, F. Mangolini, R.W. Carpick, Complete characterization by Raman spectroscopy of the structural properties of thin hydrogenated diamond-like carbon films exposed to rapid thermal annealing, *J. Appl. Phys.* 116 (2014) 123516. doi:10.1063/1.4896838.
- [82] B. Marchon, Jing Gui, K. Grannen, G.C. Rauch, J.W. Ager, S.R.P. Silva, J. Robertson, Photoluminescence and Raman spectroscopy in hydrogenated carbon films, *IEEE Trans. Magn.* 33 (1997) 3148. doi:10.1109/20.617873.
- [83] X. Zhou, T. Suzuki, H. Nakajima, K. Komatsu, K. Kanda, H. Ito, H. Saitoh, Structural analysis of amorphous carbon films by spectroscopic ellipsometry, RBS/ERDA, and NEXAFS, *Appl. Phys. Lett.* 110 (2017) 201902. doi:10.1063/1.4983643.
- [84] G. Adamopoulos, J. Robertson, N. a. Morrison, C. Godet, Hydrogen content estimation of hydrogenated amorphous carbon by visible Raman spectroscopy, *J. Appl. Phys.* 96 (2004) 6348. doi:10.1063/1.1811397.

## References

- [85] J.G. Buijnsters, R. Gago, I. Jiménez, M. Camero, F. Agulló-Rueda, C. Gómez-Aleixandre, Hydrogen quantification in hydrogenated amorphous carbon films by infrared, Raman, and x-ray absorption near edge spectroscopies, *J. Appl. Phys.* 105 (2009) 093510. doi:10.1063/1.3103326.
- [86] K. Kanda, M. Niibe, A. Wada, H. Ito, T. Suzuki, T. Ohana, N. Ohtake, H. Saitoh, Comprehensive Classification of Near-Edge X-ray Absorption Fine Structure Spectra of Si-Containing Diamond-Like Carbon Thin Films, *Jpn. J. Appl. Phys.* 52 (2013) 095504. doi:10.7567/JJAP.52.095504.
- [87] S. Tunmee, R. Supruangnet, H. Nakajima, X. Zhou, S. Arakawa, T. Suzuki, K. Kanda, H. Ito, K. Komatsu, H. Saitoh, Study of Synchrotron Radiation Near-Edge X-Ray Absorption Fine-Structure of Amorphous Hydrogenated Carbon Films at Various Thicknesses, *J. Nanomater.* 2015 (2015) 1. doi:10.1155/2015/276790.
- [88] Y. Haruyama, T. Kitagawa, K. Kanda, S. Matsui, T. Gejo, N. Toyoda, I. Yamada, X-ray photoelectron spectroscopy study of diamond-like carbon thin films formed by Ar gas cluster ion beam-assisted fullerene deposition, *Jpn. J. Appl. Phys.* 47 (2008) 3380. doi:10.1143/JJAP.47.3380.
- [89] B. Watts, L. Thomsen, P.C.C. Dastoor, Methods in carbon K-edge NEXAFS: Experiment and analysis, *J. Electron Spectros. Relat. Phenomena.* 151 (2006) 105. doi:10.1016/j.elspec.2005.11.006.
- [90] S.G. Urquhart, A.P. Hitchcock, A.P. Smith, H.W. Ade, W. Lidy, E.G. Rightor, G.E. Mitchell, NEXAFS spectromicroscopy of polymers: overview and quantitative analysis of polyurethane polymers, *J. Electron Spectros. Relat. Phenomena.* 100 (1999) 119. doi:10.1016/S0368-2048(99)00043-2.
- [91] O. Dhez, H. Ade, S.G. Urquhart, Calibrated NEXAFS spectra of some common polymers, 128 (2003) 85.
- [92] F. Mangolini, J.B. McClimon, R.W. Carpick, Quantitative Evaluation of the Carbon Hybridization State by Near Edge X-ray Absorption Fine Structure Spectroscopy, *Anal. Chem.* 88 (2016) 2817. doi:10.1021/acs.analchem.5b04525.
- [93] J. Stöhr, *NEXAFS Spectroscopy*, Springer Berlin Heidelberg, Heidelberg, 1992. doi:10.1007/978-3-662-02853-7.

## References

- [94] Y. Muramatsu, E.M. Gullikson, High-resolution CK-XANES of graphitic carbons measured under the magic angle, *Adv. X-Ray Chem. Anal. Japan.* (2011) 267. <https://ci.nii.ac.jp/naid/40018795861> (accessed November 23, 2018).
- [95] S. Ohmagari, T. Yoshitake, A. Nagano, S. AL-Riyami, R. Ohtani, H. Setoyama, E. Kobayashi, K. Nagayama, Near-Edge X-Ray Absorption Fine Structure of Ultrananocrystalline Diamond/Hydrogenated Amorphous Carbon Films Prepared by Pulsed Laser Deposition, *J. Nanomater.* 2009 (2009) 1. doi:10.1155/2009/876561.
- [96] C. Lenardi, P. Piseri, V. Briois, C.E. Bottani, A.L. Bassi, P. Milani, Near-edge x-ray absorption fine structure and Raman characterization of amorphous and nanostructured carbon films, *J. Appl. Phys.* 85 (1999) 7159. doi:10.1063/1.370527.
- [97] A. V. Sumant, P.U.P.A. Gilbert, D.S. Grierson, A.R. Konicek, M. Abrecht, J.E. Butler, T. Feygelson, S.S. Rotter, R.W. Carpick, Surface composition, bonding, and morphology in the nucleation and growth of ultra-thin, high quality nanocrystalline diamond films, *Diam. Relat. Mater.* 16 (2007) 718. doi:10.1016/J.DIAMOND.2006.12.011.
- [98] A. Saikubo, N. Yamada, K. Kanda, S. Matsui, T. Suzuki, K. Niihara, H. Saitoh, Comprehensive classification of DLC films formed by various methods using NEXAFS measurement, *Diam. Relat. Mater.* 17 (2008) 1743. doi:10.1016/J.DIAMOND.2008.01.095.
- [99] Y. Muramatsu, K. Shimomura, T. Katayama, E.M. Gullikson, Total Electron Yield Soft X-ray Absorption Spectroscopy in the C K Region of the Mixtures of Graphitic Carbons and Diamond for Quantitative Analysis of the  $sp^2/sp^3$ -Hybridized Carbon Ratio, *Jpn. J. Appl. Phys.* 48 (2009) 066514. doi:10.1143/JJAP.48.066514.
- [100] A. Von Keudell, M. Meier, C. Hopf, Growth mechanism of amorphous hydrogenated carbon, *Diam. Relat. Mater.* 11 (2002) 969.
- [101] N. Mutsukura, S.-I. Inoue, Y. Machi, Deposition mechanism of hydrogenated hard - carbon films in a  $CH_4$  rf discharge plasma, *J. Appl. Phys.* 72 (1992) 43. doi:10.1063/1.352145.
- [102] H. Sugai, H. Kojima, A. Ishida, H. Toyoda, Spatial distribution of  $CH_3$  and  $CH_2$  radicals in a methane rf discharge, *Appl. Phys. Lett.* 56 (1990) 2616. doi:10.1063/1.103264.

## References

- [103] H. Chatham, D. Hils, R. Robertson, A. Gallagher, Total and partial electron collisional ionization cross sections for CH<sub>4</sub>, C<sub>2</sub>H<sub>6</sub>, SiH<sub>4</sub>, and Si<sub>2</sub>H<sub>6</sub>, *J. Chem. Phys.* 81 (1984) 1770. doi:10.1063/1.447848.
- [104] R. van Harrevelt, Photodissociation of methane: Exploring potential energy surfaces, *J. Chem. Phys.* 125 (2006) 124302. doi:10.1063/1.2335441.
- [105] J. Laulainen, S. Aleiferis, T. Kalvas, H. Koivisto, R. Kronholm, O. Tarvainen, Hydrogen plasma induced photoelectron emission from low work function cesium covered metal surfaces, *Phys. Plasmas*. 24 (2017) 103502. doi:10.1063/1.4998005.
- [106] H. Akasaka, N. Ohtake, Characterization of amorphous carbon films deposited by surface wave plasma CVD, *Diam. Relat. Mater.* 14 (2005) 1828. doi:10.1016/j.diamond.2005.09.026.
- [107] N. Sirse, T. Tsutsumi, M. Sekine, M. Hori, A.R. Ellingboe, Measurement of F<sup>-</sup>, O<sup>-</sup> and CF<sub>3</sub><sup>-</sup> densities in 60 and 100 MHz asymmetric capacitively coupled plasma discharge produced in an Ar/O<sub>2</sub>/C<sub>4</sub>F<sub>8</sub> gas mixture, *J. Phys. D. Appl. Phys.* 50 (2017) 335205. doi:10.1088/1361-6463/aa77c4.
- [108] P. Chabert, N. Braithwaite, *Physics of Radio-Frequency Plasmas*, Cambridge University Press, Cambridge, 2011. doi:10.1017/CBO9780511974342.
- [109] P. John, J.R. Rabeau, J.I.B. Wilson, The cavity ring-down spectroscopy of C<sub>2</sub> in a microwave plasma, *Diam. Relat. Mater.* 11 (2002) 608. doi:10.1016/S0925-9635(01)00653-7.
- [110] C. Suzuki, K. Sasaki, K. Kadota, Formation of C<sub>2</sub> Radicals in High-Density C<sub>4</sub>F<sub>8</sub> Plasmas Studied by Laser-Induced Fluorescence, *Jpn. J. Appl. Phys.* 38 (1999) 6896. doi:10.1143/JJAP.38.6896.
- [111] P.S. Skell, L.M. Jackman, S. Ahmed, M.L. McKee, P.B. Shevlin, Some reactions and properties of molecular diatomic carbon C<sub>2</sub>. An experimental and theoretical treatment, *J. Am. Chem. Soc.* 111 (1989) 4422. doi:10.1021/ja00194a042.
- [112] P.S. Skell, J.H. Plonka, Chemistry of the singlet and triplet C<sub>2</sub> molecules. Mechanism of acetylene formation from reaction with acetone and acetaldehyde, *J. Am. Chem. Soc.* 92 (1970) 5620. doi:10.1021/ja00722a014.

## References

- [113] T. Terasawa, K. Saiki, Growth of graphene on Cu by plasma enhanced chemical vapor deposition, *Carbon*. 50 (2012) 869. doi:10.1016/j.carbon.2011.09.047.
- [114] T. Shiomi, H. Nagai, K. Kato, M. Hiramatsu, M. Nawata, Detection of C<sub>2</sub> radicals in low-pressure inductively coupled plasma source for diamond chemical vapor deposition, *Diam. Relat. Mater.* 10 (2001) 388. doi:10.1016/S0925-9635(00)00420-9.
- [115] M. Hiramatsu, K. Kato, C.H. Lau, J.S. Foord, M. Hori, Measurement of C<sub>2</sub> radical density in microwave methane/hydrogen plasma used for nanocrystalline diamond film formation, *Diam. Relat. Mater.* 12 (2003) 365. doi:10.1016/S0925-9635(02)00216-9.
- [116] C. Godet, N.M.J. Conway, J.E. Bourée, K. Bouamra, A. Grosman, C. Ortega, Structural and electronic properties of electron cyclotron resonance plasma deposited hydrogenated amorphous carbon and carbon nitride films, *J. Appl. Phys.* 91 (2002) 4154. doi:10.1063/1.1454226.
- [117] A. Oda, H. Kousaka, Numerical Analysis of Substrate-Incident Carbon Flux in Low-Pressure Radio-Frequency CH<sub>4</sub> Plasmas for Deposition of Diamond-Like Carbon Films, *Electron. Commun. Japan*. 98 (2015) 31. doi:10.1002/ecj.11727.
- [118] M.J. Colgan, M. Meyyappan, D.E. Murnick, Very high-frequency capacitively coupled argon discharges, *Plasma Sources Sci. Technol.* 3 (1994) 181. doi:10.1088/0963-0252/3/2/009.
- [119] F. Mangolini, J.B. McClimon, F. Rose, R.W. Carpick, Accounting for nanometer-thick adventitious carbon contamination in X-ray absorption spectra of carbon-based materials, *Anal. Chem.* 86 (2014) 12258. doi:10.1021/ac503409c.
- [120] G.D. Cody, H. Ade, S. Wirick, G.D. Mitchell, A. Davis, Determination of chemical-structural changes in vitrinite accompanying luminescence alteration using C-NEXAFS analysis, *Org. Geochem.* 28 (1998) 441. doi:10.1016/S0146-6380(98)00010-2.
- [121] J.T. Francis, A.P. Hitchcock, Inner-shell spectroscopy of p-benzoquinone, hydroquinone, and phenol: distinguishing quinoid and benzenoid structures, *J. Phys. Chem.* 96 (1992) 6598. doi:10.1021/j100195a018.

## References

- [122] D.A. Outka, J. Stöhr, Curve fitting analysis of near - edge core excitation spectra of free, adsorbed, and polymeric molecules, *J. Chem. Phys.* 88 (1988) 3539. doi:10.1063/1.453902.
- [123] J. Robertson, The deposition mechanism of diamond-like a-C and a-C: H, *Diam. Relat. Mater.* 3 (1994) 361. doi:10.1016/0925-9635(94)90186-4.
- [124] M. Schlüter, C. Hopf, W. Jacob, Chemical sputtering of carbon by combined exposure to nitrogen ions and atomic hydrogen, *New J. Phys.* 10 (2008) 053037. doi:10.1088/1367-2630/10/5/053037.
- [125] G.S. Oehrlein, Y. Zhang, D. Vender, M. Haverlag, Fluorocarbon high - density plasmas. I. Fluorocarbon film deposition and etching using  $CF_4$  and  $CHF_3$ , *J. Vac. Sci. Technol. A Vacuum, Surfaces, Film.* 12 (1994) 323. doi:10.1116/1.578876.
- [126] S.-E. Zhu, S. Yuan, G.C.A.M. Janssen, Optical transmittance of multilayer graphene, *Europhys. Lett.* 108 (2014) 17007. doi:10.1209/0295-5075/108/17007.
- [127] K. Chen, M.N. Yogeesh, Y. Huang, S. Zhang, F. He, X. Meng, S. Fang, N. Sheehan, T.H. Tao, S.R. Bank, J.-F. Lin, D. Akinwande, P. Sutter, T. Lai, Y. Wang, Non-destructive measurement of photoexcited carrier transport in graphene with ultrafast grating imaging technique, *Carbon.* 107 (2016) 233. doi:10.1016/J.CARBON.2016.05.075.
- [128] C.M. Seah, B. Vigolo, S.P. Chai, A.R. Mohamed, Mechanisms of graphene fabrication through plasma-induced layer-by-layer thinning, *Carbon.* 105 (2016) 496. doi:10.1016/j.carbon.2016.04.072.
- [129] H. Al-Mumen, F. Rao, W. Li, L. Dong, Singular Sheet Etching of Graphene with Oxygen Plasma, *Nano-Micro Lett.* 6 (2014) 116. doi:10.5101/nml.v6i2.p116-124.
- [130] K.S. Kim, Y.J. Ji, Y. Nam, K.H. Kim, E. Singh, J.Y. Lee, G.Y. Yeom, Atomic layer etching of graphene through controlled ion beam for graphene-based electronics, *Sci. Rep.* 7 (2017) 2462. doi:10.1038/s41598-017-02430-8.
- [131] W.S. Lim, Y.Y. Kim, H. Kim, S. Jang, N. Kwon, B.J. Park, J.H. Ahn, I. Chung, B.H. Hong, G.Y. Yeom, Atomic layer etching of graphene for full graphene device fabrication, *Carbon.* 50 (2012) 429. doi:10.1016/J.CARBON.2011.08.058.

## References

- [132] Y.Y. Kim, W.S. Lim, J.B. Park, G.Y. Yeom, Layer by Layer Etching of the Highly Oriented Pyrolythic Graphite by Using Atomic Layer Etching, *J. Electrochem. Soc.* 158 (2011) D710. doi:10.1149/2.061112jes.
- [133] L. Zhang, S. Feng, S. Xiao, G. Shen, X. Zhang, H. Nan, X. Gu, K. (Ken) Ostrikov, Layer-controllable graphene by plasma thinning and post-annealing, *Appl. Surf. Sci.* 441 (2018) 639. doi:10.1016/j.apsusc.2018.02.100.
- [134] L. Persichetti, F. Tombolini, S. Casciardi, M. Diociaiuti, M. Fanfoni, G. Palleschi, A. Sgarlata, F. Valentini, A. Balzarotti, Folding and stacking defects of graphene flakes probed by electron nanobeam, *Appl. Phys. Lett.* 99 (2011) 041904. doi:10.1063/1.3615802.
- [135] V.B. Jovanović, I. Radović, D. Borcka, Z.L. Mišković, High-energy plasmon spectroscopy of freestanding multilayer graphene, *Phys. Rev. B.* 84 (2011) 155416. doi:10.1103/PhysRevB.84.155416.
- [136] M.H. Gass, U. Bangert, A.L. Bleloch, P. Wang, R.R. Nair, A.K. Geim, Free-standing graphene at atomic resolution, *Nat. Nanotechnol.* 3 (2008) 676. doi:10.1038/nnano.2008.280.
- [137] L. Sun, K.W. Noh, J.-G. Wen, S.J. Dillon, In Situ Transmission Electron Microscopy Observation of Silver Oxidation in Ionized/Atomic Gas, *Langmuir.* 27 (2011) 14201. doi:10.1021/la202949c.
- [138] N. de Jonge, F.M. Ross, Electron microscopy of specimens in liquid, *Nat. Nanotechnol.* 6 (2011) 695. doi:10.1038/nnano.2011.161.
- [139] J.Y. Huang, L. Qi, J. Li, In situ imaging of layer-by-layer sublimation of suspended graphene, *Nano Res.* 3 (2010) 43. doi:10.1007/s12274-010-1006-4.
- [140] K. Tai, T.J. Houlahan, J.G. Eden, S.J. Dillon, Integration of microplasma with transmission electron microscopy: Real-time observation of gold sputtering and island formation, *Sci. Rep.* 3 (2013) 1325. doi:10.1038/srep01325.
- [141] N. Tanaka, J. Usukura, M. Kusunoki, Y. Saito, K. Sasaki, T. Tanji, S. Muto, S. Arai, Development of an environmental high-voltage electron microscope for reaction science, *Microscopy.* 62 (2013) 205. doi:10.1093/jmicro/dfs095.

## References

- [142] K. Kamatani, K. Higuchi, Y. Yamamoto, S. Arai, N. Tanaka, M. Ogura, Direct observation of catalytic oxidation of particulate matter using in situ TEM, *Sci. Rep.* **5** (2015) 10161. doi:10.1038/srep10161.
- [143] Y. Takahashi, H. Kondo, R. Asano, S. Arai, K. Higuchi, Y. Yamamoto, S. Muto, N. Tanaka, Direct evaluation of grain boundary hydrogen embrittlement: A micro-mechanical approach, *Mater. Sci. Eng. A.* **661** (2016) 211. doi:10.1016/J.MSEA.2016.03.035.
- [144] T. Malis, S.C. Cheng, R.F. Egerton, EELS log-ratio technique for specimen-thickness measurement in the TEM, *J. Electron Microsc. Tech.* **8** (1988) 193. doi:10.1002/jemt.1060080206.
- [145] M. Filippi, L. Calliari, Measuring the energy of the graphite  $\pi + \sigma$  plasmon peak, *Surf. Interface Anal.* **38** (2006) 595. doi:10.1002/sia.2221.
- [146] T. Eberlein, U. Bangert, R.R. Nair, R. Jones, M. Gass, A.L. Bleloch, K.S. Novoselov, A. Geim, P.R. Briddon, Plasmon spectroscopy of free-standing graphene films, *Phys. Rev. B.* **77** (2008) 233406. doi:10.1103/PhysRevB.77.233406.
- [147] P.Y. Huang, J.C. Meyer, D.A. Muller, From atoms to grains: Transmission electron microscopy of graphene, *MRS Bull.* **37** (2012) 1214. doi:10.1557/mrs.2012.183.
- [148] S. Horiuchi, T. Gotou, M. Fujiwara, R. Sotoaka, M. Hirata, K. Kimoto, T. Asaka, T. Yokosawa, Y. Matsui, K. Watanabe, M. Sekita, Carbon Nanofilm with a New Structure and Property, *Jpn. J. Appl. Phys.* **42** (2003) L1073. doi:10.1143/JJAP.42.L1073.
- [149] N. Chen, R.T. Yang, Ab Initio Molecular Orbital Study of the Unified Mechanism and Pathways for Gas–Carbon Reactions, *J. Phys. Chem. A.* **102** (1998) 6348. doi:10.1021/jp981518g.
- [150] J.F. Orrego, F. Zapata, T.N. Truong, F. Mondragón, Heterogeneous CO<sub>2</sub> Evolution from Oxidation of Aromatic Carbon-Based Materials, *J. Phys. Chem. A.* **113** (2009) 8415. doi:10.1021/jp903362g.
- [151] K. Koizumi, M. Boero, Y. Shigeta, A. Oshiyama, Atom-Scale Reaction Pathways and Free-Energy Landscapes in Oxygen Plasma Etching of Graphene, *J. Phys. Chem. Lett.* **4** (2013) 1592. doi:10.1021/jz400666h.

## References

- [152] T. Sun, S. Fabris, S. Baroni, Surface Precursors and Reaction Mechanisms for the Thermal Reduction of Graphene Basal Surfaces Oxidized by Atomic Oxygen, *J. Phys. Chem. C*. 115 (2011) 4730. doi:10.1021/jp111372k.
- [153] J.L. Li, K.N. Kudin, M.J. McAllister, R.K. Prud'homme, I.A. Aksay, R. Car, Oxygen-Driven Unzipping of Graphitic Materials, *Phys. Rev. Lett.* 96 (2006) 176101. doi:10.1103/PhysRevLett.96.176101.
- [154] A. Incze, A. Pasturel, C. Chatillon, Oxidation of graphite by atomic oxygen: a first-principles approach, *Surf. Sci.* 537 (2003) 55. doi:10.1016/S0039-6028(03)00355-8.
- [155] V. Morón, P. Gamallo, R. Sayós, DFT and kinetics study of O/O<sub>2</sub> mixtures reacting over a graphite (0001) basal surface, *Theor. Chem. Acc.* 128 (2011) 683. doi:10.1007/s00214-010-0798-3.
- [156] J. Jung, H. Lim, J. Oh, Y. Kim, Functionalization of Graphene Grown on Metal Substrate with Atomic Oxygen: Enolate vs Epoxide, *J. Am. Chem. Soc.* 136 (2014) 8528. doi:10.1021/ja503664k.
- [157] A. Incze, A. Pasturel, C. Chatillon, First-principles study of the atomic oxygen adsorption on the (0 0 0 1) graphite surface and dissolution, *Appl. Surf. Sci.* 177 (2001) 226. doi:10.1016/S0169-4332(01)00216-1.
- [158] D. Lamoen, B.N.J. Persson, Adsorption of potassium and oxygen on graphite: A theoretical study, *J. Chem. Phys.* 108 (1998) 3332. doi:10.1063/1.475732.
- [159] T. Sun, S. Fabris, Mechanisms for Oxidative Unzipping and Cutting of Graphene, *Nano Lett.* 12 (2012) 17. doi:10.1021/nl202656c.

## List of figures and tables

### Figures

Figure 1.1 The schematic of the a-C structure. Black balls are C atoms, and blue balls are H atoms. ....	2
Figure 1.2 The ternary diagram of a-C films.....	4
Figure 1.3 Aksenov Quarter-torus duct macroparticle filter using plasma optical principles for cathodic arc deposition. ....	7
Figure 1.4 The schematic diagram of the subplantation model.....	8
Figure 1.5 The schematic plot of the density and the $sp^3$ fraction of a-C films as a function of ion energy per C atom.....	8
Figure 1.6 Schematic diagram of an RF sputtering system. ....	10
Figure 1.7 Fundamentals in a plasma processing. ....	13
Figure 1.8 Schematic diagram of the capacitively coupled plasma with a showerhead electrode and substrate bias power. ....	15
Figure 1.9 Electron energy distribution function (EEDF) and electron dissociation coefficient of $CH_4$ to $CH_3$ ( $\sigma_{CH_3}$ ) as functions of electron energy. ....	16
Figure 1.10 Schematic diagram of inductively coupled plasma with substrate bias power.....	18
Figure 1.11 Schematic diagram of surface wave plasma with substrate bias power. ....	19
Figure 1.12 Schematic diagram of a-C deposition scheme by PECVD [39]. ....	21
Figure 2.1 The schematic diagram of an RI-PECVD system. ....	27
Figure 2.2 The waveform of the RF bias voltage of RI-PECVD system. ....	28
Figure 2.3 The reflectance spectra of the microwave as a function of frequency. Orange dash lines are Lorentzian fit results. ....	29

## List of figures and tables

Figure 2.4	The RI-PECVD system equipped QMS.....	33
Figure 2.5	Typical Raman spectrum of a-C films deposited by RI-PECVD. The background can be described as a linear function.....	37
Figure 2.6	The plot of the variation of G position versus $FWHM_G$ . ( $\Delta$ Rose et al., + Merlen et al., see details in Ref [81] and [79]).....	37
Figure 2.7	The reference synchrotron radiation intensity measured by a Si Photodiode. ....	39
Figure 2.8	The schematic diagram of the X-ray absorption spectroscopy in a total electron yield mode. ....	39
Figure 2.9	The NEXAFS spectra of HOPG with X-ray incident angles of $30^\circ$ , $55^\circ$ , and $90^\circ$ .....	40
Figure 2.10	The schematic diagram of the Tauc plot.....	42
Figure 2.11	Comb electrode structure (top) and sample structure (bottom).....	43
Figure 2.12	Typical ESR spectrum of a-C film.....	44
Figure 2.13	Schematic plot of load versus depth from nanoindentation test using Berkovich tip. ....	45
Figure 3.1	Process procedure of each condition. (A) continuous deposition, (B) deposition with 30 s interval, (C) deposition with 30 s H atom irradiation, and (D) deposition with 30 s H atom/ion irradiation. ....	47
Figure 3.2	The schematic diagram of continuous deposition (A). ....	48
Figure 3.3	The schematic diagram of deposition with 30 s interval (B).....	49
Figure 3.4	The schematic diagram of deposition with H atom irradiation for 30 s (C). ....	50
Figure 3.5	The schematic diagram of deposition with H atom/ion irradiation for 30 s (D).....	51
Figure 3.6	Thickness of as-deposited a-C films.....	53
Figure 3.7	Raman spectra of as-deposited a-C films.....	54

## List of figures and tables

Figure 3.8 Normalized Raman spectra of as-deposited a-C films.....	55
Figure 3.9 $I_D/I_G$ of as-deposited films. ....	57
Figure 3.10 G position versus $FWHM_G$ . (● Continuous, ◆ Interval, ■ H atom, and ▲ H atom/ion).....	57
Figure 3.11 Slope/ $I_G$ of as-deposited a-C films. ....	58
Figure 3.12 Dangling bonds density of as-deposited a-C films. ....	58
Figure 3.13 Optical bandgap (Tauc gap) of as-deposited a-C films. ....	59
Figure 4.1 (a) Mass spectra of the plasma at a residence time of 2 ms with ionization energy of 15 eV (lower black line: plasma off, upper red line: plasma on). (b) Quadrupole mass spectrometer output of 15 amu at a residence time of 2 ms as a function of electron energy for ionization (black line: plasma off, red line: plasma on). ....	66
Figure 4.2 Residence time dependence of $CH_3$ density (circles). Changes in $sp^2$ fraction (diamonds) are also plotted. ....	69
Figure 4.3 $CH_4$ density (circles and triangles) and its degree of dissociation (diamonds) as functions of residence time. ....	70
Figure 4.4 Dependence of $C_2H_4$ density (circles) on residence time. $C_2/Ar$ ratios (diamonds) normalized by that at a residence time of 18 ms are also plotted. ....	71
Figure 4.5 Reactions in $H_2/CH_4$ plasma with various residence times.....	73
Figure 4.6 Hardness as a function of $CH_3$ density. ....	74
Figure 5.1 The electron density in the DF-CCP region as a function of VHF power. The dashed line is not a fit but a guide for the eye. ....	79
Figure 5.2 (a) Optical emission spectra of the $CH_4/H_2$ DF-CCP for 20 to 250 W in VHF power, (b) the Ar intensity at 811 nm as a function of electron density (the dashed line is a linear fit result), (c) normalized $[C_2]/[Ar]$	

## List of figures and tables

(square: ■), [CH]/[Ar] (circle: ●), and $[H_\alpha]/[Ar]$ (diamond: ◆) intensity ratios as functions of VHF power. ....	82
Figure 5.3 (a) Mass spectra of the DF-CCP at 250 W VHF power and (b) densities of neutral species in the DF-CCP as functions of electron densities. Dashed lines in Fig. 5(b) are simply guides for the eye. ....	84
Figure 5.4 Raman spectra of a-C grown with various electron densities. The 2-peaks Gaussian fit results are also shown in each of the plots. ....	86
Figure 5.5 The Gaussian fit of 532nm Raman spectra of as-deposited a-C films. The plot of the variation of G position versus $FWHM_G$ is shown with our RI-PECVD a-C films and various kinds of a-C films reported by Rose et al. and Merlen et al. for comparison [79,81]. ( $\Delta$ Rose et al., + Merlen et al., see details in Ref [81] and [79]) ....	87
Figure 6.1 The composition ratio of ion species in $CH_4/H_2$ DF-CCP. ....	94
Figure 6.2 The results of plasma diagnostics. Diamonds (◆) correspond to 20 W VHF power and squares (□) correspond to 250 W VHF power. (a) The electron density as a function of RF bias power; (b) H excitation temperature as a function of RF bias power; (c) The magnitude of negative self-bias voltage $ -V_{DC} $ as a function of RF bias power; (d) The ion flux as a function of the magnitude of negative self-bias voltage $ -V_{DC} $ . ....	95
Figure 6.3 Ion bombardment energy fluxes $\Gamma_{E_i}$ as a function of RF bias powers. Diamonds (◆) and squares (□) correspond to 20 and 250 W in VHF power, respectively. ....	96
Figure 6.4 Deposition rate as a function of (a) magnitudes of negative self-bias voltages ( $ -V_{DC} $ ) and (b) ion bombardment energy fluxes. Diamonds (◆) and squares (□) correspond to 20 and 250 W in VHF power, respectively. ....	97

## List of figures and tables

- Figure 6.5 The Raman spectra of as-deposited a-C films. Top 3 spectra are a-C films deposited at 20 W in VHF power (black, orange, and red lines) and bottom 3 spectra are a-C films deposited at 250 W in VHF power (green, blue, and purple lines). The ion bombardment energy flux  $\Gamma E_i$  are shown at the right and its value increase from top to bottom..... 99
- Figure 6.6 The Slope/ $I_G$  as functions of (a) the magnitude of the negative self-bias voltage  $|-V_{DC}|$  and (b) the ion bombardment energy flux  $\Gamma E_i$ . Diamonds ( $\diamond$ ) correspond to 20 W in VHF power, squares ( $\square$ ) correspond to 250 W in VHF power, and circles ( $\circ$ ) correspond to 50, 100, and 200 W in VHF power with 50 W in RF bias power. .... 100
- Figure 6.7 The dangling bonds density as a function of the ion bombardment flux. Diamonds ( $\diamond$ ) correspond to 20 W in VHF power, squares ( $\square$ ) correspond to 250 W in VHF power, and circles ( $\circ$ ) correspond to 50-200 W in VHF power with 50 W in RF bias power..... 101
- Figure 6.8 (a) The magnitude of the negative self-bias voltage  $|-V_{DC}|$  and (b) the ion bombardment energy flux  $\Gamma E_i$  dependences of G band position (G position), FWHM of G band ( $FWHM_G$ ), and intensity ratio of D band to G band ( $I_D/I_G$ ). Diamonds ( $\diamond$ ) correspond to 20 W in VHF power, squares ( $\square$ ) correspond to 250 W in VHF power, and circles ( $\circ$ ) correspond to 50, 100, and 200 W in VHF power with 50 W in RF bias power. .... 103
- Figure 6.9 Dependence of  $[C_2]/[Ar]$ , G position, and  $FWHM_G$  on the  $\Gamma E_i$ . Circles ( $\bullet$ ) corresponding to  $[C_2]/[Ar]$ , diamonds ( $\blacklozenge$ ) corresponding to G position, square ( $\blacksquare$ ) corresponding to  $FWHM_G$ . .... 105
- Figure 6.10 Carbon K-edge NEXAFS spectra of a-C spectra of as-grown a-C films and HOPG. Vertically dash lines are boundaries of the integration energy window. Top 3 spectra are for the samples prepared with 250 W in VHF power and middle 3 spectra are for the samples prepared with

## List of figures and tables

20 W in VHF power with different $ -V_{DC} $ . A spectrum of HOPG is the bottom. ....	107
Figure 6.11 The optical bandgap as a function of $\Gamma_{E_i}$ . Diamonds ( $\diamond$ ) correspond to 20 W in VHF power, squares ( $\square$ ) correspond to 250 W in VHF power, and circles ( $\circ$ ) correspond to 50-200 W in VHF power with 50 W in RF bias power. ....	109
Figure 6.12 The electrical conductivity as a function of $\Gamma_{E_i}$ . Diamonds ( $\diamond$ ) correspond to 20 W in VHF power and squares ( $\square$ ) correspond to 250 W in VHF power. .	110
Figure 6.13 The mechanism of the $C_2$ emission from the plasma and the control concept of $sp^2$ -C clusters incorporation in the a-C films. ....	112
Figure 6.14 Dependence of $[C_2]/[Ar]$ on the deposition temperature. ....	113
Figure 6.15 The plot of the G position versus $FWHM_G$ for the data set of deposition temperature dependence. ....	113
Figure 7.1 (a) Schematic of experimental setup with reaction-science TEM chamber and the environmental cell (gas chamber), equipped with the newly developed, remote-type plasma source. Plasma discharges were applied to the TEM samples, 5 cm apart. (b) The typical optical emission spectrum of remote oxygen plasma with a microwave power of 20 W, an $O_2$ flow rate of 1 sccm, and a pressure at 4.6 Pa. ....	121
Figure 7.2 TEM images of etching from the graphene. The total remote oxygen plasma irradiation times are shown at the bottom-left corner of each figure. The dash line circle indicates the measurement area of EELS and electron diffraction. ....	122
Figure 7.3 (a) Plasmon peaks of EEL spectra in the low-loss region. (b) Relative thickness ( $t/\lambda$ ) as a function of the intensity ratio of the $\pi$ plasmon and $\pi + \sigma$ plasmon at 25 eV ( $[\pi + \sigma]/[\pi]$ ). (c) The relationship between the number of layers and $[\pi + \sigma]/[\pi]$ (from the data obtained by Jovanović[135]). The red dots indicate the $[\pi + \sigma]/[\pi]$ measured in this	

## List of figures and tables

experiment for the remote oxygen plasma irradiation. (d) A number of etched layers as a function of the irradiation time. ....	124
Figure 7.4 TEM images of etching from point defect at the graphene basal plane. The total remote oxygen plasma irradiation times are shown at the bottom left of each figure. ....	127
Figure 7.5 Enlarged TEM images of etching from the tip of edge. ....	127
Figure 7.6 Amount of etching of graphene from edge (○), point defect (□), and the tip of edge (△). The data for the edge is the average of the three lines. The gray dashed line corresponds to the result of linear fitting with a determination coefficient ( $R^2$ ). ....	128
Figure 7.7 Electron diffraction pattern of graphene before and after 1-60 min remote plasma irradiation. The total remote oxygen plasma irradiation times are shown at the top left of each graph. ....	129
Figure 8.1 The proposed film formation mechanism by PECVD. ....	136

## Tables

Table 1.1 Comparison of the electron density ( $n_e$ ) and the electron temperature ( $T_e$ ) among CCP, ICP, and SWP [38]. ....	19
Table 3.1 The process conditions of the sequential deposition. ....	52
Table 4.1 The deposition conditions. ....	64
Table 5.1 The deposition conditions. ....	77
Table 6.1 The deposition conditions. ....	92

## List of papers and presentations related to this thesis

### Original Papers

	Title (Related chapter)	Journal	Authors
1	Effects of gas residence time of CH <sub>4</sub> /H <sub>2</sub> on sp <sup>2</sup> fraction of amorphous carbon films and dissociated methyl density during radical-injection plasma-enhanced chemical vapor deposition (Chapter 4)	Japanese Journal of Applied Physics 57, 06JE03 (2018) [Published]	Hirotsugu Sugiura Lingyun Jia Hiroki Kondo Kenji Ishikawa Takayoshi Tsutsumi Toshio Hayashi Keigo Takeda Makoto Sekine Masaru Hori
2	Control of sp <sup>2</sup> -C cluster incorporation of amorphous carbon films grown by H-radical-injection CH <sub>4</sub> /H <sub>2</sub> plasma enhanced chemical vapor deposition (Chapter 5)	Japanese Journal of Applied Physics [Accepted]	Hirotsugu Sugiura Lingyun Jia Yasuyuki Ohashi Hiroki Kondo Kenji Ishikawa Takayoshi Tsutsumi Toshio Hayashi Keigo Takeda Makoto Sekine Masaru Hori
3	Effects of ion bombardment energy flux on chemical compositions and structures of hydrogenated amorphous carbon films grown by a radical-injection plasma-enhanced chemical vapor deposition (Chapter 6)	C   Journal of Carbon Research [Accepted]	Hirotsugu Sugiura Hiroki Kondo Takayoshi Tsutsumi Kenji Ishikawa Masaru Hori

List of papers and presentations related to this thesis

4	<i>In situ</i> observation of layer-by-layer thinning of graphene with remote oxygen plasma using reaction-science high-voltage transmission electron microscopy (Chapter 7)	[To be submitted]	Hirotsugu Sugiura Hiroki Kondo Kimitaka Higuchi Shigeo Arai Ryo Hamaji Takayoshi Tsutsumi Kenji Ishikawa Masaru Hori
---	--	-------------------	---

**Presentations in International conferences**

	Title (Related chapter)	Conference	Authors
1	Effects of ion bombardments on electronic properties of amorphous carbon films grown by plasma-enhanced chemical vapor deposition	9th international Conference on Reactive Plasmas / 68th Gaseous Electronics Conference / 33rd Symposium on Plasma Processing Hawaii Convention Center, Honolulu, USA Oct. 12-16, IW2.00002 (2015)	Hirotsugu Sugiura Lingyun Jia Hiroki Kondo Kenji Ishikawa Keigo Takeda Makoto Sekine Masaru Hori
2	Effects of ion irradiation on electronic properties of amorphous carbon films grown by plasma-enhanced chemical vapor deposition	The 37th International Symposium on Dry Process Awaji Yumebutai International Conference Center, Awaji Island, Japan Nov. 5-6, P-38 (2015)	Hirotsugu Sugiura Lingyun Jia Hiroki Kondo Keigo Takeda Kenji Ishikawa Makoto Sekine Masaru Hori
3	Effects of radicals and ions on electronic properties of amorphous carbon films grown by plasma-enhanced chemical vapor deposition	8th International Symposium on Advanced Plasma Science and its Applications for Nitrides and Nanomaterials / 9th International Conference on Plasma-Nano Technology & Science, Nagoya University, Nagoya, Japan Mar. 6-10, 07pB06O (2019)	Hirotsugu Sugiura Lingyun Jia Hiroki Kondo Kenji Ishikawa Keigo Takeda Makoto Sekine Masaru Hori

List of papers and presentations related to this thesis

4	Effects of residence time on growth characteristics and properties of amorphous carbon films grown by radical-injection plasma-enhanced chemical vapor deposition	2016 MRS Fall Meeting & Exhibit Hynes Convention Center, Boston, MA Nov. 27-Dec. 2, PM5.3.17 (2016)	Hirotsugu Sugiura Lingyun Jia Shunichi Sato Hiroki Kondo Keigo Takeda Kenji Ishikawa Makoto Sekine Masaru Hori
5	Effects of residence time on dissociations of precursor molecules in H <sub>2</sub> /CH <sub>4</sub> plasma	The 39th International Symposium on Dry Process Tokyo Tech Front (Kuramae Kaikan), Tokyo Institute of Technology, Tokyo, Japan Nov. 16-17, P-52 (2017)	Hirotsugu Sugiura Lingyun Jia Hiroki Kondo Kenji Ishikawa Takayoshi Tsutsumi Makoto Sekine Masaru Hori
6	Control of sp <sup>2</sup> -C fraction in amorphous carbon films and its hardness by formation of precursor radicals depending on a residence time	11th International Symposium on Advanced Plasma Science and its Applications for Nitrides and Nanomaterials / 12th International Conference on Plasma-Nano Technology & Science, Nagoya Institute of Technology, Nagoya, Japan Mar. 17-20 (2019) [Accepted]	Hirotsugu Sugiura Yasuyuki Ohashi, Lingyun Jia Hiroki Kondo Kenji Ishikawa Takayoshi Tsutsumi Toshio Hayashi Keigo Takeda Makoto Sekine Masaru Hori

## Acknowledgments

The present research was performed in Professor Dr. Horii and Professor Dr. Ishikawa Laboratory, Department of Electronics, Nagoya University.

The author would like to appreciate his research advisor, Professor Dr. Masaru Horii, Institute of Innovation for Future Society, Nagoya University, for his guidance, advice, and encouragements through the course of this research.

The author also would like to thank his vice-advisors, Professor Dr. Kenji Ishikawa, Plasma Nanotechnology Research Center, Nagoya University, and Associate Professor Dr. Hiroki Kondo, Plasma Nanotechnology Research Center, Nagoya University, for lots of valuable comments.

The author also would like to thank his vice-advisers, Professor Dr. Seiichi Miyazaki, Department of Electronics, Nagoya University, Professor Dr. Yutaka Yoshida, Department of Electrical Engineering, Nagoya University, and Professor Dr. Nagahiro Saito, Department of Chemical Systems Engineering, Nagoya University for their guidance and valuable suggestions in preparing this thesis.

The author is enormously grateful to Professor Dr. Makoto Sekine, Professor Dr. Toshio Hayashi, Professor Dr. Osamu Oda, Professor Dr. Hitoshi Ito, Professor Dr. Naohiro Shimizu, and Assistant Professor Dr. Takayoshi Tsutsumi, Plasma Nanotechnology Research Center, Nagoya University, Associate Professor Dr. Hiromasa Tanaka, and Assistant Professor Dr. Hiroshi Hashizume, Institute of Innovation for Future Society, Nagoya University, Professor Dr. Mineo Hiramatsu, Professor Dr. Masafumi Ito, Professor Dr. Takayuki Ohta, and Associate Professor Dr. Keigo Takeda,

## Acknowledgments

Department of Electrical and Electronic Engineering, Meijo University, for their valuable comments and suggestions.

The author also would like to thank Professor Dr. Noritsugu Umehara and Assistant Professor Dr. Motoyuki Murashima, Department of Micro-Nano Mechanical Science and Engineering, Nagoya University, for the measurement of nanoindentation.

The author also would like to appreciate help to carry out experiments and fruitful discussions from his group members, Dr. Lingyun Jia, Mr. Xu Da, Mr. Masayuki Nakamura, Mr. Shunichi Sato, Mr. Koutaro Okimura, Mr. Yasuyuki Ohashi, and Mr. Ryo Hamaji.

The authors would like to thank Dr. Masashi Nakatake of Aichi Synchrotron Radiation Center, Aichi Science & Technology Foundation, Aichi, Japan, for supporting the NEXAFS measurements.

The authors would like to thank Professor Shigeo Arai and Mr. Kimitaka Higuchi of Institute of Materials and Systems for Sustainability (IMaSS), Nagoya University, for conducting the TEM measurements.

The author would like to acknowledge Dr. Shoji Den and Dr. Koji Yamakawa at Katagiri Engineering Co., Ltd., Yoshiaki Watanabe at Innovation Science Ltd. for their helpful advice and discussions about the experimental equipment.

The author would like to acknowledge all members in Leadership Development Program for Space Exploration and Research, Nagoya University Program for Leading Graduate School, Nagoya University for giving the chance to grow up mentally.

The author would like to acknowledge Mr. Tsunetoshi Nakamura at Science Shokai Co., Ltd. for preparation of the experimental equipment.

## Acknowledgments

The author would like to acknowledge Dr. Tsuyoshi Moriya, Mr. Satoshi Tanaka, Mr. Yoshinori Morisada, and Dr. Tadashi Mitsunari at Tokyo Electron Technology Solutions Limited for their helpful advice and discussions.

The author would like to thank his colleagues including Dr. Tomoki Amano, Dr. Naoyuki Kurake, Dr. Timothy Ryan Brubaker, Dr. Shun Imai, Dr. Masakazu Tomatsu, Dr. Yusuke Fukunaga, Dr. Borude Ranjit Rohidas, Dr. Lin Louis, Mr. Takumi Ito, Mr. Kazuki Iwamoto, Mr. Takumi Kumakura, Mr. Kazuaki Kojima, Mr. Jialin Pan for giving the big pleasure in his life.

The author also thanks sincerely Dr. Yudai Miyawaki, Dr. Hironao Shimoeda, Dr. Toshiya Suzuki, Dr. Hyung Jun Cho, Dr. Lu Yi, Dr. Yusuke Kondo, Dr. Zecheng Liu, Dr. Atsushi Ando, Dr. Yan Zhang, Mr. Takashi Kako, Mr. Kuangda Sun, Mr. Jiadong Cao, Mr. Haoran Wang, Mr. Keita Miwa, Ms. Sijie Liang, Mr. Atsuki Asano, Mr. Shinnosuke Takai, Mr. Suiki Tanaka, Mr. Takuya Tonami, Mr. Kenichi Naito, Mr. Ryo Furuta, Mr. Naoki Yoshitake, Mr. Masato Imamura, Mr. Toshinari Ueyama, Mr. Daiki Kanno, Mr. Ren Kuramashi, Mr. Yukihiro Kurokawa, Ms. Mika Takahashi, Mr. Tomonori Ichikawa, Ms. Moe Okabe, Mr. Xitong Xie, Ms. Yao Han, Ms. Kaede Katsuno, Mr. Naoki Takeda, Mr. Yugo Hosoi, Mr. Kaito Murakami, Mr. Soutarou Yamaoka, Mr. Takahiro Ohmichi, Mr. Takumi Kato, Mr. Kazuya Nakane, Mr. Masaki Hasegawa, Mr. Shogo Maeda, Mr. Ni Jiawei, Ms. Liu Yang, Mr. Ozaki Atsushi, Mr. Suda Yuki, Mr. Ryusei Sakai, Mr. Masahiro Hazumi, Mr. Matsumura Shogo, Mr. Moriyama Tatsuyuki, and all other students who have studied in Professor Hori and Professor Ishikawa Laboratory for giving the big pleasure in his life and creating a most enjoyable working atmosphere.

## Acknowledgments

The author would like to thank Ms. Yoko Kuwabara, Ms. Kazuyo Hirota, Ms. Taeko Terasawa, Ms. Aya Honda, Ms. Yoko Mizuno, and Ms. Yoshiko Kubo for lots of encouragements and helpful advice in day-to-day life.

Finally, the author would like to appreciate the help, support, and encouragement from his wife, Ayano Sugiura, parents, Kazuhiro Sugiura and Naoko Sugiura, brothers, grandparents, uncles, aunts, and cousins.

杉浦 啓嗣  
Tchirotsugu Sugiura

February 2019